CALIBRATION OF CMS LUMINOMETERS USING VAN DER MEER AND EMITTANCE SCANS

by

Yusuf Can Çekmecelioğlu

B.S., Physics, Boğaziçi University, 2018

Submitted to the Institute for Graduate Studies in
Science and Engineering in partial fulfillment of
the requirements for the degree of
Master of Science

Graduate Program in Physics

Boğaziçi University

2021

ACKNOWLEDGEMENTS

I want to start by expressing my gratefulness towards my family for their support and belief in me at every turn leading to this thesis and beyond.

I would like to thank my supervisor Olena Karacheban for her endless patience and superb mentorship, which made this thesis possible and advanced my understanding of being a scientist in every way.

I would like to thank my advisors Erhan Gülmez and Bora Akgün for their amazing guidance and patience during my thesis writing. I could not complete this work without their presence and pushes that countervailed my procrastination. I would also like to thank my thesis committee members Mithat Kaya and Özlem Sevinç Kaya, for their time, comments, and suggestions.

Additionally, I would like to thank all my friends for their mental support during my studies. Especially to Suat Dönertaş for his great companionship during my time at CERN, and to Zeynep Güneş Sönmez for supporting me tirelessly during my stressful times.

Finally, I would like to give my special appreciation to Veysi Erkcan Özcan for his time and great feedback as part of my thesis committee, but more importantly, as my original mentor, he is my reason to start in High Energy Physics in the first place. I would not be at the place where I am today without him giving a chance to a random second-year student with no knowledge to prove and improve himself. For which, I will always remain grateful.

ABSTRACT

CALIBRATION OF CMS LUMINOMETERS USING VAN DER MEER AND EMITTANCE SCANS

The calibration for the CMS luminosity measurement for the 2018 LHC run is described. The principal calibration is derived from the analysis of the van der Meer scan program in CMS taken in LHC fill 6868 on June 30th–July 1st, 2018. Additionally, the performance and stability of the CMS luminometers is evaluated using emittance scans taken throughout the course of the year. The systematic uncertainty on the absolute calibration from the van der Meer scan is measured as 2.1%. The dominant systematic uncertainties in the van der Meer calibration are those arising from the x-y correlations of the beam shape and the scan to scan variations.

ÖZET

VAN DER MEER VE EMİTANS ÖLÇÜMLERİNİ KULLANARAK CMS LUMİNOSİTE DEDEKTÖRLERİNİN KALİBRASYONU

Bu tezde, Büyük Hadron Çarpıştırıcısı'nın 2018 yılı çalışması için CMS luminosite ölçümü yöntemi ve kalibrasyon verileri açıklanmıştır. Temel kalibrasyon, 30 Haziran-1 Temmuz 2018'de gerçekleşen 6868 nolu BHÇ veri grubunun, CMS'deki van der Meer tarama programıyla analizinden elde edilmiştir. Ek olarak, CMS luminosite dedektörlerinin performansı ve kararlılığı, yıl boyunca alınan emitans taramaları kullanılarak değerlendirilmiştir. 2018 yılı için van der Meer taramasından elde edilen mutlak kalibrasyon değerleri %2.1'lik sistematik belirsizlik ile elde edilmiştir. Van der Meer kalibrasyonundaki baskın sistematik belirsizlikler, ışın şeklinin x-y koordinat bağımlılıklarından ve taramadan taramaya fark gösteren kalibrasyon değerlerinin değişiminden kaynaklanmaktadır.

TABLE OF CONTENTS

LIST OF FIGURES

LIST OF TABLES

LIST OF SYMBOLS

f_{LHC}	Revolution Frequency of LHC
R(t)	Raw Number of Observed Quantity as a Function of Time
$\mathcal{L}$	Integrated Luminosity
$\mathcal{L}_{inst}$	Instantaneous Luminosity
Σ	Convoluted Beam Width
σ	Cross Section
σ_{vis}	Visible Cross Section
μ	Average Number of Measured Signals

LIST OF ACRONYMS/ABBREVIATIONS

ALICE	A Large Ion Collider Experiment
ATLAS	A Toroidal LHC ApparatuS
BB/bb	Beam-Beam Correction
BCM1F	Fast Beam Condition Monitor
BG/bg	Background Correction
BPM	Beam Position Monitors
BSRT	Beam Synchrotron Radiation Telescope
BRIL	Beam Radiation, Instrumentation, and Luminosity
BQM	Beam Quality Monitors
CMS	Compact Muon Solenoid
DAQ	Data Acquisition
DB/db	Dynamic-Beta Correction
DCCT	DC Current Transformers
DT	Drift Tubes
emit	Emittance Scan
ERGO	Environment and Radiation Graphic Observer
FBCT	Fast Beam Current Transformers
HFET	Hadronic Forward E_T
HFOC	Hadronic Forward Occupancy
Hz	Hertz
GeV	Giga Electron-Volt
imag	Imaging Scan
LDM	Longitudinal Density Monitors
LEP	Large Electron–Positron Collider
LHC	Large Hadron Collider
LHCb	LHC Beauty
LSC/lsc	Length-Scale Correction
norm	Normal Scan

MA	Mega Ampere
MHz	Mega Hertz
MeV	Mega Electron-Volt
OD/od	Orbit-Drift Correction
off	Offset Scan
PCC	Pixel Cluster Counting
PLT	Pixel Luminosity Telescope
PS	Proton Synchrotron
RAMSES	Radiation Monitoring System for the Environment and Safety
REMUS	Radiation and Environment Monitoring Unified Supervision
SBIL	Single Bunch Instantaneous Luminosity
SPS	Super Proton Synchrotron
TeV	Tera Electron-Volt
vdM	van der Meer
VTX	Vertex Counting

1. INTRODUCTION

The Large Hadron Collider (LHC) is the largest particle accelerator ever built, up to date. Operating at the center of mass energy of 13 TeV, LHC holds the title of being the highest-energy accelerator in the world. The properties of the particles produced by the hadronic collisions are directly bounded by the available center of mass energy of the collided particles. Thus, the higher the accelerator's energy, the higher the possibility of creating the particles sought at the collision points.

There are four experiments located on the collision points of LHC. The Compact Muon Solenoid (CMS) is one of the two general-purpose detectors operating at LHC. The luminosity recorded and measured by the CMS experiment establishes the reference for cross section measurements of physics processes and the sensitivity reach of searches for new physics. Moreover, the uncertainty on the luminosity measurement often constitutes the leading systematic effect on the precise measurements of Standard Model processes. Hence, the precision of the luminosity measurements directly influences the precision of the physics studies using the CMS detector.

The Beam Radiation, Instrumentation, and Luminosity (BRIL) group is responsible for monitoring and publishing the luminosity values and beam diagnostic measurements for the CMS experiment using both the dedicated luminosity detectors (luminometers) and general-purpose detectors in the CMS detector. This thesis comprises the results of measurement for the 2018 absolute calibration of luminosity for the CMS detector, performed by the BRIL group.

Chapter 2 and 3 are dedicated to 'the introduction of LHC and the CMS experiment' in detail, respectively. In Chapter 4, 'the definition and the calculation of the luminosity' are discussed. The instantaneous luminosity has the formula of,

$$\mathcal{L}_{\text{inst}} = \frac{R(t)}{\sigma_p} \tag{1.1}$$

where $R(t)$ is the raw measured rate of the observed quantity in the detector as a function of time and σ_p is the cross section of the particle production. The raw rate measurements and the detector specifics are explained in Chapter 5. Details of the 'σ_{vis}', which is the production cross section visible by the detectors that replaces the σ_p in Equation 1.1, and 'the corrections and the systematic uncertainties' applied on σ_{vis} are discussed in Chapter 6 and Chapter 7, respectively. Chapter 8 focuses on 'the analysis framework' that is used and developed further for the analysis of the absolute calibration constant σ_{vis}. Finally, the results of all analyses including 'σ_{vis} values, corrections and systematic uncertainties' are demonstrated in Chapter 9.

2. THE LARGE HADRON COLLIDER

With a circumference of 26.7 km and a center of mass energy of 13 TeV, the Large Hadron Collider (LHC) is currently the largest and most energetic particle accelerator in the world [1]. LHC is located in an average of 100 m deep underground tunnel that resides beneath the France-Swiss border near Geneva as illustrated in Figure 2.1 [2].

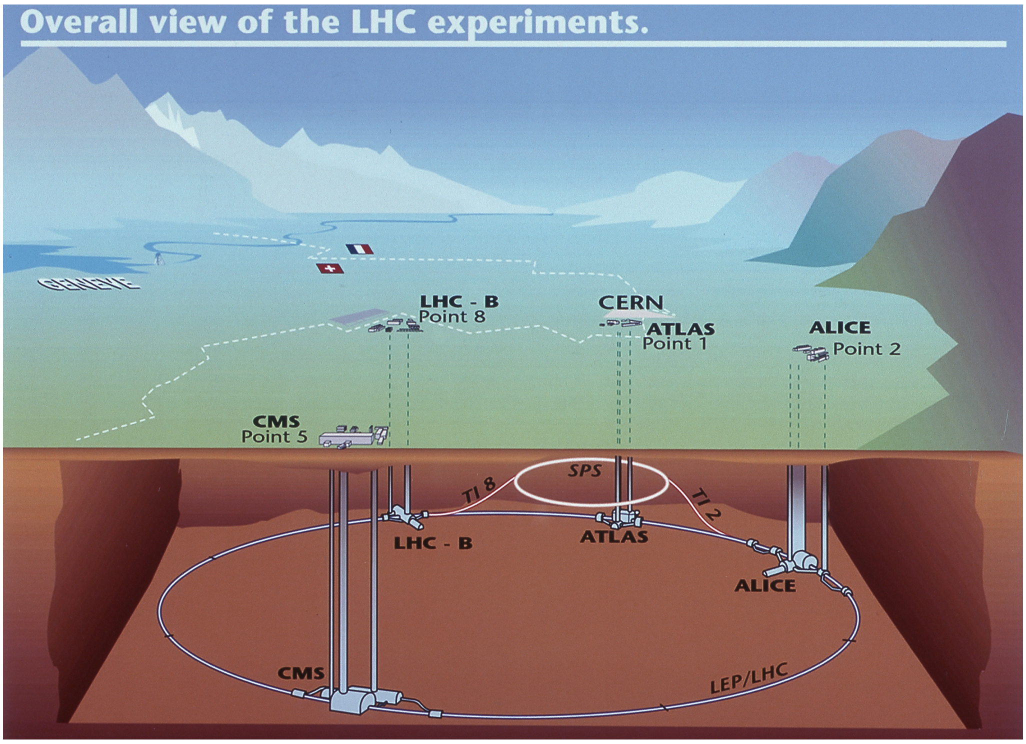

Figure 2.1: Illustration of the location for LHC and CERN.

The first plan for the LHC project was published in 1996 [3], yet its construction was completed in 2008. Subsequently, the first successful beam circulation in LHC was achieved in 2008. However, due to the technical problems that occurred in the machine, the first beam collisions could only be achieved in 2009. Since then, LHC is continuing to be one of the most important scientific advancements in human history.

2.1. Design and Technical Details of LHC

LHC uses the tunnel built in 1988 for the Large Electron-Positron Collider (LEP). The highest energy that LEP could reach was 209 GeV due to the high energy loss to synchrotron radiation.[1] In the same geometrical dimensions of LEP, LHC can reach the center of mass energy of 13 TeV since it accelerates hadrons rather than electrons and positrons. LHC consists of a two-ring superconducting hadron accelerator for two separate beams going in opposite directions. The rings do not form a perfect circular shape. Instead, they consist of arcs and straight sections (insertions). As shown in Figure 2.2, LHC is divided into eight octants where each octant corresponds to a region starting from one arc to the next. The length of each arc is 2.45 km and contains 154 dipole bending magnets to stir the beam in the beam-pipe.[2] Furthermore, the length of each insertion is 528 m. The insertions are used for various roles like beam injections and beam dumping, but the most prominent role is containing the collision points for the experiments at the LHC. The two beams collide on four interaction points (IP) on LHC. These four IPs are illustrated in Figure 2.2 [1] with stars.

Each of the IPs corresponds to one major experiment and thus, one detector to detect produced particles from hadronic collisions. The four experiments located on LHC and their respective IPs are:

(i) IP 1 - A Toroidal LHC ApparatuS (ATLAS)
(ii) IP 2 - A Large Ion Collider Experiment (ALICE)
(iii) IP 5 - Compact Muon Solenoid (CMS)
(iv) IP 8 - Large Hadron Collider beauty (LHCb)

Moreover, octants 2 and 8 include beam injection points besides the ALICE and LHCb experiments. Similarly, octant 6 consists of a beam dump point for the vertical ejections of the beam from the machine, and octants 3 and 7 hold a collimation system to clean up the loose particles traveling alongside the beams.

[1] Synchrotron radiation occurs when a charged particle is accelerated perpendicular to its velocity.
[2] The beam pipe contains the hadrons that circulate in the LHC.

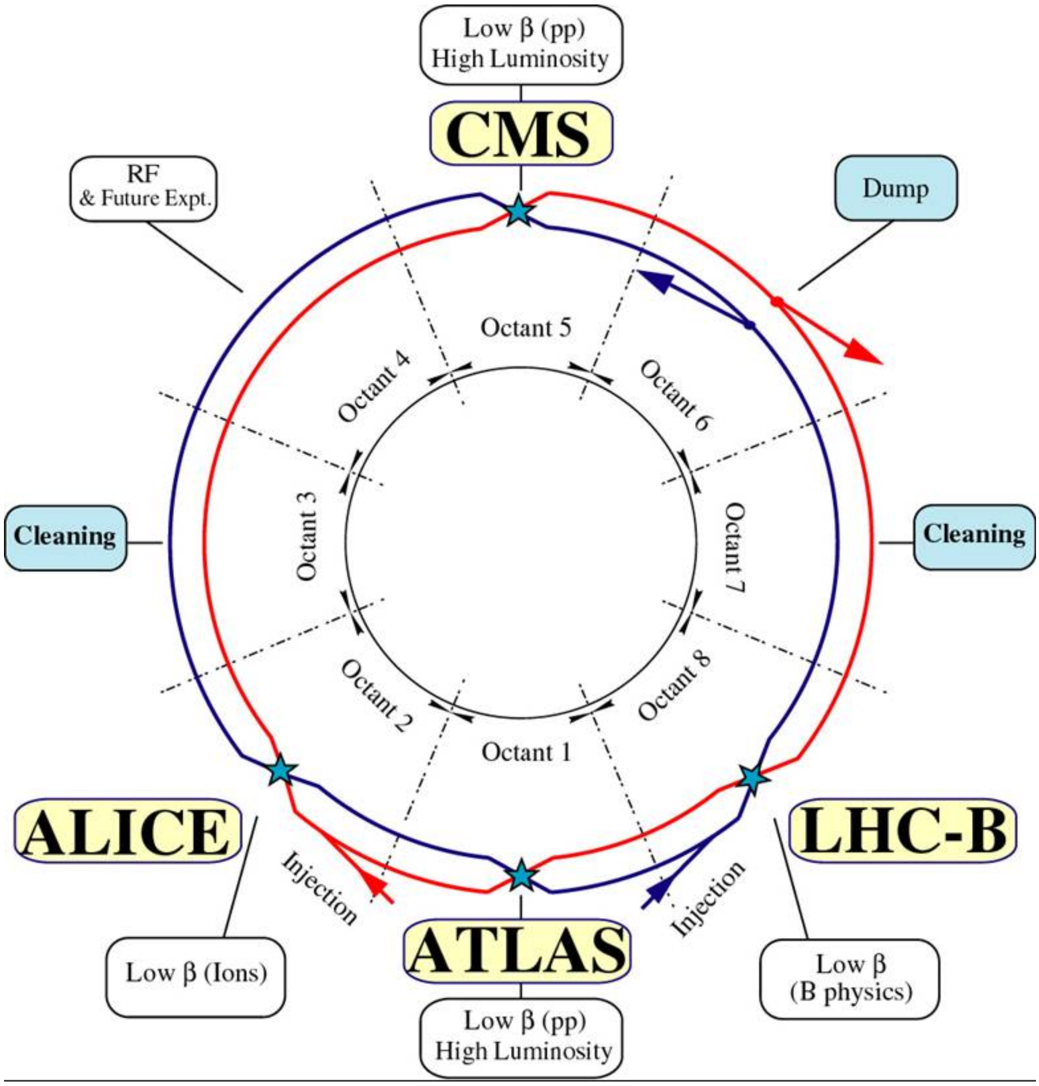

Figure 2.2: Schematic view of LHC sections. The low β indicates the high squeezing effect at the collision points.

LHC has seven detectors installed on it, including the four major experiments ATLAS, CMS, ALICE, and LHCb. The Large Hadron Collider forward (LHCf) experiment and the TOTal Elastic and diffractive cross section Measurement (TOTEM) experiment use forward detectors located near the ATLAS and CMS experiments, respectively. Additionally, the Monopole and Exotics Detector at the LHC (MoEDAL) experiment is located near the LHCb experiment. Out of the four major experiments, the ATLAS and CMS experiments have general-purpose detectors to investigate a wide range of distinct physics phenomena, whereas the LHCb and ALICE experiments focus on 'bottom-quark'[3] studies and 'quark-gluon plasma' studies, respectively.

[3]Also known as 'beauty-quark'.

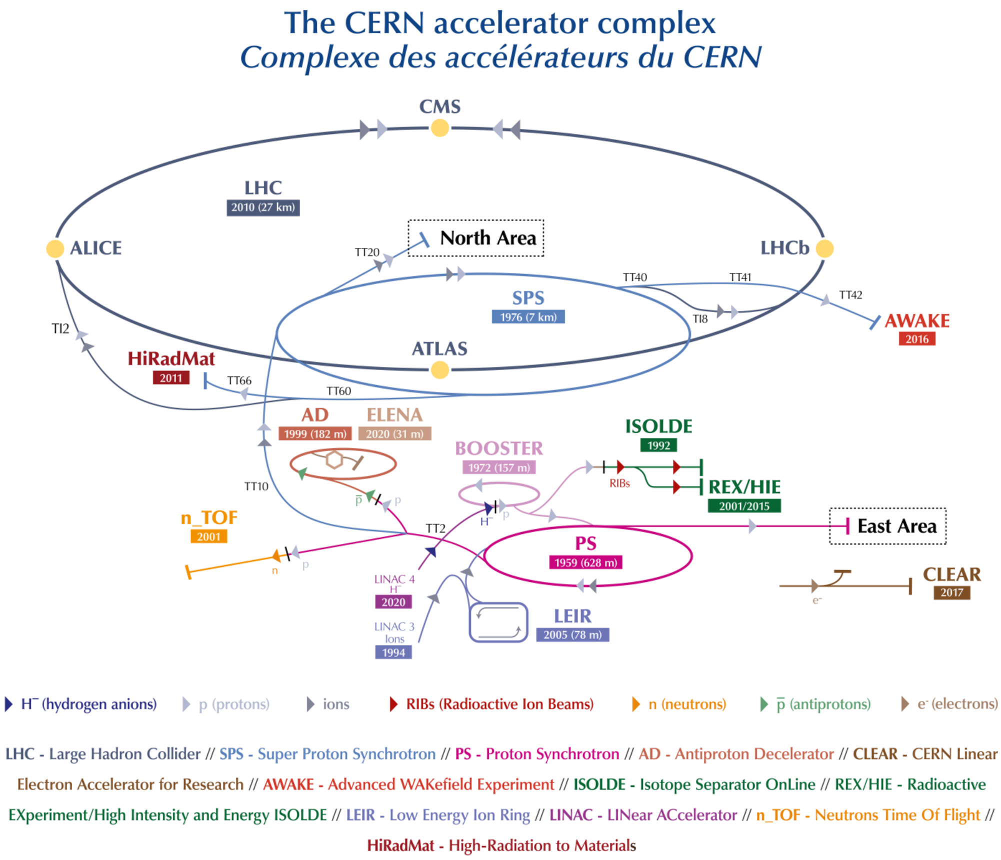

Figure 2.3: Schematics showing the accelerator complex of CERN.

LHC is designed to provide a beam energy of 7 TeV. However, in order to achieve this energy, the beams go through series of smaller particle accelerators, as illustrated in Figure 2.3 [4]. First, the hydrogen gas atoms[4] are stripped off their electrons to leave only the protons to be collected and accelerated in 'Linac 2'[5] to 50 MeV energy.Next, protons are fed into the 'Booster', the first ring accelerator in the chain that boosts the protons to 1.4 GeV energy levels. Then, the protons move to the 'Proton Synchrotron (PS)' to get accelerated to 25 GeV, and in the process, they form a bunch structure with frequency of 40 MHz.[6] Lastly, accelerated protons are injected into the 'Super Proton Synchrotron (SPS)' to get accelerated to 450 GeV before moving to LHC and getting to the energy level as high as 6.5 TeV.

[4]LHC also accelerates heavy ions like 'lead' and 'xenon' nuclei for special studies. The process of the acceleration of heavy ions follows the same procedure as protons.

[5]A linear accelerator that starts the chain of acceleration for LHC.

[6]Corresponding to 25 nano-second spacing in between successive bunches.

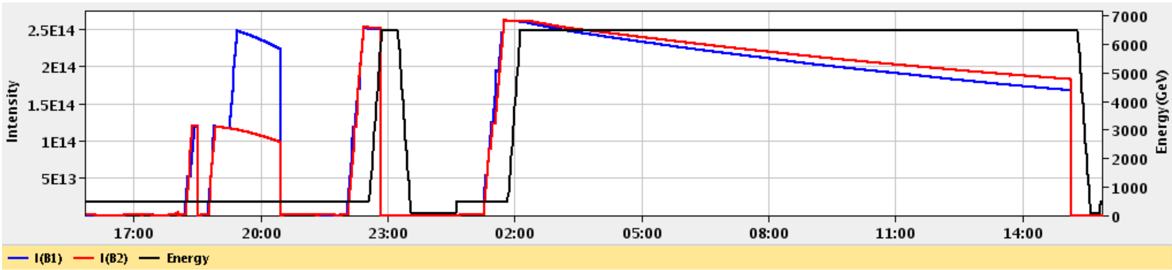

Figure 2.4: Graph of a typical fill period at LHC, indicating beam 1 with blue, beam 2 with red, and LHC machine energy as black.

The protons start with 0.999997828 times of the speed of light at the injection to LHC and they reach 0.999999990 times the speed of light at top energy. Each beam typically have 2808 bunches that contains 1.15×10^{11} protons in each that equates a total of approximately 3.2×10^{14} protons for a beam [1]. The average number of collisions produced per bunch crossing is called ‘pile-up’. Furthermore, a ‘fill’ comprises the timeline of the protons from entering the accelerator complex of Linac, PS, SPS, and LHC, respectively, until the beam dumping occurs. In terms of machine modes of LHC [5], a regular ‘physics fill’[7] follows the order of: Injection, ramp, flat top, squeeze, stable beams, dump, and ramp down.

The protons injected in the LHC with the ‘injection’ mode become online and stay in the machine until the ‘dump’ is stated. ‘Ramp’ indicates the period where the protons are accelerated from the SPS energy levels to the LHC energy levels. Similarly, ‘ramp down’ marks the beams’ ejection from the machine. The modes ‘flat top’, ‘squeeze’, and ‘adjust’ are for the checks and adjustments on the beams’ intensity for acquiring the maximum efficiency from the collisions. Finally, the ‘stable beam’ is declared to switch LHC to the collision mode. At this period, the two beams start colliding at the interaction points (1, 2, 5, and 8) every 25 ns, simultaneously signaling the experiments on LHC to begin the data acquisition. Figure 2.4 demonstrates a typical physics fill indicating the beam intensity in number of protons and energy in GeV as a function of time.

[7]Excludes special fills (e.g. low energy, short, long, van der Meer etc.).

3. THE COMPACT MUON SOLENOID

The Compact Muon Solenoid is designed as a general-purpose detector to study various physics phenomena such as the search for Standard-Model Higgs Boson, Supersymmetric particles, new massive Vector Bosons, extra dimensions, and heavy-ion physics. Although the detector itself is 21.6 m in length, 14.6 m in height, 14.6 m in width, and weights 12.5 tonnes, it is considered 'compact' compared to other general-purpose detectors (e.g., the ATLAS detector). With a 3.8 Tesla magnetic field providing a superconducting 'solenoid' magnet, CMS is designed to deliver precise measurements for 'muon' studies.

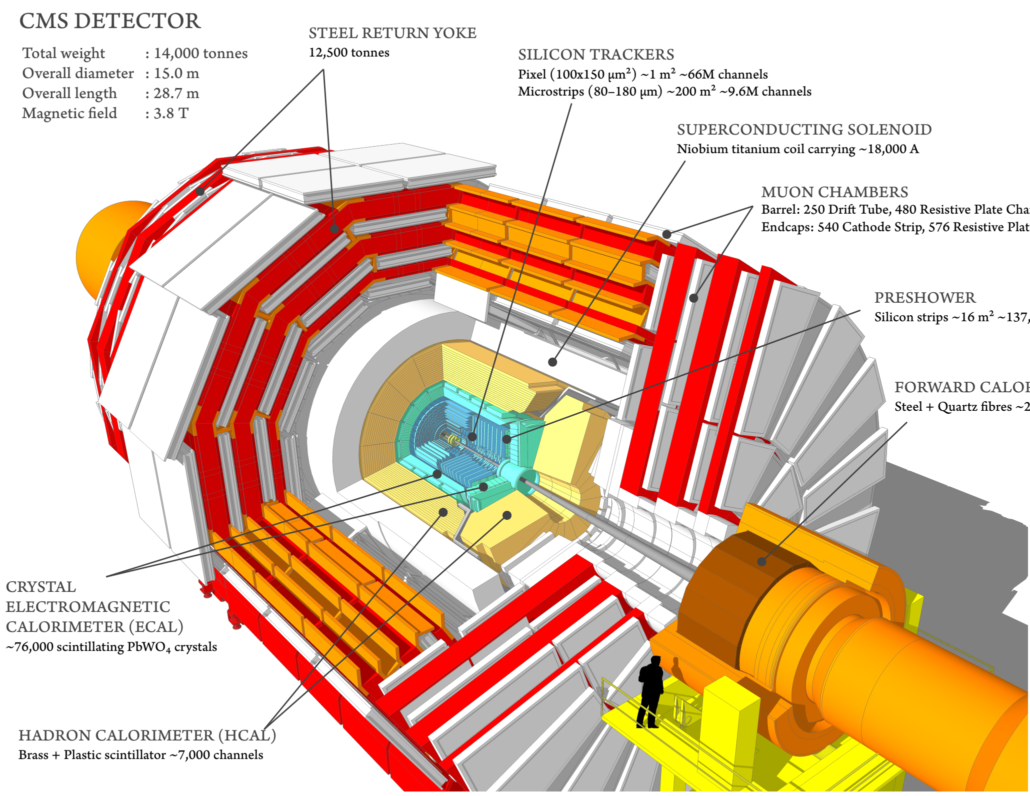

Figure 3.1: The detector of the CMS experiment with indication to the sub-sections and their layout.

Figure 3.1 shows the layered structure of the CMS detector, indicating the main parts and the locations [6]. CMS is built around its superconducting solenoid magnet, forming a cylindrical shape.

Figure 3.2 illustrates the coordinate systems of the CMS detector. CMS uses a right-handed Cartesian coordinate system with an origin centered at the collision point (IP5). The x-axis points radially inward towards the center of LHC. The y-axis points vertically upwards from the ground. Finally, the z-axis points along the direction of the beam pipe that passes through the center of the detector. Due to the cylindrical shape of the CMS detector, the azimuthal angle ϕ measured from the x-axis in the x-y plane, and the polar angle θ calculated from the z-axis are also used. Additionally, the pseudorapidity η is defined as $\eta = -ln(tan(\theta/2))$ as shown in Figure 3.2. The transverse momentum p_{T} and the transverse energy E_{T}, that measures the momentum and energy in the transverse plane (the x-y plane) to the beam direction (z-axis), are computed from the x and y coordinates, respectively [7].

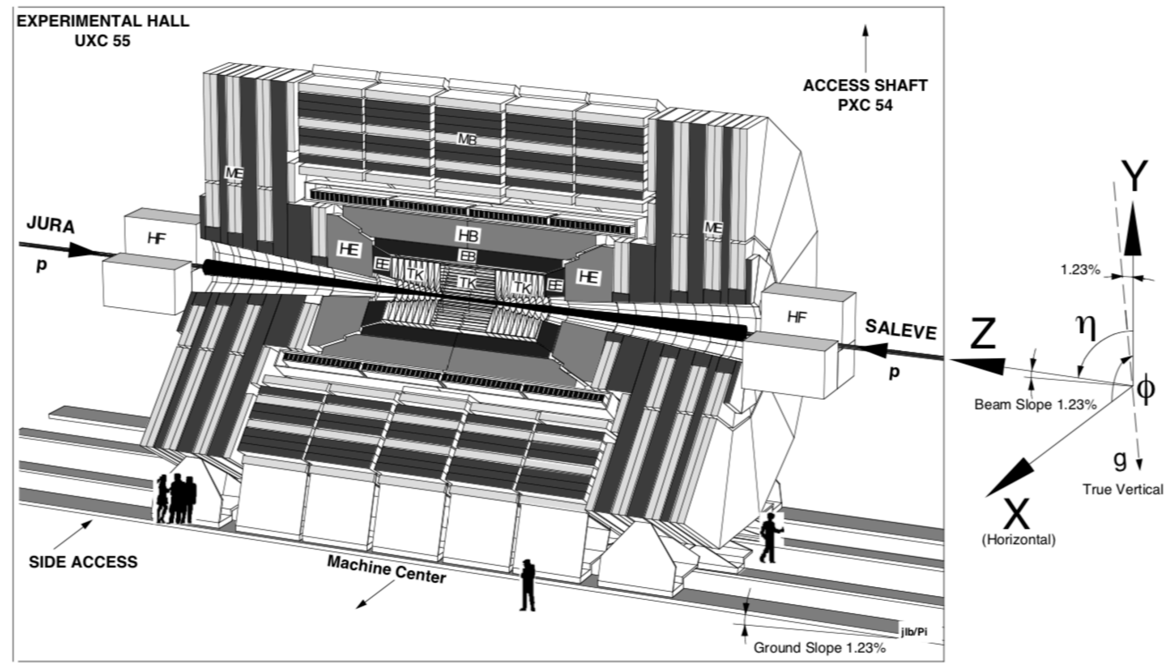

Figure 3.2: Coordinate system of the CMS detector.

The CMS detector consists of 5 main sub-structure starting from inside to outside laid out as the ‘Inner Tracker’, the ‘Electromagnetic Calorimeter (ECAL)’, the ‘Hadron Calorimeter (HCAL)’, the ‘Solenoid Magnet’ and the ‘Muon System’.

3.1. Inner Tracking System

The inner trackers are designed for the precise measurement of the bent trajectories of the charged particles under the influence of the magnetic field provided by the solenoid magnet. The tracking system can track both the primary particles produced from the hadron collisions in the beam pipe and the secondary particles that result from the decays of the primary particles. The two trackers of the inner tracking system are 'the pixel tracker' and 'the strip tracker'. The trackers surround and occupy the closest space to the beam pipe in the CMS detector, the pixel tracker being the closest.

The Pixel Tracker consists of four barrel and three endcap disk layers [8]. The tracker comprises 124 million pixels being each pixel module has the shape of 100×150 μm^2 with a thickness of 250 μm. The pixel tracker covers the pseudorapidity of $|\eta| < 2.5$. The Pixel Detector is part of the detectors used for the luminosity measurements. Thus, the detailed introduction of this detector will be explained in Section 5.2.1.

The Silicon Strip Tracker comprises a total of 9.6 million silicon strips. The barrel region of the tracker is divided into two parts as 'Tracker Inner Barrel (TIB)' and 'Tracker Outer Barrel (TOB)'. The TIB and TOB are made of 4 and 6 layers using silicon sensors with a thickness of 320 μm and 500 μm. Similarly, the endcaps of the strip tracker are divided into two as the 'Tracker End Cap (TEC)' and the 'Tracker Inner Disks (TID)'. Each TEC consists of 9 disks covering the range of 120 cm $<$ |z| $<$ 280 cm, and each TIB comprises 3 smaller disks that occupy the region between the TIB and the TEC, as shown in Figure 3.3 [9].

3.2. Electromagnetic Calorimeter

The electromagnetic calorimeter (ECAL) is a hermetic and homogeneous calorimeter that measures the energy composition of the particles by the interaction through electromagnetic force. It uses 61200 and 7324 lead tungstate ($PbWO_4$) scintillating crystals that constitute the barrel part and endcaps.

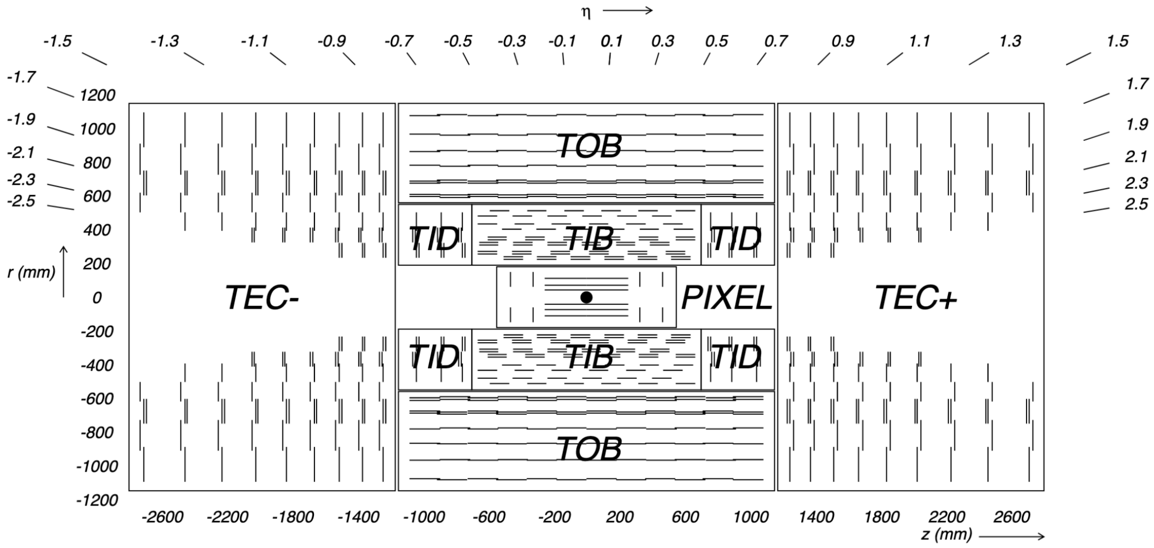

Figure 3.3: Schematic of inner tracker showing the each layers of the strip trackers and their coordinate coverage.

Additionally, the ECAL uses a preshower detector located in front of the endcap crystals. The photodetection is done by the 'Avalanche Photodiodes (APDs)' in the barrel and 'Vacuum Phototriodes (VPTs)' in the endcap.

The characteristics of $PbWO_4$ crystals such as high density (8.28 g/cm^3) and short radiation length (0.89 cm) allows a compact yet fine granularity and radiation-resistant calorimeter. Additionally, the decay time of the $PbWO_4$ scintillation is about 80% of the light in 25 ns, corresponding roughly the same time window as the LHC bunch crossing time.

The Barrel (EB) is located 129 cm away from the vertex formed as 36 identical 'supermodules' each having half the barrel length covering the range of $0 < |\eta| < 1.479$. The barrel crystals have a cross section of 22×22 mm^2 and a length of 230 mm.

The Endcap (EE) has an inner radius of 314 cm and covers a pseudorapidity range of $1.479 < |\eta| < 3.0$. The EE consists of 2 semi-circular aluminum plates that house 5x5 crystal structures called 'supercrystals'. The EE crystals have a cross section of 28.6×28.6 mm^2 and a length of 220 mm.

3.3. Hadron Calorimeter

The hadron calorimeter (HCAL) surrounds the ECAL with the separated barrel and endcap parts. Together with the ECAL, the HCAL completes the calorimeter system that provides a good hermeticity for the measurement of the missing transverse energy $E_{\mathrm{T}}^{\mathrm{miss}}$. Hence, the HCAL is designed to contain most of its material inside the solenoid magnet, except for an additional layer of scintillators placed outside of the magnet referred to as the 'hadron outer'. The HCAL uses brass as the absorber material due to its short length of interaction and being non-magnetic. The extensive use of the absorber material limits the space left for the active material. Thus, the HCAL uses fibre that consists of plastic scintillator tiles that form a 3.7 mm thick scintillator layers. The photodetection is performed using the readout system of multi-channel 'Hybrid Photodiodes (HPDs)'. The HCAL consists of 5 sub-parts: The 'hadron barrel', the 'hadron outer', the 'hadron endcap', and the 'hadron forward' as illustrated in Figure 3.4 [9].

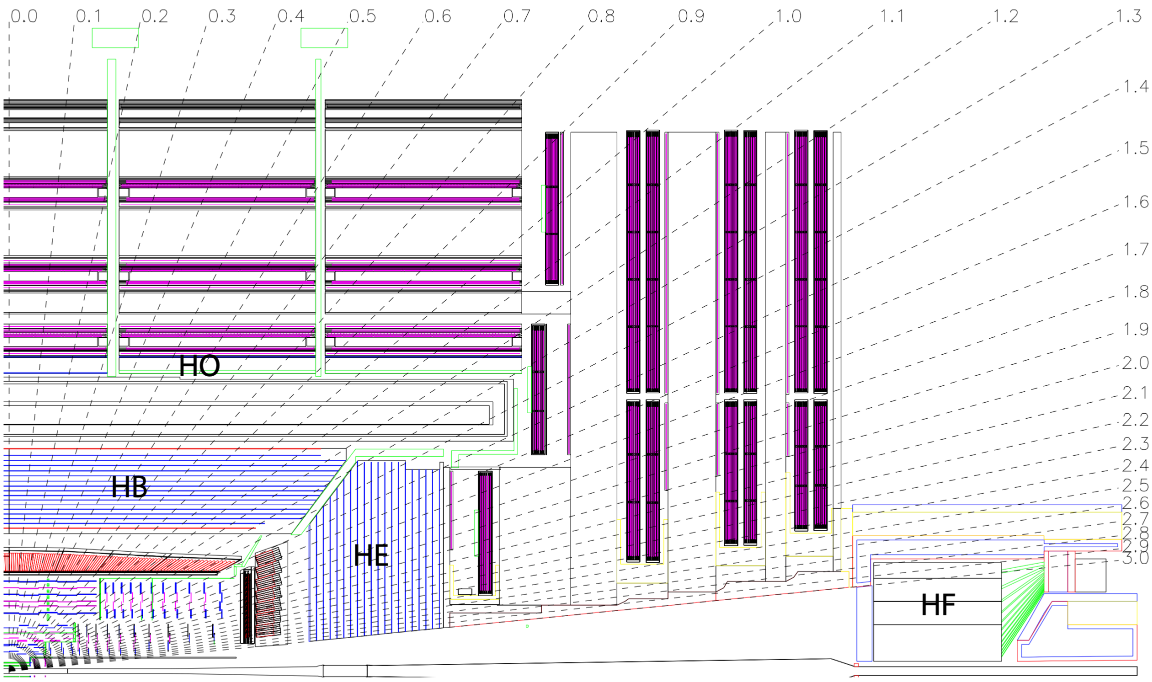

Figure 3.4: Longitudinal view of the hadron calorimeters showing the locations of the hadron barel, the hadron outer, the hadron endcap, and the hadron forward.

The Hadron Barrel (HB) has 32 towers covering a pseudorapidity of $|\eta| < 1.4$. The HB is designed as 2 half barrels providing a single longitudinal readout samling. The HB comprises 15 brass plates of 5 cm thick and additional two steel plates with 2 cm thickness for the structural strength. Furthermore, the particles passed the ECAL go through a 9 mm thick layer of scintillators instead of an absorber layer or a regular 3.7 mm scintillator layer.

The Hadron Outer (HO) is located right outside of the vacuum tank of the solenoid magnet and covers the region of $|\eta| < 1.26$. It consists of scintillators with 10 mm thickness acting as 'tail-catchers' that detect the leaked hadron showers through the HB. The HO increases the effective interaction length of the HCAL, resulting in a reduction in the tails of the energy resolution function and increasing in the resolution of the $E_{\mathrm{T}}^{\mathrm{miss}}$.

The Hadron Endcap (HE) covers the pseudorapidity region $1.3 < |\eta| < 3.0$, and consists of 2304 towers. Each HE layer has 14 η towers with 5° ϕ segmentation for the 5 outermost towers and 10° ϕ segmentation for the 8 innermost towers.

The Hadron Forward (HF) is located at 11.2 m from the interaction point, covering a range of $3.0 < |\eta| < 5.0$. It consists of steel/quartz fibre that constitutes 900 towers and 1800 channels. The HF is one of the detectors used for the luminosity measurements, as described in Section 5.1.5.

3.4. Solenoid Magnet

CMS uses a superconducting solenoid magnet designed to reach a nominal 4 T magnetic field with a length of 12.5 m and 220 tonnes of mass. The magnet constitutes the centerpiece of the detector design since the direction of the magnetic field directly decides the path that charged particles would follow. It is made of superconducting Niobium-Titanium (NiTi) wires powered by 20 kA to reach a magnetic field of 3.8 T.[8] In order to reach a field of 3.8 T, the winding of the magnet is designed as 4 layers due

[8]The magnet is operated at 3.8 T to increase its lifetime and stability.

to the high ampere requirements per turn needed (41.7 MA for a turn). The magnet also houses the inner tracker, ECAL, and HCAL inside within its radius of 5.9 m.

3.5. Muon System

Muons have a mean lifetime of 2.2 μs, yet it is much longer than many other known particles. This is because the decay process of a muon is dominated by the 'weak force' rather than stronger forces such as 'strong force' and 'electromagnetic force'. Hence, muons are less affected by the radiative losses caused by the tracker material. This puts the muon studies at high importance. For instance, the signal for the Higgs boson decay into four leptons is called 'gold plated' for the case where all four leptons are muons ($\mathrm{H} -> \mathrm{ZZ}^* -> 4\mu$), due to the low background of the process [7]. Moreover, the name of the Compact Muon Solenoid indicates how vital the muon studies are for the CMS experiment from the design.

The muon system is located outside of the solenoid magnet making it the outermost detector of CMS. The three functions that the muon system primarily has are muon identification, momentum measurements, and triggering. The solenoid magnet and the steel yokes placed in between the layers of the muon system allow CMS to have a homogenous magnetic field resulting in good momentum resolution and trigger capabilities. The yokes also serve as a hadron absorber improving the muon identification.

Similar to the other sub-detectors of CMS, the muon system is also inherited the cylindrical shape of the CMS detector by employing a central section (the barrel) that covers the pseudorapidity of $|\eta| < 1.2$ and a forward section (the endcap) covering $|\eta| < 2.4$. Each of the endcap detectors consists of 4 disks that enclose both sides of the barrels. The muon system uses three types of gaseous detectors for the identification of the muons [10]: The 'Drift Tube (DT)' in the barrel, the 'Cathode Strip Chamber (CSC)' in the endcap, and the 'Resistive Plate Chamber (RPC)' in both the barrel and endcap.

The Drift Tube consists of 4 stations located in between the flux return plates. For the first 3 stations, each station contains 8 chambers divided into two groups of 4. The two groups of 4 chambers are separated as much as possible for the maximum angular resolution. Furthermore, each chamber is arranged with an offset of a half drift cell with respect to the next one for maximum efficiency and a gapless design. In 2018, the DT was added in the luminosity measurements for the stability and linearity studies, which will be discussed in Section 5.1.6.

The Cathode Strip Chambers are located on both sides of the endcaps of the muon system due to having a high muon rate and a large and non-uniform magnetic field in the endcaps. The endcaps house 4 stations of CSCs as each of them are interspersed between the flux return plates. Thus, the CSCs provide a robust recognition of patterns for selecting the non-muon interactions as backgrounds and improving the efficiency of the hits-matching of the other sub-detectors.

The Resistive Plate Chambers are complementary dedicated trigger systems implemented in both the barrel and the endcaps of the muon system due to their fast, independent, and highly-segmented trigger capabilities with a sharp p_T threshold [7]. The RPCs are double-gap chambers covering the pseudorapidity of $|\eta| < 1.6$. There are 6 layers of RPCs located in the barrels, distributed as 2 for the first 2 stations and 1 for each of the other 2 stations. There is 1 layer of the RPCs in each of the first 3 stations of the endcaps to use coincidences efficiently between the stations for better triggering.

4. LUMINOSITY MEASUREMENTS

In this chapter, we will briefly define luminosity and its derivation from colliding bodies as well as luminometers used at CMS. Sections 4.1 and 4.2 will roughly follow the source material of 'Concept of luminosity' by 'Werner Herr and Bruno Muratori' [11]. The definition and the derivation for the luminosity will stay generalized until Chapter 6 where the methodology for the measurement of the luminosity at CMS is introduced.

4.1. The Definition of Luminosity

One of the most important aspects of particle physics experiments is the energy available to produce new particles. This requires minimizing the loss of center of mass energy for the colliding beams during the motion. Second to the energy loss, the number of interactions is equally important for studying new particles. The quantity that measures these interactions is called luminosity. Luminosity represents a ratio between the rate of the recorded events[9] and a cross section[10] of the process.

$$\mathcal{L} = \frac{R(t)}{\sigma_p} \tag{4.1}$$

where σ_p is the production cross section and $R(t)$ is the raw number of observed quantity (hits, tracks, etc.) per second,

$$R(t) = \frac{dR}{dt}. \tag{4.2}$$

The unit of the cross-section is cm^2. Thus, the unit of the luminosity becomes $\mathrm{cm}^{-2}\mathrm{s}^{-1}$.

---

[9] Results of a fundamental interaction between sub-atomic particles [12].

[10] A measure of the probability for a certain process to happen when the required interaction takes place [13].

4.2. Luminosity of Colliding Bodies

4.2.1. Fixed Target Collisions

Luminosity calculation of a fixed target collision experiment requires consideration of both the incoming beam and the stationary target properties. Assuming the target has a homogeneous distribution with constant density function (ρ_T) and is large enough that the distribution of the incoming beam is not important. Figure 4.1 shows a visual representation of the fixed target collision.

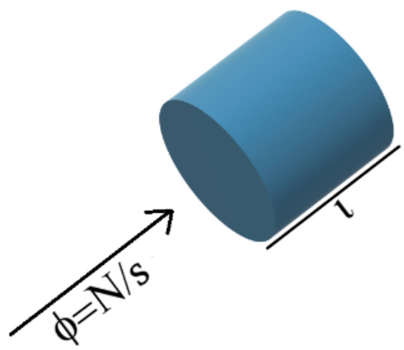

Figure 4.1: Schematic view of a fixed target collision.

Then, the rate of this interaction can be written as,

$$R(t) = \frac{dR}{dt} = \phi.\rho_T.l.\sigma_p \tag{4.3}$$

where ϕ is the flux of the incoming beam as number particle per second (N/s), $\rho(T)$ is the density function of the target, l is the length of the target, and σ_p is the production cross section. Comparison of Equations 4.1 and 4.3 gives the luminosity of a fixed target collision to be,

$$\mathcal{L}_{FT} = \phi.\rho_T.l. \tag{4.4}$$

4.2.2. Colliding Beams

In the case of two beams colliding, each beam becomes both ‘incoming’ and ‘target’ simultaneously. Thus, the beam distribution cannot be ignored and has to be considered as a 3-D distribution function.

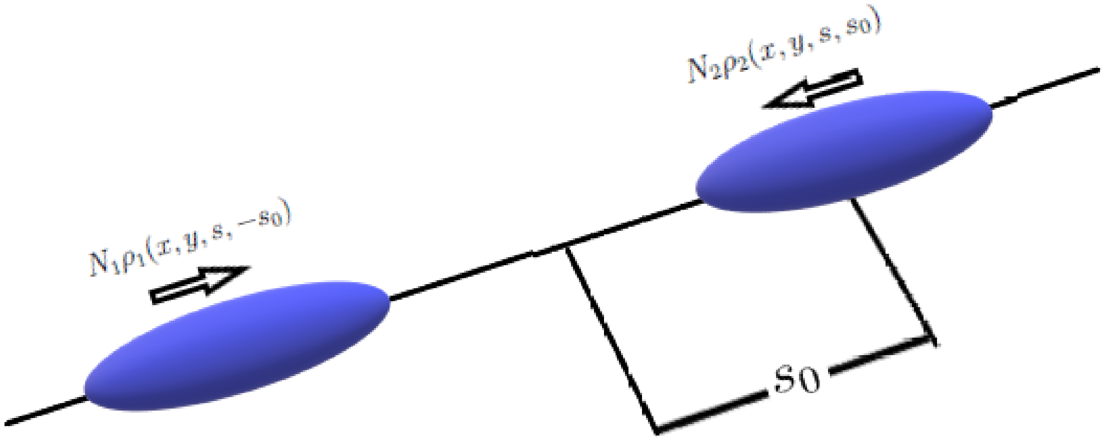

Figure 4.2: Schematic view of a beam-beam collision.

In the figure above (fig. 4.2) N_1 and N_2 represents particle number in their respective beam bunches, and ρ_1, ρ_2 stand for the time-dependent density distribution functions of the bunches. The propagating axis of the bunches is taken as ‘s’, and $s_0 = ct$ is the ‘time’ variable of the distribution functions declaring the distance of the two bunches to the interaction point as a function of time.

The luminosity integral for these two overlapping bodies become,

$$\mathcal{L} \propto K \int\int\int\int_{-\infty}^{+\infty} \rho_1(x, y, s, -s_0)\rho_2(x, y, s, s_0)dxdydsds_0. \tag{4.5}$$

Assuming two bunches meet at $s_0 = 0$, one can write the kinematic factor K as,

$$K = \sqrt{\frac{(\vec{v}_1 - \vec{v}_2)^2 - (\vec{v}_1 \times \vec{v}_2)^2}{c^2}}. \tag{4.6}$$

The next step will require two important assumptions to be made, bunches collide with a head-on collision ($\vec{v}_1 = -\vec{v}_2$), and all densities are uncorrelated in all planes. The former, with the consideration of bunches are traveling almost at the speed of light, gives the kinematic factor to be,

$$K = 2|\vec{v}_1| = 2|\vec{v}_2| \cong 2. \tag{4.7}$$

The latter will let us factorize the density distribution functions, which is crucial to write the following integral of the luminosity for overlapping bodies.

$$\mathcal{L} = 2N_1N_2fN_b \int\int\int\int_{-\infty}^{+\infty} \rho_{1x}\rho_{1y}\rho_{1s}(s-s_0)\rho_{2x}\rho_{2y}\rho_{2s}(s+s_0)dxdydsds_0 \tag{4.8}$$

where N_1 and N_2 are intensities of two colliding bunches, N_b is the number of bunches in one beam and f is the revolution frequency of the bunches in the accelerator. For the LHC this frequency is $f_{LHC} = 11245.6Hz$.

To evaluate this integral (4.8), one should know all the distribution functions in all planes, which is not always possible to do analytically and numerical integration may be required. However, it is often justified to assume these distributions to be 'Gaussian'. The Gaussian distribution assumption and the assumption that 'all densities are uncorrelated in all planes' will bring out the uncertainty of 'x-y correlation' which will be covered in Chapter 7.6.

The densities of the bunches are profiled as Gaussian distribution of the form,

$$\rho_{ik}(k) = \frac{1}{\sigma_k\sqrt{2\pi}}\exp(-\frac{k^2}{2\sigma_k^2}) \quad \text{where} \quad i = 1,2, \quad k = x,y, \tag{4.9}$$

and

$$\rho(s \pm s_0) = \frac{1}{\sigma_s\sqrt{2\pi}}\exp(-\frac{(s \pm s_0)^2}{2\sigma_s^2}). \tag{4.10}$$

Furthermore, assuming equal beams (i.e, $\sigma_{1x} = \sigma_{2x}, \sigma_{1y} = \sigma_{2y}, \sigma_{1s} = \sigma_{2s}$) and plugging Equations 4.9 and 4.10 into Equation 4.8 brings,

$$\mathcal{L} = \frac{2N_1N_2fN_b}{(\sqrt{2\pi})^6\sigma_x^2\sigma_y^2\sigma_s^2}\int\int\int\int_{-\infty}^{+\infty} e^{-\frac{x^2}{\sigma_x^2}}e^{-\frac{y^2}{\sigma_y^2}}e^{-\frac{s^2}{\sigma_s^2}}e^{-\frac{s_0^2}{\sigma_{s0}^2}}\,dxdydsds_0. \tag{4.11}$$

Using the well-known formula of,

$$\int_{-\infty}^{+\infty} e^{-\alpha t^2}dt = \sqrt{\frac{\pi}{\alpha}}, \tag{4.12}$$

Equation 4.11 yields,

$$\mathcal{L} = \frac{N_1N_2fN_b}{4\pi\sigma_x\sigma_y}. \tag{4.13}$$

The luminosity of the two Gaussian beams colliding head-on (Equation 4.13) is a well-known expression and it mainly depends on the number of particles per bunch and the beam sizes.

To generalize this solution one can assume different sized bunches in x and y with an approximately equal bunch lengths (i.e. $\sigma_{1x} \neq \sigma_{2x}, \sigma_{1y} \neq \sigma_{2y}, \sigma_{1s} \approx \sigma_{2s}$),

$$\mathcal{L} = \frac{N_1N_2fN_b}{2\pi\sqrt{\sigma_{1x}^2+\sigma_{2x}^2}\sqrt{\sigma_{1y}^2+\sigma_{2y}^2}}. \tag{4.14}$$

The luminosity does not appear to depend on bunch length due to the assumption of uncorrelated density distributions. Equation 4.14 can be further generalized by replacing 'head-on collision' assumption with 'offset collisions' and/or addition of 'bunch-crossing angle'. However, as it will be shown in Chapter 6.1 the van der Meer (vdM) scan methodology introduces 'convoluted beam widths (Σ_x, Σ_y)' which declares both bunches' properties simultaneously, removing the need for knowing $\sigma_{1x}, \sigma_{2x}, \sigma_{1y}, \sigma_{2y}$ individually.

5. LUMINOMETERS AT CMS

There are six detectors used for monitoring and measuring luminosity at CMS: the CMS silicon pixel detector, the drift tubes in the barrel (DT), the Hadronic Forward Calorimeter (HF), the Fast Beam Conditions Monitor (BCM1F) [14], the Pixel Luminosity Telescope (PLT) [15], and the Radiation Monitoring System for the Environment and Safety (RAMSES) detector. These detectors can be categorized into online and offline luminometers. The online luminometers can deliver per bunch luminosity data in real-time, in contrast to the offline luminometers, where the data collected at the end of each fill needs to be analyzed to deliver luminosity measurement.

5.1. The Online Luminometers

The online luminometers (PLT, BCM1F, and HF) can deliver instantaneous luminosity data in real-time through a specialized data acquisition system known as BRILDAQ. The DT being able to deliver luminosity measurement online, its inherent dependence on CMS DAQ makes it a special case of an online luminometer. Nevertheless, the DT will also be presented under the online luminometers.

5.1.1. The BRILDAQ System

The BRILDAQ is specialized in the sense that it is independent of the main CMS DAQ. This allows the BRILDAQ to send luminosity and beam background information to LHC and CMS even when CMS is not running. The BRILDAQ data are displayed on online monitoring tools published to DIP for CMS and LHC to access, where DIP is a Data Interchange Protocol developed and being used at CERN [16]. The data are recorded as ‘hd5’ files. After completing a fill, the recorded data are uploaded into the luminosity database (lumiDB), where it can be displayed using the BRIL Calculation (brilcalc) tool. The DT data from the main CMS DAQ are also available to BRILDAQ via an XDAQ flashlist, where XDAQ is a software product that handles the requirements of data acquisition of the CMS experiment [17].

The CMS silicon pixel detector ntuples obtained from CMS data and the RAMSES data from Timber (an open source content management system) are manually loaded to the lumiDB independently.

5.1.2. Zero-Counting Algorithm

Due to high pile-up, it is often not clear to distinguish single and multiple hits on the detector. To resolve this issue, a method called 'zero-counting algorithm' is employed. Zero-counting method is based on Poisson statistics that takes advantage of the assumption that signals in the detectors follows a Poisson distribution,

$$p(n) = \frac{\mu^n e^{-\mu}}{n!} \tag{5.1}$$

where the mean value μ can be derived from the probability of finding no signal, p(0) using the formula,

$$\mu = -ln[p(0)] = -ln[1 - p(\neq 0)]. \tag{5.2}$$

Then, the raw rate for a particular detector can be calculated as,

$$R(t) = \sum_i R_i(t) = f \sum_i \mu_i \tag{5.3}$$

where $f_{LHC} = 11245.6$ Hz for LHC and μ_i is the average number of measured signals per bunch crossing. Thus, the instantaneous luminosity is,

$$\mathcal{L}[Hz/\mu b] = \mu \frac{f_{LHC}}{\sigma_p}. \tag{5.4}$$

5.1.3. Pixel Luminosity Telescope

The PLT is a dedicated system for measuring the luminosity at CMS using silicon pixel sensors, installed in CMS in 2015. The PLT uses similar technology to the phase-0 CMS pixel detector (including the same sensors and readout chips), but takes advantage of a special 'fast-or' readout mode in the readout chips. The readout chips can deliver signals with a frequency of 40 MHz, which corresponds to the full machine bunch crossing frequency at LHC. Thus, the PLT provides online per-bunch luminosity with excellent statistical precision.

The PLT consists of 48 sensors arranged into 16 telescopes as each telescope caries 3 sensors. The sensors consist of 80 rows and 52 columns of pixels, with each pixel 150 μm wide and 100 μm high, for a total area of 8x8 mm^2. During 2018 running, only the central region of the sensors is used, consisting of a region of 26 columns by 38 rows wide (3.9x3.8mm) for the outer planes, and 24 columns by 36 rows (3.6x3.6mm) for the central plane. Each sensor is mounted on the x-y plane with the surface normal to be parallel to the z-axis, with the total length of the telescopes being approximately 7.5 cm. The telescopes are installed outside the CMS pixel end-caps, with eight telescopes arranged around the beam-pipe at each end of the detector.

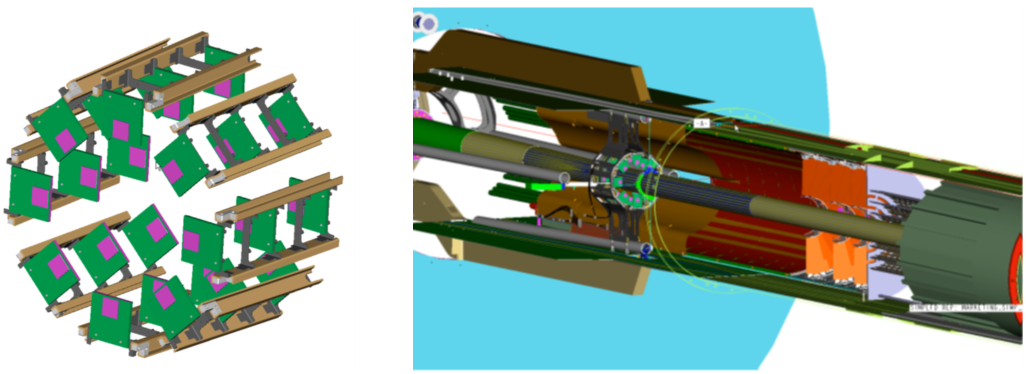

Figure 5.1: On the left, PLT telescope arrangement, and on the right, PLT placement in the CMS detector are shown.

The 'fast-or' readout is used to define 'triple coincidences', which are events where all three sensors in a single telescope read out a hit, indicating a track from the IP.

The rate of triple coincidences should then be proportional to the luminosity. To avoid issues where multiple tracks may only be read out as a single triple coincidence, the ‘zero-counting’ algorithm, discussed in Section 5.1.2, is employed.

The primary correction necessary for the PLT data comes from the presence of ‘accidentals’. Accidentals correspond to the cases where a triple coincidence is observed yet not caused by a track originating from the interaction point. This may be due to tracks from particles elsewhere (e.g., activated material surrounding the detector) or from a random coincidence of hits from different tracks (for example, two tracks that do not individually pass through all three planes of the PLT could combine to make a triple coincidence). The reduction in the active area of the PLT sensors is chosen to reduce these accidentals’ contribution, as the accidental rate depends strongly on the sensor area.

5.1.4. Fast Beam Condition Monitor

The BCM1F has been upgraded during the 2016–2017 extended year-end technical stop (EYETS) and consists of 24 sensors. The 24 sensors use three separate technologies: 10 poly-crystalline diamond sensors (pCVD), 10 silicon sensors, and 4 single-crystal diamond sensors (sCVD). The diamond sensors use two-pad metallization, while the silicon sensors use one pad, for a total of 38 readout channels with about 1 ns arrival time resolution. The BCM1F has a radius of 6.94 cm from the beam axis, 1.8 m away from the CMS IP. Due to each sensor type’s different properties, the three different sets of sensors are treated as separate luminometers. The pCVD measurement is used to represent BCM1F in the final luminosity output. Due to its excellent time resolution and spatial location, BCM1F is used for both luminosity measurements and measurements of machine-induced background (MIB). As incoming MIB particles and outgoing collision products are separated in time by 12.5 ns, the rate contribution due to MIB can be measured separately and used to correct the rate measured during the expected collision time. As with the PLT above, the ‘zero-counting’ algorithm is used to determine the mean rate μ for the luminosity calculation.

5.1.5. Hadronic Forward Calorimeter

The HF calorimeter was used to produce the primary CMS luminosity measurement during Run 1 and has continued to produce excellent luminosity measurements throughout Run 2. The HF measurement uses two different luminosity algorithms. The first one, the occupancy-based method (HFOC), uses the occupancy of the towers in HF by counting the number of towers with deposited energy above a noise threshold and then using the 'zero-counting' algorithm to determine the average occupancy μ. In 2017, a second algorithm that uses the sum-E_{T} (HFET) was developed. HFET uses the total sum of the transverse energy deposited in the HF to determine the μ. Both HFOC and HFET use two rings in the HF, the rings with $i_\eta = 38$ and 39, to ensure relatively uniform occupancy across the region considered. The HF luminosity is corrected for both efficiency loss due to radiation-induced aging and for afterglow (out-of-response) effects.

5.1.6. Drift Tubes

The DT measurement uses the rate of muon track stubs in the muon barrel track finder (MBTF). While the DT measurement is available online to BRILDAQ, as the MBTF is still part of the main CMS DAQ, this measurement is only available when the CMS DAQ runs normally, unlike the PLT, BCM1F, and HF. The DT algorithm does not provide bunch-by-bunch measurements and is thus useful only for the total luminosity measurement. Since the DT rates are generally lower than the other online luminometers, it is not practical to calibrate the DT directly using the dedicated vdM measurement. Instead, the DT measurement is cross-calibrated to other detectors. The good stability and linearity performance of the DT measurements make it useful addition as an offline reference luminometer.

5.2. The Offline Luminometers

5.2.1. The CMS Silicon Pixel Detector

The silicon pixel detector constitutes the innermost part of the CMS Tracker comprised of 124 million separate pixel detectors of size 100 μm x 150 μm. The detector is reliant on CMS DAQ and collects data only when 'Stable Beam' is declared during a fill which makes it unreliable to be used for online luminosity measurement. Although, the readout system is not designed for online luminosity, it is still capable of delivering precise luminosity data. Therefore, it is still an important part of the offline luminosity measurement. However, due to the required statistical precision, it is limited to deliver data of 5 selected bunches only for luminosity measurement. There are two methods employed for luminosity measurement using the silicon pixel detector, as it is with the HF.

The pixel cluster counting (PCC) method features very low occupancy of less than one per mil under pileup environments of $\mu = 25$ and shows excellent stability over time after correction. The methodology relies on the assumption that the mean number of pixel clusters per event (or bunch crossing) should be proportional to the number of interactions μ,

$$< N_{cluster} >=< N_{cluster/interaction} > \mu. \tag{5.5}$$

The number of interactions in turn is given by the proton-proton minimum bias cross-section σ_0,

$$\mu = \frac{\sigma_0}{f}\mathcal{L} \tag{5.6}$$

where $\mathcal{L}$ is the instantaneous luminosity and f_{LHC} is the orbit frequency of the LHC. The PCC visible cross section can be defined as,

$$\sigma_{\text{vis}}^{PCC} \equiv< N_{cluster/interaction} > \sigma_0, \tag{5.7}$$

then the relation of $\sigma_{\text{vis}}^{PCC}$ to the instantaneous luminosity becomes,

$$\mathcal{L} = \frac{< N_{cluster} > f}{\sigma_{\text{vis}}^{PCC}}. \tag{5.8}$$

The visible cross-section is determined using the vdM scan method for which the number of clusters recorded with the zero-bias trigger divided by the number of zero-bias events is measured for each scan point, the details of the vdM is discussed in Chapter 6. All reconstructed pixel clusters are considered for counting with two exceptions. First, pixel modules that are not fully operational throughout the 2018 data-taking period have been omitted from the sum. Second, all clusters originating in the pixel detector's innermost barrel layer are excluded from the sum since this layer is significantly affected by dynamic inefficiency caused by the harsh environment in terms of high particle and radiation density.

The vertex counting (VTX) method counts reconstructed pp collisions, which is considered one of the cleanest sources of low pileup luminosity estimates. Primary interaction vertices can be reconstructed using tracks that point back to a well-defined point in space with a precision of tens of microns. At high pileup, vertices often occur very close together; therefore, they are often indistinguishable for track reconstruction algorithms alone. However, in fills for calibration analyses (i.e vdM fills), the pileup is so low that there are usually only 0 or 1 pp collisions in a single crossing, and so concerns about non-linearity from vertex-merging does not arise.

Vertex reconstruction has at least 30% inefficiency but has no background. Consequently, vertex counting provides excellent profiles of beam shape overlaps. The VTX method's main drawback is that not enough data can be acquired to achieve good statistical precision for each bunch crossing.

As the vertex counting uses the same zero-bias data sample collected for PCC, only five bunch crossings in a vdM fill are typically considered by the DAQ.

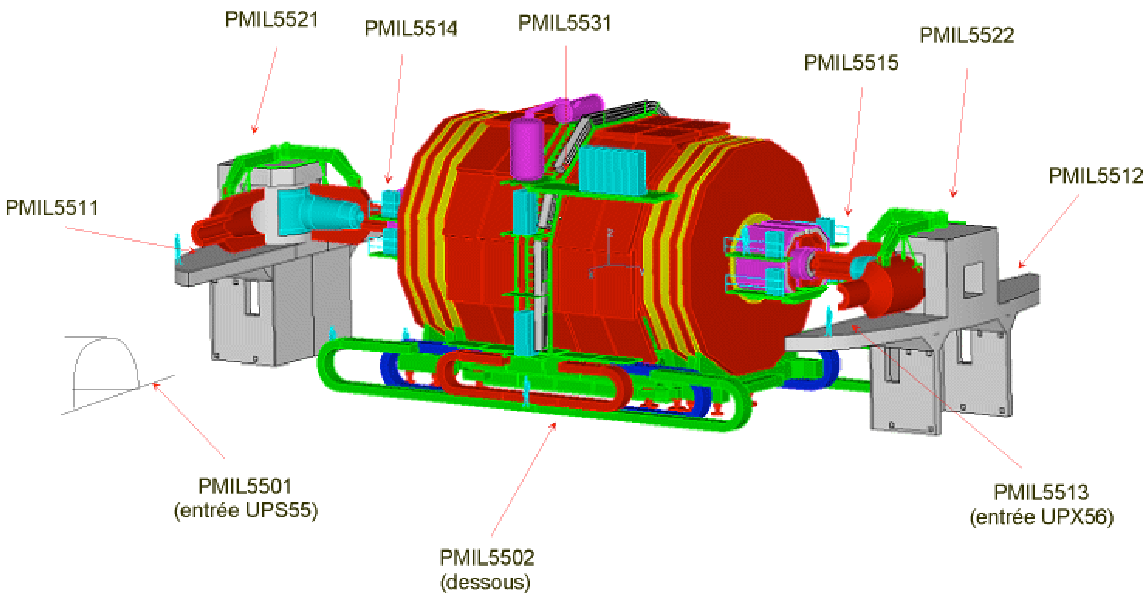

Figure 5.2: Location of the 10 individual RAMSES detectors in the CMS cavern.

5.2.2. The RAMSES

RAMSES is a CERN radiation and environmental monitoring system, it is part of the Radiation and Environment Monitoring Unified Supervision (REMUS) system. It was introduced in the beginning of the LHC operation, and consists of 350 monitors in the LHC underground areas as well as on the surface, around the CERN perimeter. Originally, there were 8 monitors installed in the CMS experimental cavern, with an additional 2 detectors installed during Run 2. Figure 5.2 shows the location of the RAMSES detectors around CMS. The sensor itself is a plastic ionization chamber filled with 3 L of air at atmospheric pressure. The chamber has a cylindrical shape, and the walls are coated with 4 mm of PE graphite. It detects photons within the energy range of 50 keV to 7 MeV (reference calibration at 662 keV). The collected current on the anode is translated into the ambient dose equivalent rate providing measurements in the range 5 μSv/h to 500 μSv/h (corresponding to a current in the range $1.4\text{x}10^{-13}$–$1.4\text{x}10^{-8}$ A). The broad measurement range allows real-time monitoring in the working environment during LHC operation as well as during stops and shutdowns. The measurement interval varies from 1 to 3600 s, and both instantaneous and mean (typically averaged over 60 s) values are saved.

The main task of RAMSES is to monitor radiation levels and ensure personnel safety, not equipment protection. It can generate alarms and interlocks. RAMSES allows remote supervision and provides permanent data storage in the REMUS database accessible directly from ERGO (Environment and Radiation Graphic Observer) which is a data visualisation tool, providing direct access to all measurements and events recorded by the REMUS system. The data are published via DIP and Timber, facilitating further data analysis. Although RAMSES is not designed as a luminometer, the rate observed in the RAMSES detectors do function quite well as a luminosity measurement. Due to a low overall rate, it cannot make bunch-by-bunch measurements and cannot be independently calibrated using a vdM scan.

Nevertheless, it is observed that the Ramses exhibited excellent linearity and stability performance over the course of the 2018 run. Thus, the detector is added as a new luminometer for stability and linearity cross-check of online luminometers in 2018.

6. METHODOLOGY OF LUMINOSITY MEASUREMENTS

In Chapter 5, the rate (R(t)) part of the Equation 5.1 is explained. For the purpose of calculation of luminosity, the cross-section of the process (σ_p) also needs to be known. Since protons are not elementary particles and have an inner structure made of gluons and quarks, it is theoretically challenging to assign a known cross-section to their interactions. Instead, in 1968 a method for the measurement of the cross-section was pioneered by Simon van der Meer [18]. The so-called 'vdM scan' methodology lets scientists measure the cross-section visible by the luminometers (σ_{vis}) by sweeping beams transversely, thus, gathering interaction information experimentally for each detector separately.

In this chapter, vdM scan methodology will be explained together with the 2018 vdM program. Emittance scans, being smaller vdM scans, will also be introduced as it is a relatively new method for gathering stability and luminosity information throughout the year.

6.1. The van der Meer Scan Methodology

In order to obtain an absolute calibration of luminosity, the cross-section σ_{vis} needs to be measured for all luminometers of interest. For this, special fills are performed once or twice a year using vdM scans.

Assuming there is no crossing angle between the beams and they are separated by $(\Delta x, \Delta y)$ in respective axes, the instantaneous luminosity of the colliding bunch pair can be expressed as,

$$\mathcal{L}(\Delta x, \Delta y) = N_1 N_2 f \int\int_{-\infty}^{+\infty} \rho_1(x,y)\rho_2(x+\Delta x, y+\Delta y)dxdy \tag{6.1}$$

where N_1 and N_2 are the number of protons in the two colliding bunches, f_{LHC} = 11245.6 Hz is the orbit frequency of the LHC, and ρ_1 and ρ_2 are the proton densities of the colliding bunches in beams 1 and 2, respectively. The total bunch populations N_1 and N_2 can be measured to good precision directly, whereas the bunch proton density functions ρ_1 and ρ_2 are difficult to measure precisely. The LHC experiments use the vdM scan method to measure integral over the bunch proton densities. For the vdM scan method to work, it is assumed that the two bunch proton densities are factorizable in x and y which results in factorization of the integral in Equation 6.1 as,

$$\int\int_{-\infty}^{+\infty} \rho_1(x,y)\rho_2(x+\Delta x, y+\Delta y)dxdy = \int_{-\infty}^{+\infty} \rho_1(x)\rho_2(x+\Delta x)dx \times \int_{-\infty}^{+\infty} \rho_1(y)\rho_2(y+\Delta y)dy. \tag{6.2}$$

The possible bias introduced by this assumption will be discussed in the Section 7.6. If we integrate both sides of the Equation 6.2 independently in Δx and Δy while other respective separation is kept fixed, we get,

$$N_1 N_2 f \int_{-\infty}^{+\infty} \rho_1(x)\rho_2(x+\Delta x_0)dx = \int_{-\infty}^{+\infty} \mathcal{L}(\Delta x_0, \Delta y)d(\Delta y), \tag{6.3}$$

and

$$N_1 N_2 f \int_{-\infty}^{+\infty} \rho_1(y)\rho_2(y+\Delta y_0)dy = \int_{-\infty}^{+\infty} \mathcal{L}(\Delta x, \Delta y_0)d(\Delta x) \tag{6.4}$$

where Δx_0 and Δy_0 represent head-on working point of the respective axes, i.e. $\Delta x_0 = 0$ and $\Delta y_0 = 0$. Using the Equations 6.1, 6.3 and 6.4 together yields,

$$\int_{-\infty}^{+\infty} \rho_1(x)\rho_2(x+\Delta x_0)dx = \frac{\mathcal{L}(\Delta x_0, \Delta y_0)}{\int_{-\infty}^{+\infty} \mathcal{L}(\Delta x, \Delta y_0)d(\Delta x)}, \tag{6.5}$$

and

$$\int_{-\infty}^{+\infty} \rho_1(y)\rho_2(y+\Delta y_0)dy = \frac{\mathcal{L}(\Delta x_0, \Delta y_0)}{\int_{-\infty}^{+\infty} \mathcal{L}(\Delta x_0, \Delta y)d(\Delta y)}. \tag{6.6}$$

The integrations over Δx and Δy above are done experimentally by scanning the two beams against each other in steps as shown in the Section 6.1.2. The integrals on the right hand side of the Equations 6.3 and 6.4 are evaluated by measuring the luminometer rate as a function of the beam-beam separations (i.e. R(Δx, Δy)) since the luminosity is linearly correlated with the rate measured.

The Equation 6.1 can be expressed in terms of rate and head-on points (Δx_0 and Δy_0),

$$\mathcal{L}(\Delta x_0, \Delta y_0) = N_1 N_2 f \frac{R(\Delta x_0, \Delta y_0) R(\Delta x_0, \Delta y_0)}{\int_{-\infty}^{+\infty} R(\Delta x, \Delta y_0) d(\Delta x) \int_{-\infty}^{+\infty} R(\Delta x_0, \Delta y) d(\Delta y)} \tag{6.7}$$

where the luminosity is replaced by the measurable $R(\Delta x, \Delta y)$. The vdM procedure is a physical convolution of the two beams, thus, it is convenient to re-write the integrals over the rate scan curves in terms of the convoluted widths (Σ_x and Σ_y) of the two beams (also known as the beam overlap widths). Convoluted beam widths (Σ_x and Σ_y) are defined as,

$$\Sigma_x = \frac{1}{\sqrt{2\pi}} \frac{\int_{-\infty}^{+\infty} R(\Delta x, \Delta y_0) d(\Delta x)}{R(\Delta x_0, \Delta y_0)}, \tag{6.8}$$

and

$$\Sigma_y = \frac{1}{\sqrt{2\pi}} \frac{\int_{-\infty}^{+\infty} R(\Delta x_0, \Delta y) d(\Delta y)}{R(\Delta x_0, \Delta y_0)}. \tag{6.9}$$

Then, the luminosity becomes,

$$\mathcal{L}(\Delta x_0, \Delta y_0) = \frac{N1 N_2 f}{2\pi \Sigma_x \Sigma_y}. \tag{6.10}$$

Substituting the Equation 6.10 in the Equation 4.1 gives the final formula for the visible cross section,

$$\sigma_{\text{vis}} = \frac{2\pi \Sigma_x \Sigma_y R(\Delta x_0, \Delta y_0)}{N_1 N_2 f}. \tag{6.11}$$

The important part of the Equation 6.11 is all quantities on the right hand side of the formula are measurable by experiment. The determination of the $R(\Delta x_0, \Delta y_0)$ for different luminometers is already covered in the Chapter 5. In the next section, determination of Σ_x and Σ_y from fits of the scan curves, based on luminometer rate measurements during the VdM scans, will be shown.

6.1.1. Extraction of Sigma Visible Constants

During the vdM scans beams are separated from each other in x and y axes in different scans by Δx and Δy values. Step by step beams are convoluted until the head-on collisions are acquired and then scanning proceeds in the other direction as shown in of Figure 6.1-left.

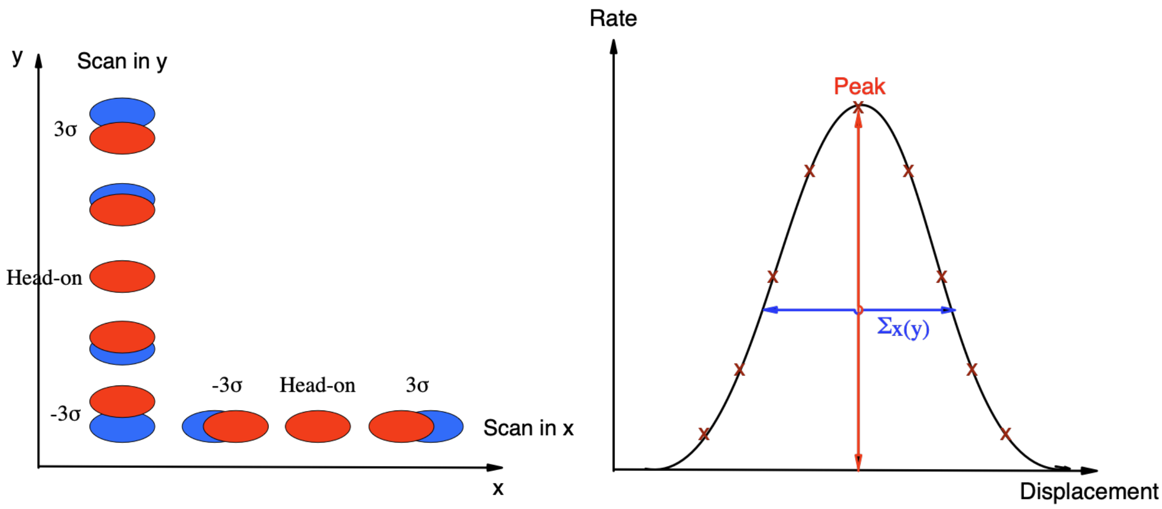

Figure 6.1: On the left, the vdM scan progress is shown in x and y separately. On the right, the rate data collected from each scan point is illustrated according to their displacement points, the peak being the head-on position.

Each scan point with a different displacement value corresponds to a red ‘x’ data point in Figure 6.1-right. A ‘single Gaussian’ fit is employed to obtain the beam overlap widths (Σ_x and Σ_y) as well as the normalized rates (r_x and r_y). Although other fit models like ‘double Gaussian’ (fitted to the tails and the peak separately) are checked, the most stable fits were obtained from the single Gaussian model since the background correction from super-separation scans makes the second Gaussian to the tails obsolete.

The scan data are collected for per scan and per bunch crossing ID number (BCID). For each BCID the visible cross sections are then calculated using the Equation 6.11, i.e.,

$$\sigma_{\text{vis}} = 2\pi\Sigma_x\Sigma_y\langle n\rangle_0 \tag{6.12}$$

where

$$\langle n\rangle_0 = \frac{1}{2}(r_x + r_y), \tag{6.13}$$

as r_x and r_y denote the amplitudes of the fitted scan curves which are already normalized to the bunch intensities. The r_k quantities above represents the rate per bunch, so their relation to the R_k can be given by,

$$fr_k = \frac{R_k}{N_1N_2}, \quad k = x, y. \tag{6.14}$$

In Figure 6.2 two fits to data are given for the PCC detector in scan 1 on the left and in scan 2 on the right. The plot on the left shows the scanning in the x-direction whereas the plot on the right shows scanning in y-direction. Both figures are for the BCID 865.

After the calculation of σ_{vis} values for each BCID, the values are weighted averaged according to their uncertainties in order to find σvis of the scan.

6.1.2. The 2018 vdM Scan Program

The vdM scans were performed during LHC fill 6868 on June 30th–July 1st, 2018, at a center-of-mass energy of 13 TeV. The LHC filling scheme had 124 colliding bunch pairs at IP5 widely spread over the orbit to reduce long-range beam-beam effects and detector afterglow. Special LHC beam optics were used for the fill, with $\beta^* \approx 19$ m and a transverse emittance of $\epsilon_N \approx 3.0\ \mu m$.

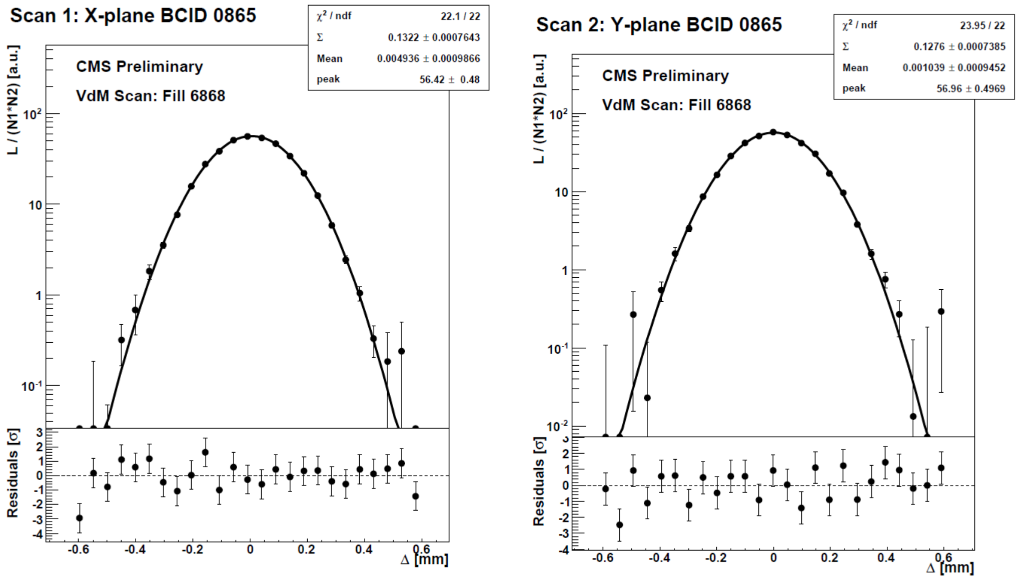

Figure 6.2: Normalized rates and the resulting fitted single Gaussian scan curves as a function of the beam separation (Δ) for a single bunch (BCID 865) as recorded by PCC for a scan in the x (left) and y-directions (right).

For 2018, the emittance of the bunches was selected in two different ranges to allow for studies of bunches with different beam sizes. The resulting beam size σ_b at the beginning of the fill was in the range of approximately 85–95 μm in x and 80–90 μm in y, increasing over time in the x dimension and decreasing over time in the y dimension. No crossing angle was used for collisions at ATLAS and CMS. The resulting pileup was approximately $\mu = 0.6$, much lower than a regular physics fill.

The bunch intensities were approximately 7 to 9 $\times$ 10^{10} protons per filled bunch, resulting in a total beam intensity of approximately 11 $\times$ 10^{12} protons per beam. The total beam intensities were measured with the DC Current Transformers (DCCT) [19], and the bunch currents were measured with the Fast Beam Current Transformers (FBCT) [20] and cross-checked with the Beam Quality Monitors (BQM). Ghost and satellite fractions are estimated by the LHC longitudinal density monitors (LDM) [21, 22]. The beam orbit was monitored using two systems, the DOROS beam position monitors (BPMs) [23] located near IP5, and the arcBPMs located in the LHC arcs adjacent to CMS. The orbit was also tracked using beam spot movements based on reconstructed vertices.

To collect the most possible data for PCC for large beam separations, CMS gated the zero-bias triggers on 5 bunch pairs (IDs 265, 865, 1780, 2192, and 3380) and recorded events with a total rate of 27.7 kHz. For the online luminometers (PLT, BCM1F, HF), all colliding bunches were recorded.

The CMS vdM scan program consisted of a total of seventeen x-y scan pairs. Five pairs were completed before CMS data-taking was interrupted by a smoke alarm at CMS, which necessitated a significant delay (approximately 7.5 h) in order to recover from the alarm and return the detector (which was automatically shut off by the alarm) to operational status. Because of the need to taking the two pairs of beam imaging scans together, the complete beam imaging scan program was restarted when operations resumed.

Five pairs (which are labeled as 'emit1–5') were 'emittance' scans, which are performed in the same manner as standard vdM scans but with a much shorter scan (a sequence of 9 steps with 10 seconds per step, and a maximal separation of approximately $\pm 3\sigma_b$). The emittance scans are not used for the final calibration. However, they are taken to compare with the emittance scans performed throughout the year as described in Section 6.2 and to evaluate the difference in results from emittance scans and those from the full scan. Four pairs (which are labeled as 'norm1–4') were standard vdM scans, in which the two beams are separated by up to $6\sigma_b \approx 600\ \mu m$ and scanned across one another in a sequence of 25 steps with 30 seconds per step. Scan pair 'norm3' immediately followed by 'norm2' to measure reproducibility effects, while 'norm4' occurred later in the fill to look for changes throughout the fill. Three pairs (which are labeled as 'imag1–3') were 'beam imaging' scans, in which one beam[11] is kept fixed at its nominal position while the other is separated and scanned in 19 steps from $+4.5\sigma_b$ to $-4.5\sigma_b$ with 46 seconds per step. Two scan pairs (which are labeled as 'off1–2') were 'offset' scans, with the same procedure as the standard scans except that the beams are separated by $\pm 1.5\sigma_b$ in the non-scanning direction.

[11]Beam 1 for scans 'imag1' and 'imag2' and beam 2 for scan 'imag3'.

Two length-scale calibration scans (LSC) were performed between scan pairs 'norm3' and 'norm4'. The 2018 length-scale calibration program consisted of two parts: the first ('lsc1') was the constant separation or 'hobbit' scan that is generally used for the CMS length scale calibration, in which the two beams are separated by $1.4\sigma_b$ (approximately equal to 1Σ) and moved together in steps of $1\sigma_b$ across and back, for a total of 11 steps with 70 seconds per step, once in each transverse direction. The second part ('lsc2') consisted of a 'variable separation' (also known as ATLAS-style) scan, in which one beam (starting with beam 1) is moved to $-2.5\sigma_b$, and then a three-point scan is performed with the other beam (starting with beam 2) at a relative position of $-1.25\sigma_b$, 0, and $+1.25\sigma_b$. The position of the first beam is then stepped in five steps to $+2.5\sigma_b$, repeating the three-point scan at each step. Therefore, the LSC consists of four individual scans, with two directions for each of the two beams, and each scan point has a duration of 46 seconds.

In each scan pair, the scan is performed first in the x-direction and then in the y-direction, with the exception of the variable separation length scale scan ('lsc2'), which was performed with the y scan first. The complete 2018 vdM scan program is shown in Figure 6.3 with the scan names labeled to correspond to the names given above.

The beam imaging and offset scans are intended for specific studies on the beam shapes described in Section 7.6, but they can also be analyzed as traditional vdM scans [24].

Figure 6.4 shows the beam positions for the two beams in the x and y-directions as measured by the DOROS BPMs during the scan program, showing (from left to right) in the top row the scans before the smoke alarm, consisting of two emittance scan pairs, a normal scan pair, an offset scan pair, and the two beam imaging scan pairs (interrupted in the last pair), and then in the next two rows, the resumption of the scan program, consisting of an emittance scan, the two beam imaging scan pairs, an offset scan pair, two regular scan pairs, the two LSC scan pairs, one regular scan pair, and two emittance scans at the end with different total separation.

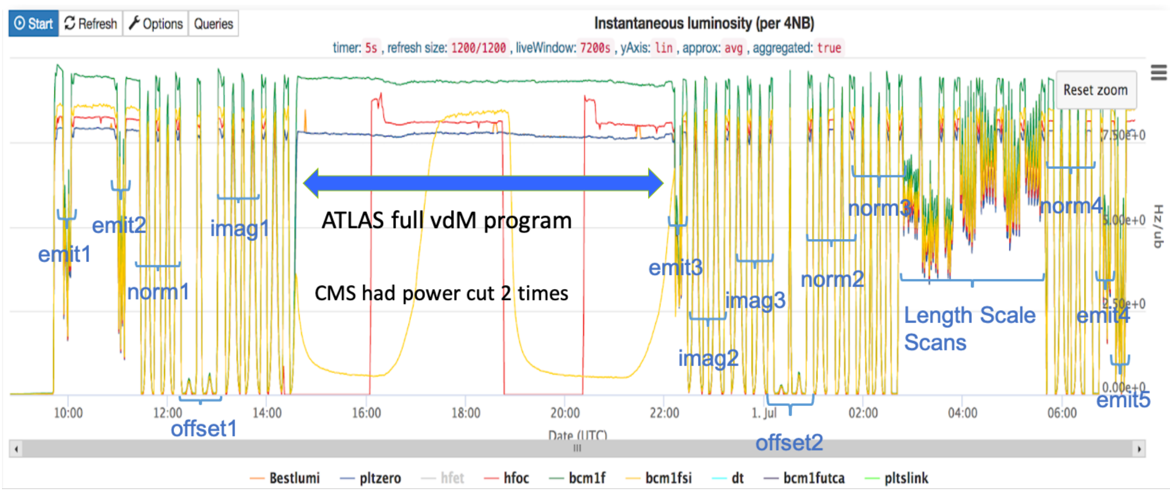

Figure 6.3: The full 2018 vdM scan program of LHC.

6.2. Emittance Scans

Although the vdM program is the most effective method for measuring detector characteristics, it is only performed once a year. Therefore, an additional method for monitoring the detector stability throughout the year is needed. For this, the so-called 'emittance scans' are employed since 2017 as they are performed for almost every LHC fill [25]. Emittance scans are performed mainly at the beginning of the LHC fills as 'early' emittance scans. However, for the long fills (10–12 hours), the luminosity can drop by almost a factor of two during the fill. Therefore, an additional 'late' emittance scan is also performed at the end of these long fills. Having two scans in the same fill allows monitoring the linearity of the detectors. In 2018, emittance scans were included nine steps for each step to collect data for 10 seconds.

The left of Figure 6.5 shows μ values of the HFOC during the emittance scan of fill 6592. The sudden drop of the rate observed before the emittance scan steps begin is beam optimizations performed to find the head-on collision point for the beams. Such optimizations are part of the standard procedure to improve the quality of the emittance scans. The middle and the right plots of Figure 6.5 show the normalized μ values as a function of beam separation fitted by a single Gaussian model for the same fill 6592 for HFOC.

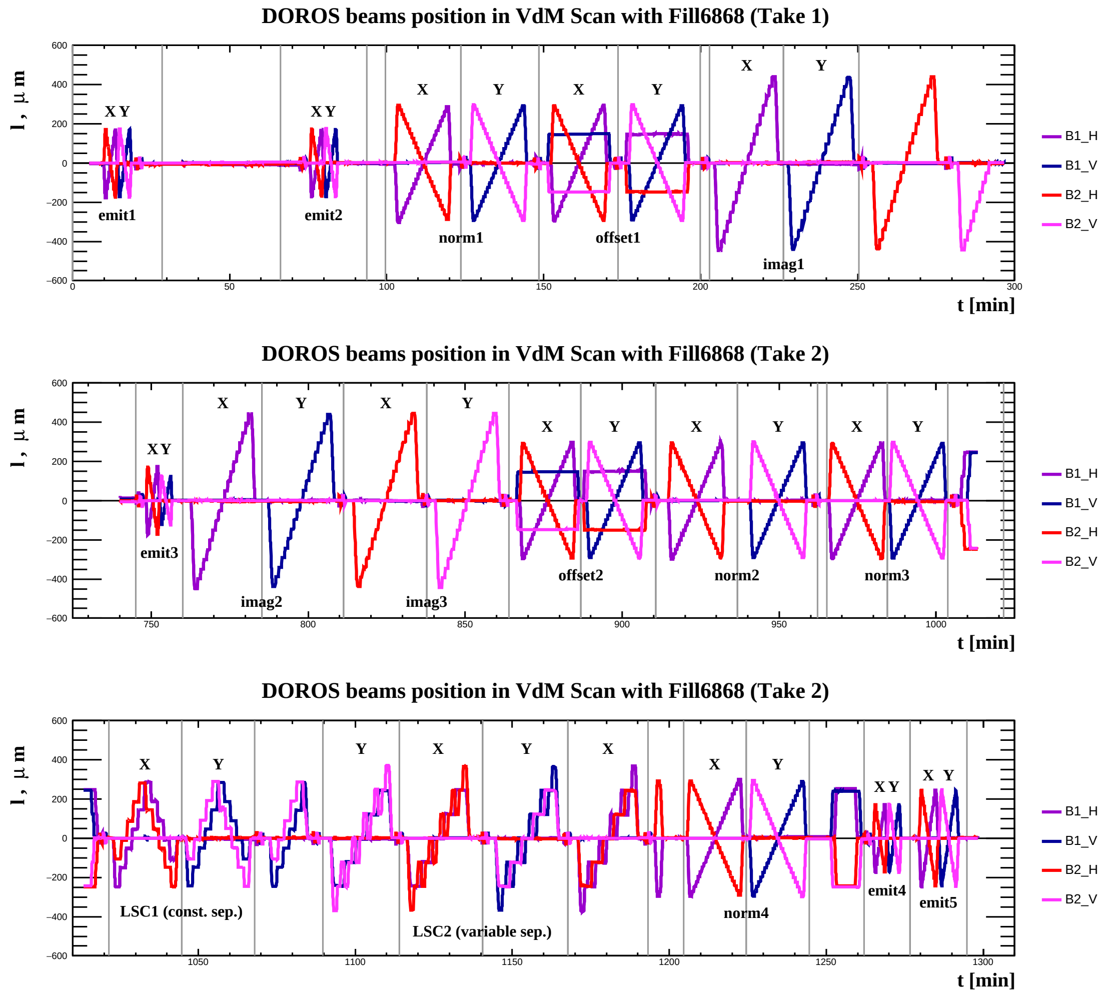

Figure 6.4: Relative change in beam positions measured by the DOROS BPMs during the 2018 vdM program for the two individual beams in the horizontal x and vertical y-directions, as a function of time. The top row shows the portion of the scan program before the alarm at CMS, while the bottom two rows show the scan program after the alarm.

The peak rate $R_{x,y}$ and the effective beam overlap $\Sigma_{x,y}$ for x and y-directions separately are collected from the fits to calculate the visible cross section σ_{vis} using the formula,

$$\sigma_{\text{vis}} = \pi \Sigma_x \Sigma_y (R_x + R_y). \tag{6.15}$$

The information for the stability of the detectors is gathered by the collection of σ_{vis} values throughout the year. Since σ_{vis} is a quantity characterising the detector,

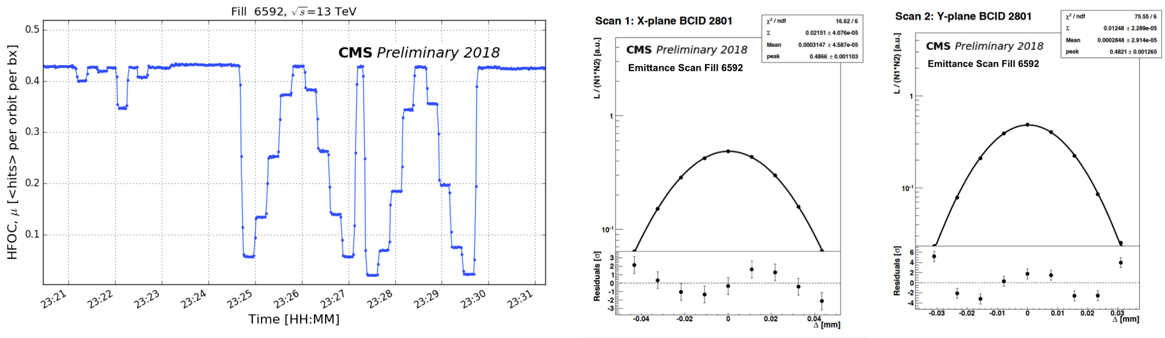

Figure 6.5: Rate (left) and normalized μ values (middle and right) of HFOC during fill 6592.

it is expected to stay constant for a stable detector configuration. Stability information is used to determine the performance changes of the detectors and the derivation of the efficiency corrections accordingly. In addition, corrections applying to σ_{vis}, as they are discussed in Chapter 7, also need to be applied on all σ_{vis} values collected.

In the past, measuring the linearity (or rather non-linearity) of a detector was only possible by comparing the ratios of reported luminosity values for all detectors, as described in Section 9.2.1. However, the utilization of the early and the late emittance scans allows the extraction of the linearity correction for a detector directly by measuring σ_{vis} values for each bunch in both scans for the coverage of a wide range of Single Bunch Instantaneous Luminosity (SBIL).

7. CORRECTIONS AND SYSTEMATIC UNCERTAINTIES

There are several systematic effects which affect the beam overlap width measurement, and hence the σ_{vis} extracted from the vdM scan procedure. These effects are measured and where applicable, corrected as described in this chapter. A systematic uncertainty is also assigned to the resulting measured cross section for each source [26].

7.1. Background Correction

Background correction is performed by a simple subtraction of a constant term from each data point recorded per scanning step shown in Figure 6.2. In the past, the constant background term was acquired by fitting the data to a double Gaussian model with an additional constant term to determine the background value. In 2018, vdM scans included two special 'super separation' periods, each being 5 minutes long. During the super separation scans beams are separated by 6σ in x and 6σ in y in order to reduce the rate from collisions to a negligible level, thus the rate measured corresponds to machine induced radiation and detector noise. Constant term estimated by the super separation scans are used for PLT, BCM1F, and HFOC, whereas HFET and VTX considered to be background-free.

For PCC, from the initial analysis of the separation scans the background is estimated as the average number of clusters as $\langle \mathrm{ncluster} \rangle = 0.169 \pm 0.003$. The systematic uncertainty of this measurement is evaluated by examining the variation of the average number of clusters as a function of time using both super separation scans. As shown in Figure 7.1, the value of the uncertainty is taken as the stability of the measurement over time and yields an uncertainty of $\sigma_{syst} = 0.010$. Thus, the total background value of PCC becomes,

$$\langle \mathrm{n_{cluster}} \rangle = 0.169 \pm 0.003(\mathrm{stat}) \pm 0.010(\mathrm{syst}) = 0.169 \pm 0.011\,(\mathrm{tot}). \tag{7.1}$$

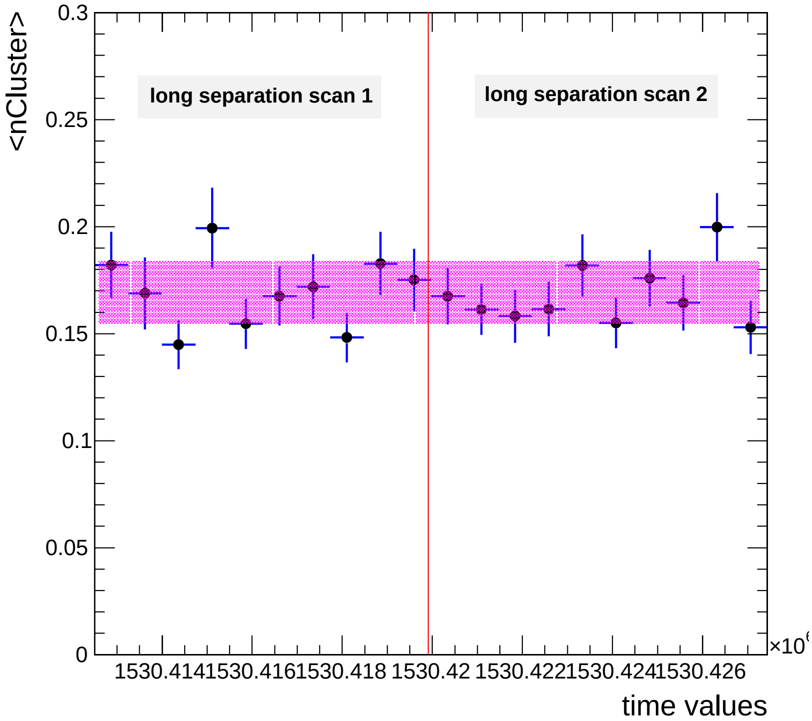

Figure 7.1: The average number of clusters $\langle n_{\mathrm{cluster}} \rangle$ as a function of time for both super separation scans. The systematic uncertainty is shown as the overlaid purple band.

The final fixed background values for BCM1F pCVD, PLT, HFOC and PCC are listed in Table 7.1. For all detectors, the ratio of the background to the peak value when beams are head-on is at the sub-percent level. A systematic uncertainty of 0.1% is assigned to the final calibration result to account for the uncertainty in the background subtraction.

An example of the background constant measured by the BCM1F detector accumulated during the two super separation periods is shown in Figure 7.2. The two measurements were separated by 4 hours in time and were performed to confirm that background level stays the same, and so the average constant term estimated from the super separation measurements is the same for all scans.

Table 7.1: Summary of measured background level for colliding bunches for detectors BCM1F pCVD, HFOC, PLT and PCC.

Detector	Count rate (μ) in super separation	μ in normal scan at head-on	Ratio [%] $\mu_{\text{super-sep.}}/\mu_{\text{head-on}}$
BCM1F pCVD	$(5 \pm 1) \times 10^{-6}$	$(956 \pm 44) \times 10^{-6}$	0.5
PLT	$(3 \pm 1) \times 10^{-6}$	$(1200 \pm 49) \times 10^{-6}$	0.3
HFOC	$(30 \pm 3) \times 10^{-6}$	$(3780 \pm 88) \times 10^{-6}$	0.8
HFET	0	$(11700 \pm 150) \times 10^{-6}$	0
PCC	0.17 ± 0.01	43.51 ± 0.49	0.4

The points on the plot fall into three horizontal bands as the highest band corresponds to colliding bunches, whereas the middle band at about half the height contains non-colliding bunches in which only one beam is filled, so the beam-induced background should be only half. The count rate in empty bunches shown as the bottom band corresponds to the detector noise.

7.2. Beam-beam Correction

In the same charge particle collisions (i.e. proton-proton and heavy-ion) beam bunches apply electromagnetic force towards one to another. These forces create two kinds of effects. First is the beam-beam effect, which is the effect created on shift of the orbital position of one bunch due to the electric field created by the other bunch. This effect results in deviation in orbital positions of measured collision, which changes the luminosity measurements and need to be corrected.

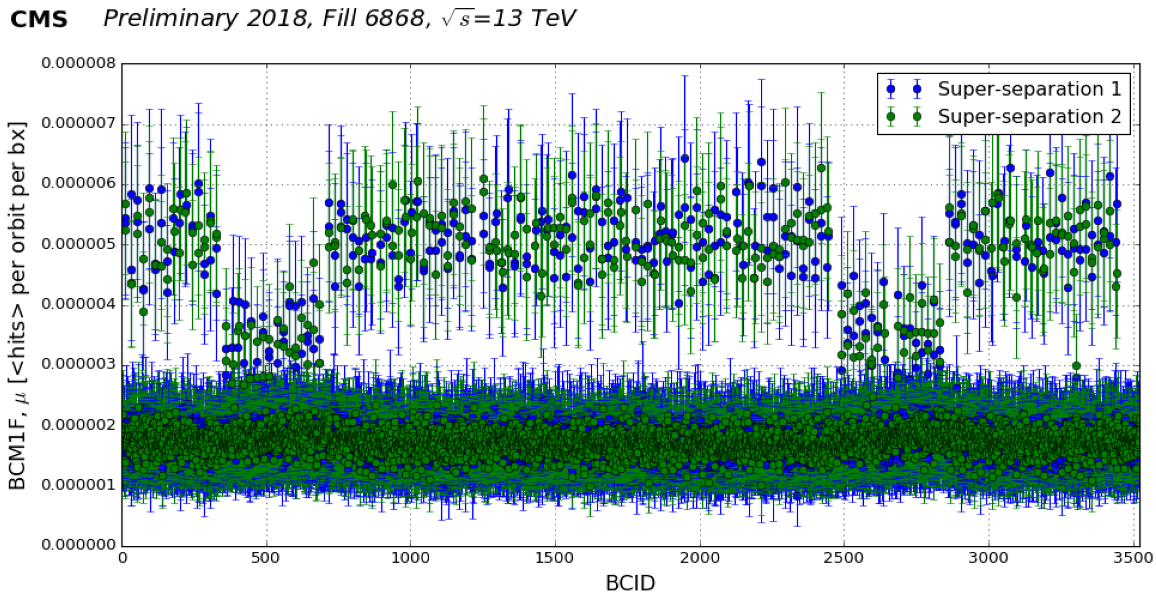

Figure 7.2: Background measured in the two super separation periods (blue and green dots) by the BCM1F detector. The colliding and non-colliding bunches show distinguishable levels of beam-induced background. The measured count rate in empty bunches corresponds to the detector noise.

The calculation and the final result of beam-beam effect is shown below. The calculated value of this correction is later applied on beam separation value measured by LHC.

The transverse charge density function is given below has Gaussian distribution factor in it as beams are accepted as having Gaussian shape.

$$\rho(x,y) = \frac{\lambda}{2\pi\sigma_x\sigma_y} e^{-(\frac{x^2}{2\sigma_x^2}+\frac{y^2}{2\sigma_y^2})}. \tag{7.2}$$

Then, the electric field created by the opposite beam on the probe beam derived by Bassetti and Erskine in [27] is as,

$$E_x(x,y) = \frac{\lambda}{2\epsilon_0\sqrt{2\pi \mid (\sigma_x^2-\sigma_y^2) \mid}} Im\left[W(\frac{x+iy}{\sqrt{2(\sigma_x^2-\sigma_y^2)}}) - e^{[-\frac{x^2}{2\sigma_x^2}+\frac{y^2}{2\sigma_y^2}]} W(\frac{x\frac{\sigma_y}{\sigma_x}+iy\frac{\sigma_x}{\sigma_y}}{\sqrt{2\mid(\sigma_x^2-\sigma_y^2)\mid}})\right], \tag{7.3}$$

$$E_y(x,y) = \frac{\lambda}{2\epsilon_0\sqrt{2\pi \mid (\sigma_x^2 - \sigma_y^2) \mid}} Re\left[W(\frac{x+iy}{\sqrt{2(\sigma_x^2-\sigma_y^2)}}) - e^{[-\frac{x^2}{2\sigma_x^2}+\frac{y^2}{2\sigma_y^2}]} W(\frac{x\frac{\sigma_y}{\sigma_x} + iy\frac{\sigma_x}{\sigma_y}}{\sqrt{2 \mid (\sigma_x^2-\sigma_y^2) \mid}})\right] \tag{7.4}$$

where σ_x and σ_y are beam widths in x, y axes calculated by the framework using the formula of,

$$\sigma_x = \sqrt{\frac{\Sigma_x^2 - 2\sigma_z^2 sin^2(\alpha/2)}{2cos^2(\alpha/2)}}, \qquad \sigma_y = \frac{\Sigma_y}{\sqrt{2}}. \tag{7.5}$$

Furthermore, $W(z)$ is the complex error function defined in [27] as,

$$W(z) = e^{-z^2}\left[1 + \frac{2i}{\sqrt{\pi}}\int_0^z e^{\zeta^2} d\zeta\right] \tag{7.6}$$

where

$$\zeta = \frac{x}{\sqrt{2(\sigma_x^2-\sigma_y^2)}} t + i\frac{\frac{y}{\sqrt{2(\sigma_x^2-\sigma_y^2)}}}{t} \quad and \quad \frac{\sigma_y}{\sigma_x} \leq t \leq 1. \tag{7.7}$$

The deflection angles derived and defined in [28] and [29] as,

$$\begin{aligned} \theta_x &= \frac{2r_p}{\gamma} N_p E_x(x,y), \\ \theta_y &= \frac{2r_p}{\gamma} N_p E_y(x,y) \end{aligned} \tag{7.8}$$

where r_p is the classical radius of a proton (taken as $1.53x10^{-18}[m]$), N_p is the intensity of the opposite bunch in the number of protons per bunch, and γ is the relativistic factor of a proton.

The orbital deflections (orbital shifts) are defined as,

$$\begin{aligned} \Delta u_x &=< \theta_x > \beta^*(\frac{1}{2tan(\pi Q_x)}), \\ \Delta u_y &=< \theta_y > \beta^*(\frac{1}{2tan(\pi Q_y)}) \end{aligned} \tag{7.9}$$

where β^* is the β function at interaction point of the bunches that is special to the CMS detector and Q_x, Q_y are the LHC tunes for x and y planes as $Q_x = 64.31$ and $Q_y = 59.32$.

In considering a probe bunch in the field of the opposite bunch, the probe bunch consists of protons distributed in space. The fields, described in Equations 7.3 and 7.4, are generated by the opposite bunch and depends on the distance from the center of that bunch. The distance is described by x and y in Equations 7.3 and 7.4. As protons of the probe bunch are distributed in space, the distance (x,y) from the center of the opposite bunch differs for protons of the probe bunch. Therefore, every proton in the probe bunch is experiencing different deflecting forces and gain their own deflection angle θ. Hence, an average deflection angle of overall protons of the probe bunch is taken and used in Equation 7.9.

Theoretically, such averaging must take into account the distribution of protons in the probe bunch and mathematically this averaging is a convolution integral over the deflection angle for every proton (that is, the function of (x,y)) multiplied with the density of protons in the probe bunch. The result depends on beam separation (the distance between centers of the probe and opposite bunches). However, for simplicity, the deflection angle calculated for the particle in the center of the probe beam instead of 'rigid integral'[12] is used. In this case, one obtains expressions Equation 7.8 instead of the integral. Thus, with the new approach electric fields given by the Equations 7.3 and 7.4 depend on beam separation[13] rather than (x,y) of individual protons.

The x and y values in the Equations 7.3 and 7.4 are the positions of individual protons in the bunches. Theoretically, these values need to be calculated for each proton in an integral that goes over the whole bunch. However, in the calculations at the analysis framework, they are taken as the separation values in (x, y) which corresponds to the center of bunches in respective axes.

[12] All particles of the probe bunch considered to have the same deflection angle of the particle in the center of the probe bunch.

[13] Δ_x and Δ_y are the distance between centers of colliding bunches in x and y axes.

Two assumptions that are made for making the electric field calculations applicable in the framework are as following:

(i) Equation 7.2 assumes bunches as infinite cylinders, whereas in the framework they are taken as finite cylinders with the length of L.

(ii) The change of the electric field due to taking the bunches as a finite cylinder is ignored.

Therefore, the definition of λ in Equations 7.2 , 7.3 and 7.4 becomes,

$$\lambda = \frac{ZN}{L} \tag{7.10}$$

where Z is the charge of the particle of the opposite bunch, and N is the number of particles of the opposite bunch.

Four orbital deflections for each beam (beam1, beam2) and both (x, y) axes are calculated. By adding beam1 and beam2 values for each respective axis one get two final state beam-beam corrections for (x,y) for each bunch numbers.

Later, the corrections are applied on beam separation values measured by LHC by simply adding them. The corrected values go into the fitting process of the framework described in Chapter 8 to get the new convoluted beam widths ($\Sigma_{x,y}$) and visible cross section values (σ_{vis}).

For the data of 2018 vdM measurement, beam-beam correction is calculated to be 1.5% with an uncertainty of 0.2%.

7.3. Dynamic-β^* Correction

The second effect created by having the same charged particles colliding is called dynamic-β^* effect. Dynamic-β^* correction is used for correcting the (de)focusing

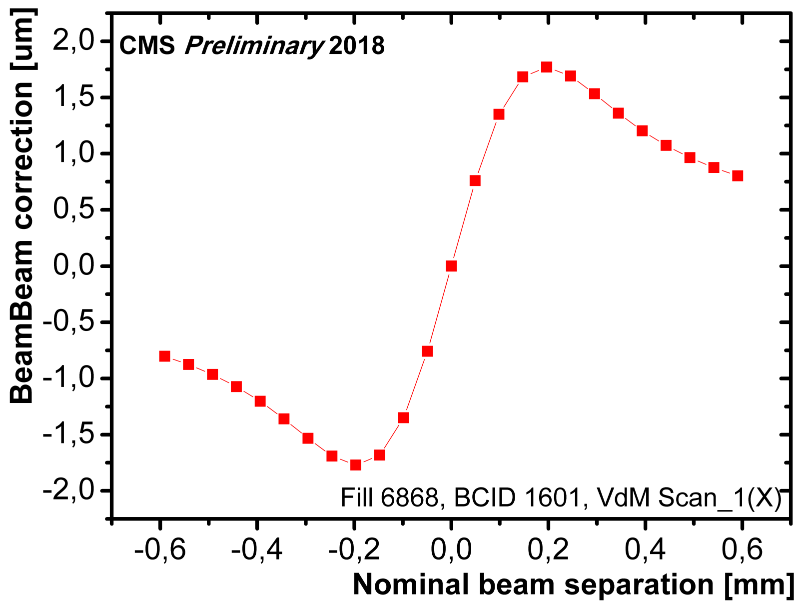

Figure 7.3: Beam-beam correction versus nominal beam separation is showed above. When the beams are head-on beam-beam correction becomes '0'. This plot contains data for fill 6868, for x-plane separation for the bunch ID 1601.

quadrupole effect of the probe bunch protons due to the electromagnetic fields created by the opposite bunch [30].

(De)focusing quadrupole effect of the beams affects the β parameter of the system which causes the change of the bunch size in transverse plane, thus changes the rate measured for the bunches. The correction calculates the β-parameter change for the interaction point (IP) of the beams and is applied on nominal rate measured for that particular interaction.

The β-parameter of the interaction point is calculated from,

$$\frac{\beta^*_{x0}}{\beta^*_x} = \sqrt{1 - (2\pi\varepsilon_x)^2 + 2(2\pi\varepsilon_x)cot(2\pi\theta_x)} \tag{7.11}$$

where β^*_{x0} is the 'unperturbed' β, θ_x is the 'unperturbed' horizontal tune and ε_x is the beam-beam parameter that is,

$$\varepsilon_x = \frac{\beta^*_{x0} N r_1}{2\pi\gamma\sigma_x(\sigma_x + \sigma_y)} \tag{7.12}$$

where γ is the relativistic factor of a proton as it was in beam-beam correction and σ_x, σ_y uses the same formalization as in Equation 7.5.

$$\frac{R_{corr}(\Delta_x)}{R(\Delta_x)} = \sqrt{\frac{\beta^*_x(\Delta_x)}{\beta^*_{x,ref}}}\sqrt{\frac{\beta^*_y(\Delta_y)}{\beta^*_{y,ref}}} exp\left[-\frac{1}{2}\left(\frac{\Delta_x}{\Sigma_x}\right)^2\left(1 - \frac{\beta^*_{x,ref}}{\beta^*_x(\Delta_x)}\right)\right] \tag{7.13}$$

where $R_{corr}(\Delta_x)$ is the corrected rate and $R(\Delta_x)$ is the measured rate at the same beam separation point in x-plane. The beam separation values Δ_x and Δ_y are corrected values come from beam-beam corrected data. $\beta^*_{x,ref}$ and $\beta^*_{y,ref}$ are reference values of β^* which uses $\Delta_x = \Delta_y = 0$ in the current implementation.

For the data of 2018 vdM measurement, dynamic-β^* correction is calculated to be -0.5% with an uncertainty of 0.1%. The uncertainty in the β^* measurement is taken to be 15% [31]. Using the nature of the beam-beam and the dynamic-β^* corrections being in the opposite directions and anti-correlated, a common correction of 1.0% and a conservatively chosen common systematic uncertainty of 0.2% are assigned to the combination of the two corrections.

7.4. Orbit Drift Calibration

The orbit drift correction accounts for the potential movement of the LHC orbit during the vdM scans. The beam position is measured using two separate beam position monitor (BPM) systems called the DOROS and the arc BPMs.

Primary measurement was gathered from DOROS, whereas the arc BPM was used as a cross-check. DOROS measures an incoming and an outgoing position in x and y for each beam.

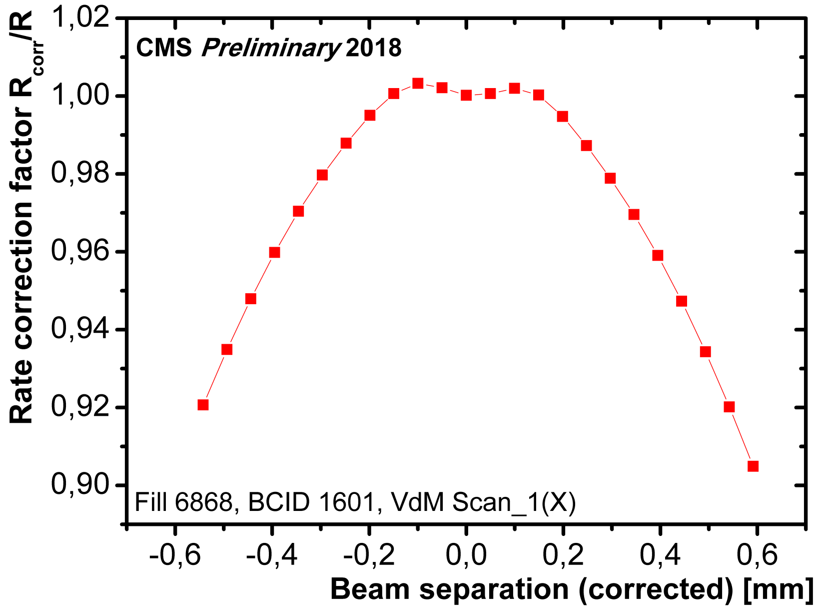

Figure 7.4: Dynamic-β^* correction versus beam separation that are corrected by the beam-beam correction is above. For head-on collisions dynamic-β^* correction becomes '1' meaning no correction on the measured rate. As the separation gets bigger the ratio of corrected and measured rates gets smaller, thus the correction effect gets bigger.

As there are no magnets between the DOROS BPMs and the IP, any beam movement is considered as a drift, and the position at the IP is taken as the middle point of the straight line between the left and right modules. Any offset measured at the moment 'Stable Beams' are declared is considered not a real offset, but rather a measurement bias which is then corrected for. Since the BPM data are not necessarily accurate when the beams are not head-on, the arc and DOROS BPM data are only used for periods before and after the scan and at the head-on step of the scans.

The final beam position measurements for the CMS vdM program using the DOROS BPMs are shown in Figure 6.4. The beam 1 horizontal and vertical positions are shown in violet and dark blue, and the beam 2 horizontal and vertical positions are shown in red and pink, respectively. A clear movement of each beam during each vdM scan pair can be observed, e.g., the beam imaging scans, where only one beam is moving, and the offset scans, where the separation in the non-scanning direction is at a 150 μm offset position rather than 0.

A slight orbit drift of the beams away from their nominal position is observed using the beam position data from directly before the scan, during the head-on step of the scan, and immediately after the scan. A linear fit from the start point to the head-on point of the scan is used to obtain an orbit drift correction for the first half of the scan, and similarly, a linear fit from the head-on point to the last point of the scan is used to correct the second half of the scan. The resulting data and fits are shown in Figure 7.5.

The orbit drift effect in 2018 vdM scans was observed to be typically less than 10 μm for the horizontal drift and less than 5 μm for the vertical drift. It is also observed from the arc BPM data that the assumption of the orbit drift accumulating linearly is reasonable.

A correction to the beam position is derived by dividing the measured orbit drift between the beginning and middle of the scan equally and correspondingly between the middle and the end of the scan. This correction assumes that the orbit drift accumulates linearly and may not account for fast orbit drifts. However, it is demonstrated on the measured visible cross sections of all vdM scans that scan-to-scan variation is significantly reduced with orbit drift correction applied, as shown in Figure 7.6 for BCM1F and HFET. As indicated in the text boxes on the plots, the standard deviation for BCM1F was improved by a factor of 2 and for HFET by more than a factor of 3. The red line on the plots indicates the average visible cross section for all seven scans.

The overall orbit drift correction applied using DOROS or arc BPMs has an overall correction of 0.2% on σ_{vis} and an agreement of 0.01%.

In addition to orbit drift, the peak position is also added in 2018 as a correction for the offset in the non-scanning direction. The peak position effect is more important in emittance scans than vdM scans since vdm scans uses single bunches (only 124

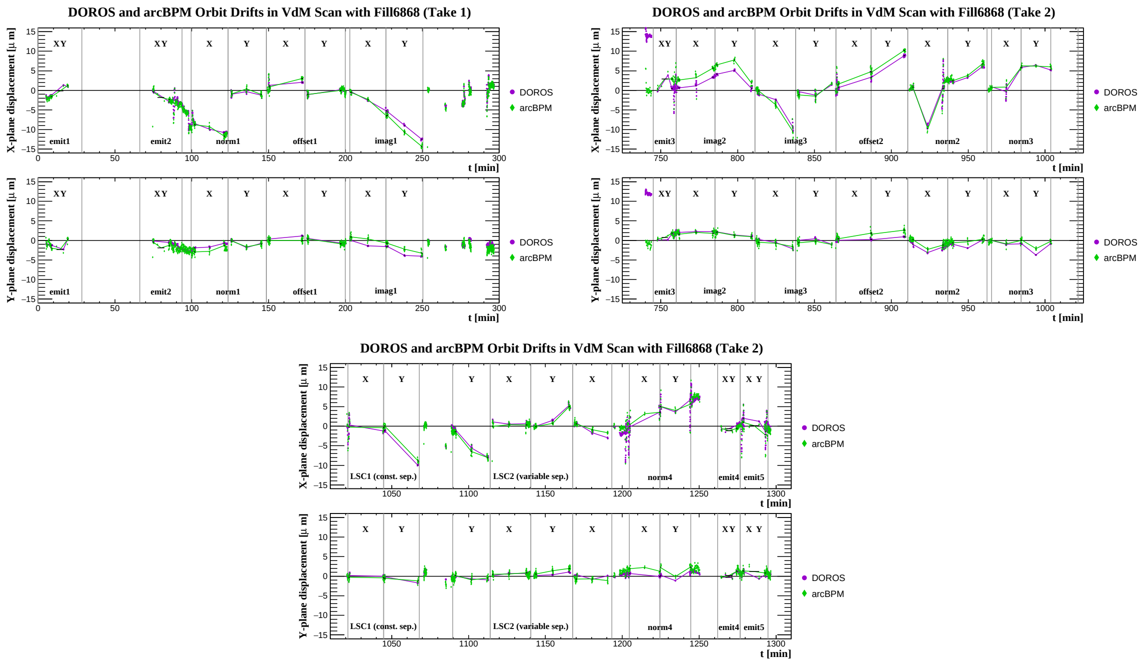

Figure 7.5: Results of the orbit drift measurement. The top left pair of the plots covers the time range before the alarm at CMS, the top right pair covers the first part of the time after the alarm, and the bottom pair covers the last part of the scan. In each pair the x drift is shown in the top plot and the y in the bottom plot. The dots represent the beam position measured at the times when the beams are head-on before, during, and after each scan, as given by the DOROS and arc BPMs in μm. The lines are the fits used to provide the orbit drift correction for each step of the scan.

bunches are filled out of 2808), yet still small offsets are observed in vdM scans and corrected. A total of 0.1% uncertainty is assigned conservatively for the orbit drift and peak position corrections.

7.5. Length Scale Cablibration

The length scale correction (LSC) stems from the fact that the nominal beam separation, as determined by the magnets used to steer the LHC beam, may differ from the actual beam separation. In order to measure this effect, a dedicated length scale calibration consisting of two separate scans are conducted.

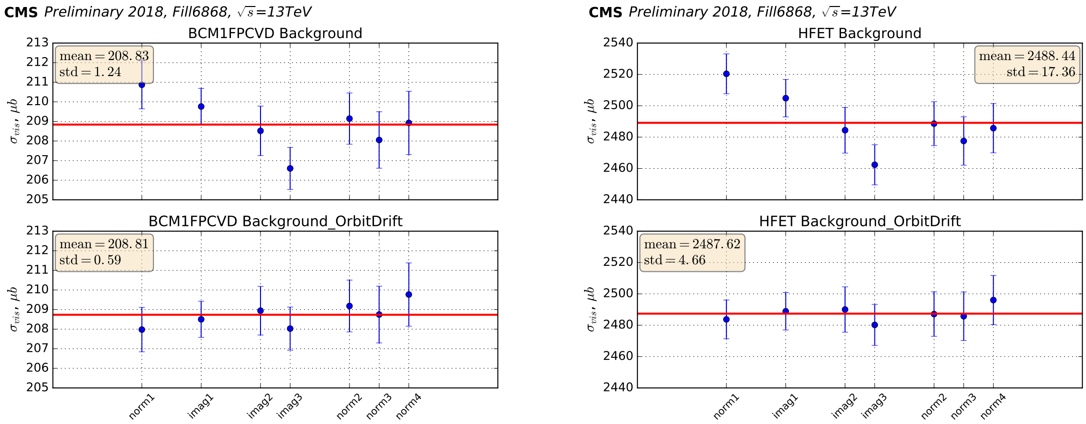

Figure 7.6: Measured visible cross sections for all vdM scans before (top) and after (bottom) the orbit drift correction is applied. Left: BCM1F, right: HFET. Significant improvement in the scan-to-scan agreement is observed.

7.5.1. Constant separation scan

In the constant separation scan, the beams are moved together, and the resulting beam spot position, as reconstructed by the CMS tracker, is measured. The beam is moved first in the positive direction and then in the negative direction in both the vertical and horizontal planes. Data are taken at five different beam positions for each direction with a sub-micron level accuracy. The procedure to derive the length scale calibration constant follows [24, 32]. The reconstructed beam spot position is plotted as a function of the nominal offset of the beam centroid and then is fitted with a linear function to extract a calibration constant.

Figure 7.7 shows the resulting fits as the difference between the reconstructed vertex position and the nominal beam position, so the resulting slope can be directly translated to the correction value. The fits produce slopes of on average 0.9934 ± 0.0003 in the horizontal scans and 0.9975 ± 0.0003 in the vertical scans. Application of the correction directly to beam-beam separations in the scan curves reduces the measured beam width by 0.66% horizontally and 0.25% vertically. The measured visible cross section is therefore reduced by 0.91% with the correction.

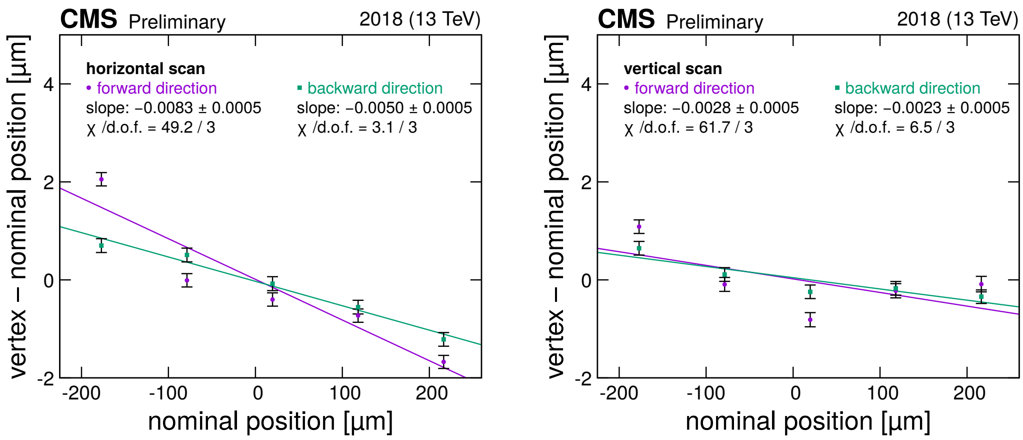

Figure 7.7: Difference between reconstructed beam spot position and nominal beam separation, as a function of the nominal beam separation, in the LSC constant separation scans. Left: scan in the x plane, for the forward (purple) and backward (green) scan directions. Right: same for the y plane. The plots are fitted with a straight line to derive the LSC correction.

There are four sources of systematic error that contribute to the length scale correction uncertainty. The first is the variation between the forward and backward scans, which amounts to 0.17% in the x scan and 0.03% in the y scan. The second is the effect of orbit drift. However, since the assumption of the orbit drift occurs linearly over time in the scan, the effect of the orbit drift will have an exactly opposite effect on the slopes in the forward and backward directions of the scan and hence the effect is canceled out on average. Instead, the uncertainty due to orbit drift is measured by first taking the forward-backward difference with the uncorrected beam positions, and then the fits reperformed with the beam positions corrected for orbit drift. The total resulting difference is 0.25% in the x and 0.13% in the y scans, of which 0.17% and 0.03%, respectively, are already accounted by the forward-backward difference, so the remaining 0.18% and 0.13%, respectively, is taken as the contribution from the orbit drift uncertainty. The third is a potential contribution from the effect of tracker misalignment, which is evaluated by comparing the reconstructed prompt data with the re-reconstructed data for the uncertainty of 0.03% in the x and 0.01% the y scans. Finally, at each point, the distribution of the individual vertex positions are fitted with a Gaussian to obtain a mean value; this is compared with the simple average to assess uncertainty in the fit method, which is negligible in the x scan and amounts to 0.17% for the y scan. The total correction and its uncertainty is thus $(0.66 \pm 0.26)\%$ for the x scan and $(0.25 \pm 0.22)\%$ for the y scan, resulting to a final correction of $(0.91 \pm 0.34)\%$.

7.5.2. Variable separation scan

The variable-separation scans provide a second measurement of the length scale. In these scans, one beam is scanned in five steps over the range $\pm 2.5\sigma$, and at each step, the other beam is scanned in three steps across it, keeping (at each scan step) the beams well centered on each other in the scanning plane. The actual displacement of the luminous region can then be measured with high accuracy using the primary vertex position reconstructed by the CMS tracking detector. Since each of the four bump amplitudes (two beams in two transverse directions) depends on different magnet and lattice functions, the length scale calibration scans are performed to extract each of these four calibration constants independently. The calibration data for both horizontal and vertical bumps of beam 1 and beam 2 are presented in Figure 7.8; as in the constant separation plots, the difference between the reconstructed beam position and nominal beam position is shown. Since normal vdM scans are performed by displacing the two beams symmetrically in opposite directions, the final correction value is given by the average of the corrections for beam 1 and beam 2 in each direction; i.e., $(-0.0027 - 0.0072)/2 \approx -0.49\%$ and $(-0.0004 - 0.0015)/2 \approx -0.10\%$ in the x and y directions, respectively. The results agree with those from the constant separation scan within uncertainties.

In order to assess the potential systematic effect due to orbit drift, the analysis is performed twice, once with the expected beam positions corrected for the orbit drift and once without the correction. Table 7.2 shows the overall results, both with and without the orbit drift corrections applied. The overall correction value taken from the results without the orbit drift correction applied is -0.59%. The systematic uncertainty is taken from the difference between the results with and without the orbit drift correction and is thus taken to be 0.05%. To account for the statistical uncertainties, the statistical uncertainty from the fits by $\sqrt{\chi^2/\mathrm{n_{dof}}}$ are calculated to be 0.07% in the

x-direction and 0.18% in the y-direction for a total statistical uncertainty of 0.25%. Adding the uncertainties together yields a total of 0.26%. The final uncertainty in the length scale calibration is evaluated by combining the results from the two independent scan methods. The two scan results are averaged to get the final correction and its uncertainty of $(-0.75 \pm 0.21)\%$.

Table 7.2: Length scale calibrations at the CMS IP using the variable separation procedure. Values shown are the ratio of the beam displacement measured by CMS using the average primary vertex position, to the nominal displacement entered into the accelerator control system. Ratios are shown for each individual beam in both planes, as well as for the beam separation scale that determines that of the beam overlap in the vdM scan. The statistical uncertainties are negligibly small.

Measured Scale	Without Orbit Drift Correction		With Orbit Drift Correction	
	Horizontal	Vertical	Horizontal	Vertical
Beam 1	0.9973	0.9996	0.9973	0.9996
Beam 2	0.9928	0.9985	0.9937	0.9987
Average	0.9951	0.9991	0.9955	0.9992

7.6. X-Y Correlation

The vdM scan method is derived assuming bunch proton densities that are factorizable in x and y, as shown in Equation 6.2. This is, however, not valid in general and may result in an overestimation of the beam overlap integral. In order to estimate the size of this bias, the bunch proton densities are reconstructed using measured vertex distributions with special beam imaging scans. The bunch proton densities can be used to derive corrections on the visible cross section measurement.

7.6.1. Beam Imaging Analysis

In the beam imaging scans one beam is held stationary while the other beam is scanned in one direction consists of 19 steps starting from -9σ to 9σ per σ steps. The

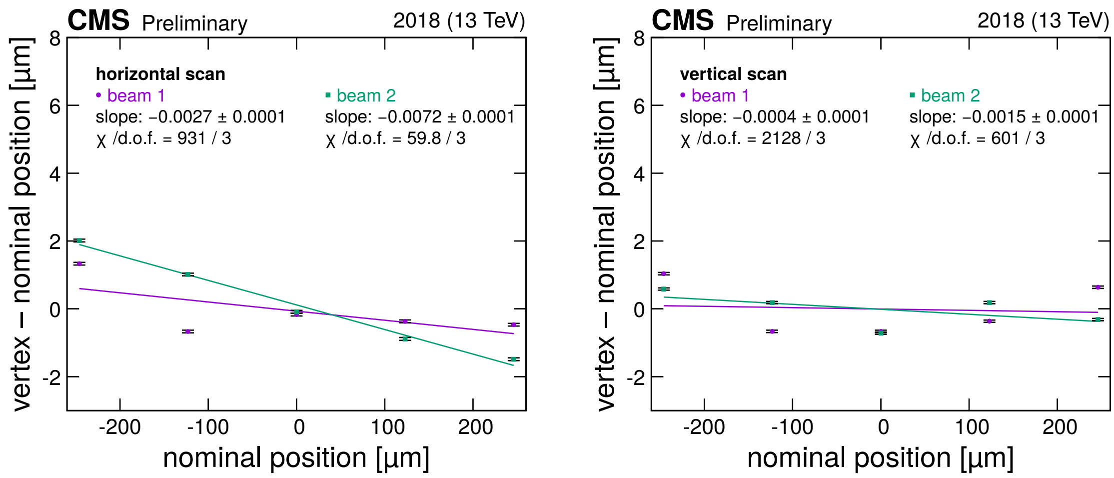

Figure 7.8: Length scale calibration scan, using the variable separation procedure, for the x (left) and y (right) direction of beam 1 (purple) and beam 2 (green), respectively. The difference between the reconstructed beam spot position and nominal beam separation, as a function of the nominal beam separation is shown. Orbit drift corrections are not applied in this plot. The line is a linear fit to the data. Errors are of statistical nature.

collected two-dimensional vertex distribution is then fitted by a beam shape model to obtain the bunch proton density of the stationary beam [33]. The simplest shape model for the bunch proton density that has a correlated spatial dependence is a Gaussian distribution with x-y correlations parametrized by a correlation parameter ϱ,

$$g(x,y) = \frac{1}{2\pi\sigma_x\sigma_y\sqrt{1-\varrho^2}} \exp\left(-\frac{1}{2(1-\varrho^2)}\left[\frac{x^2}{\sigma_x^2}+\frac{y^2}{\sigma_y^2}-\frac{2xy\varrho}{\sigma_x\sigma_y}\right]\right). \tag{7.14}$$

The fit model for the bunch proton density using Equation 7.14 is,

$$\rho(x,y) = -w_N g_N(x,y) + w_M g_M(x,y) + (1 + w_N - w_M) g_W(x,y) \tag{7.15}$$

where g_M is the main Gaussian component, following the form of Equation 7.14, w_M is a large weight, g_W is a wide component with a small weight to model wide tails, g_N is a narrow component with a small but negative coefficient of $-w_N$ to model a flattened central part.

The derivation of the x-y correlation correction needs the simulation of the vdM scans using the new bunch proton density from Equation 7.15. Comparison of the non-factorized and the factorized bunch proton densities used in the calculation of $\Sigma(x, y)$ showed that there are still significant residuals that are not considered by the fit model of Equation 7.15. The sources of these residuals are yet to be understood, hence the x-y correlation is not applied as a correction to the vdM scans, but rather assigned as a systematic uncertainty of 2.0% to cover the resulting uncertainties observed in the correction.

7.6.2. Offset Scan Analysis

As described in Section 6.1.2, the offset scans are specific scans intended for x-y correlation studies. The scans are conducted as the normal vdM scans with an offset of $\pm 1.5\sigma_b$ in the non-scanning direction.[14] Thus, the offset scans make it possible to perform a test for the x-y correlation of the overlapping shape directly without reconstructing the bunch proton densities. The study uses the assumption that the beam geometry does not change between the two scan pairs ('off1' and 'off2') that are performed. Thus, for the test, a 2D model on the vdM and offset data is fitted simultaneously.

7.7. Bunch Current Normalisation

While the beam widths $\Sigma_{x,y}$ are determined from fits to the beam shape, the currents of the two beams, evaluated in the BCID being analyzed, are an important input to the calibration procedure. The bunch current normalization is measured by the Fast Bunch Current Transformers (FBCTs) with a per-bunch-slot granularity (25 ns). The FBCT measurement is cross-calibrated to the total intensity of the beam current product measured by the Direct-Current Current Transformers (DCCTs). However, DCCT measurements include components which do not contribute to the total luminosity: 'satellite' charges, which refers to the charge in a single filled bunch slot but not in the colliding RF bucket (each 25 ns bunch slot contains ten 2.5 ns RF buckets,

[14] An offset in the x-direction for y-scan and vice versa.

of which only the first is nominally used for collisions), and 'ghost' charges, which are charges not in any nominally filled bunch slot. These satellite and ghost contributions must thus be corrected to obtain the correct bunch charges in Equation 6.11.

Table 7.3 shows the percentage of ghost-bunched charges for the two colliding beams as measured with the LDM. No particular time dependence for either beam is observed. The resulting overall spurious-charge correction is $0.13 + 0.15 \approx 0.3\%$ [34]. In addition, the observed amount of satellite charge ($\approx 0.09\%$) [34] is also included into the correction, for a total correction of 0.4%.

The two sources of systematic uncertainty arise from: first being the uncertainty in the absolute beam current, which comes from the precision of the DCCT measurement of the product of the beam currents of 0.2% [35], and the second is the uncertainty in the ghost charge measurement, which is obtained by comparing the beam-gas rates in beam-empty and empty-empty crossings at IP8 using the beam-gas imaging method [36]. Their difference of $\approx 0.05\%$ [37] is taken as the systematic uncertainty in the spurious charge correction.

Table 7.3: Percentage fraction of the ghost charges as measured separately from LDM devices and the LHCb Collaboration during fill 6868.

Input	beam 1 [%]	beam 2 [%]
LDM ("bunched")	0.13	0.15
LHCb	0.14	0.19

8. THE LUMINOSITY ANALYSIS FRAMEWORK

The luminosity analysis framework composes the heart of the luminosity calibration analyses. The framework was developed in 2015 as a centralized software package to analyse 'vdM scans' for the extraction of the calibration constants σ_{vis}. Nevertheless, the framework has been improved over the years to handle other scan types, e.g., 'emittance scans' and 'mu scans'.

The analysis framework is written in Python (version 2) language, and it utilizes CERN's data analysis package 'ROOT'[15] under the hood. The input data for the luminometers and the scan information are taken from BRIL DAQ through the Data Interchange Protocol (DIP).[16] The data are structured in tables for each detector and each scan in a 'HD5' format. In basic terms, the framework takes the input data, applies requested corrections onto the raw rates, fits the corrected data with the chosen function (e.g., single Gaussian, double Gaussian), and finally, from the fit results, calculates and publishes the $\Sigma_{x,y}$, $R_{x,y}$ and $\sigma_{\text{x,y}}$ in a 'CSV' file. During the run process, the vdM framework also creates and saves intermediary files for both the usage of its modules and informing the user about the outputs of each process.

The framework can be examined under two categories: the core and automation wrappers. The core contains the scripts responsible for the main processes needed to perform the luminosity analysis. The automation wrappers serve the user for the ease of usage of the framework. Sections 8.1 and 8.2 focus on the core and automation, respectively, and Section 8.3 discusses the improvements applied to the framework in 2018.

[15] An object-oriented framework created for handling the data analysis challenges of high-energy physics [38].

[16] A middle-ware infrastructure developed for the lightweight communications between control systems [39].

8.1. The Core

Figure 8.1 illustrates the core structure and the data flow of the luminosity analysis framework. The core framework has the driver script called 'vdmDriverII.py' responsible for the executions of the consecutive operations. The vdmDriver script uses a configuration file called 'vdmDriverConfig.json', which is formatted in 'JSON',[17] for the decisions of which scripts to run and which data to be processed. An example of this configuration file is included in Appendix B.1. The driver directly calls eight specialized scripts that produce both the intermediary files and the final result file and calls two plugin managers, indirectly, for the applications of corrections and fits.

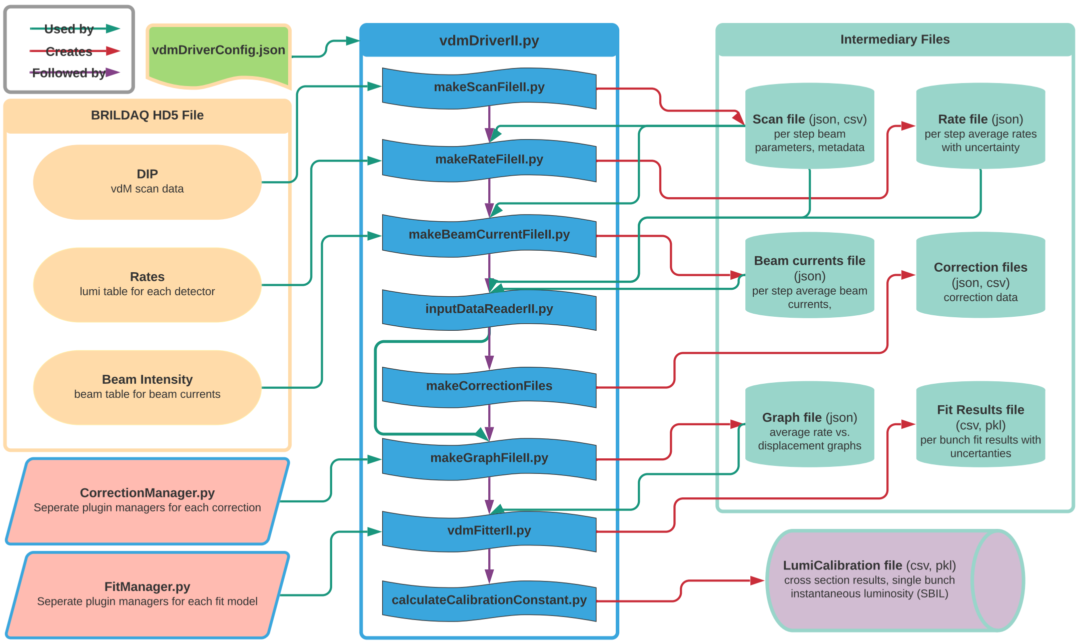

Figure 8.1: The flowchart of the core structure of the luminosity analysis framework.

8.1.1. Make Scan File

As the first step of the analysis, the vdmDriver calls for the 'makeScanFileII.py' for the production of the scan files. Then, according to the path given in the vdmDriverConfig file, the script imports DIP data from BRIL DAQ that contains start and end timestamps and the separation values of the beams for each step of the scan.

[17] A lightweight data-interchange format that eases for users to read and write [40].

The information, later saved in both 'CSV'[18] format for ease of the user and in 'JSON' for easy readability by the computer.

8.1.2. Make Rate File

The 'makeRateFileII.py' script makes the rate file for the specified luminometer by gathering the data from BRIL DAQ. The raw rates are integrated over 4 'luminibles' (NB4), where each nible corresponds to 2^{12} (4096) LHC orbits or 364 ms. The NB4 measurements are averaged for each step according to the timestamps stated in the scan file. The uncertainty of the averages is calculated as a binomial error. To be precise, the script uses the formula,

$$\sqrt{\frac{\overline{N}(1-\overline{N})}{4.4096.n}} \tag{8.1}$$

where $\overline{N}$ is the average rate of the nibles, and n is the number of nibles that are averaged. The results are saved into a 'JSON' file to be used later in the process chain.

8.1.3. Make Beam Current File

The beam intensity data are collected by the 'makeBeamCurrentFileII.py' from BRIL DAQ. The data are averaged per step according to the scan file for each bunch ID (BCID) and saved as a 'JSON' file.

8.1.4. Input Data Reader

The 'inputDataReaderII.py' serves as an intermediary script for collecting the data created by the framework until that point. The created scan, rate, and beam current files are imported and converted into objects to be used in the following steps.

[18] A comma-separated values (CSV) file is a delimited text file that uses a comma to separate values [41].

8.1.5. Make Correction File

The framework uses two scripts for the application of each correction. The first script collects the required data for that particular correction and calculates the amount of correction needed to be applied according to the procedures described in Chapter 7. Then, the output data is saved into 'CSV' and 'JSON' intermediary files.

The second script is responsible for applying the correction to the raw rates, which is managed by the 'CorrectionManager.py'.

8.1.6. Make Graph File

The 'makeGraphFileII.py' loads the objects created by the 'inputDataReaderII.py' as the input data. It accesses to all scan, rate, and beam current data previously calculated. Subsequently, it calls the 'CorrectionManager.py' script to gain access to the correction data and for the application of the corrections. The order of the application of the corrections is fixed by hardcoding in the framework. Previously, the order was 'Background' (BG), 'BeamBeam (BB)', 'LengthScale (LSC)', and 'Ghosts and Satellites (GS)'. However, the addition of 'DynamicBeta (DB)' and 'OrbitDrift (OD)' corrections in the framework have changed the order to BG, BB, DB, LSC, OD, GS. A further study on scan-to-scan variations with different combinations of the application order for the corrections showed that the application of the OD correction as early as the second in line minimized the scan-to-scan variations. Hence, the final order for the corrections has been made as BG, OD, BB, DB, LSC, and GS. The requested corrections by the user are always re-ordered according to this sequence independent of their requesting order.

After the application of the corrections, the rates are normalized by dividing them with the corresponding beam currents. The final results of the 'makeGraphFileII.py' are saved in a 'JSON' file that contains normalized average rate values for each beam separation per BCID.

8.1.7. VdM Fitter

The rate data that are corrected, averaged, and normalized by the 'makeGraphFileII.py' script are loaded into the 'vdmFitterII.py' for the fitting process. Next, the fitter script calls another plugin manager similar to the 'CorrectionManager.py' called 'FitManager.py' to apply the fit model chosen by the user. The most commonly used fit models are 'Single Gaussian (SG)' and 'Double Gaussian (DG)' functions created as 'TF1' objects under the roof of the 'ROOT' libraries.

The input graph data then fitted by the vdmFitter to produce the output files in both 'CSV' and 'PKL' formats, where the latter is inherited from the old version of the framework and not used in the current version. Additionally, upon the user's request, the framework can create and save a visualization of the data points, and the corresponding fits into a 'PDF' file for a visual inspection as shown in Figure 6.2.

8.1.8. Calculate Calibration Constant

Using the fit results saved by the vdmFitter, the 'calculateCalibrationConstant.py' script calculates the final results of the framework as beam width Σ and σ_{vis} values for x and y components by using the methodology given in Chapter 6. The results are saved in 'LumiCalibration' files in 'CSV' and 'PKL' formats, separately. An example result file for the PLT detector in fill 6868 using SG fit is presented as a table in Appendix B.3.

8.2. Automation

In older versions of the framework prior to 2017, the user had to enter the required information of the data path, the detectors to be processed, the corrections to be applied, and the fit to be performed by hand into the configuration file. This was possible since the need for usage for the framework was limited by the vdM program, which is performed once per year. However, with the addition of new luminometers and corrections into the framework, and most notably with the need for analyzing the 'emittance scans' through the year, automation became required. Hence, an additional layer of automation wrappers is added in 2017, where the user can select the options by giving option flags to the main script at the beginning.

The automation is done by adding four scripts to the framework beside the core, yet the user only needs to interact with one of them, the 'AutoAnalysis.py'.

8.2.1. Auto Analysis

The 'AutoAnalysis.py' constitutes the main interaction point between the user and the framework. The script can take a number of option flags for enabling and disabling different processing modes and a single 'HD5' file as input data. In some rare cases, the scan data can be saved in two separate files rather than one. In which case, both of the 'HD5' files needed to be given by using a flag. Additionally, the framework can be used in 'watcher mode', where it automatically checks for newly added 'HD5' files in a specified path for the analysis and posting of the results to the BRIL monitoring web page.

The script uses a configuration file in 'JSON' format called 'configAutoAnalysis.json' that specifies: the folder paths that the results needed to be saved, the minimum number of steps in a scan to decide whether a 'double Gaussian' fit to be used or not, the number of seconds to wait before re-checking the center folder for the 'HD5' files for the 'watcher mode', the maximum number of threads that the script is allowed to use for running in the computer, and the names of the luminometers as written in the 'HD5' files. An example of this configuration file is shown in Appendix B.2.

The complete list of the option flags and their actions are:

- '-f', '–filename' {hd5 file path}: Indicates the path to the 'HD5' file. (Not needed for the watcher mode.)
- '-f2', '–filename2' {hd5 file path}: Gives the path to the second 'HD5' file. (In case the scan has two files.)

- '-c', '–central' {folder path}: Gives the path to the central folder that contains the watcher input data. (In case it is different than the path indicated in the configuration file.)
- '-t', '–test': Analyses the data for only the detectors given in the configuration file under 'ratetables'.
- '-p', '–post': For posting one-time analysis to the web monitoring. (The watcher mode posts automatically.)
- '-pdf', '–pdfs': Makes pdf files for the visualization of the output of fitting.
- '-l', '–logs': Creates log files for the fitting process.
- '-d', '–double': Forces double Gaussian function to be used in fitting. (The default is a single Gaussian model.)
- '-ms', '–muscan': Removes the prerequisites for the scan data to obey for the analysis of 'mu scans'.
- '-bg', '–background': Applies Background correction using non-colliding bunch intensities.
- '-bgf', '–supersep': Applies Background correction with fixed values collected from 'superseparation' scans.
- '-b', '–beambeam': Applies BeamBeam correction.
- '-db', '–dynamicbeta': Applies Dynamic-Beta correction.
- '-od', '–orbitdrift': Applies OrbitDrift correction.
- '-ls', '–lscale': Applies LengthScale correction.

The AutoAnalysis is mainly responsible for the collection of the user inputs. The script runs the 'Configurator', 'runAnalysis, and 'postvdm' according to the options passed by the user. Additionally, it creates the output folders, if they do not already exist, and gives access rights to all files created for all users since the framework runs in a reserved cluster for BRIL operations.

8.2.2. Configurator

The configurator automates the metadata input to the vdmDriver configurator file. The 'Configurator.py' imports the DIP data from the target 'HD5' and selects the beginning and end of the scan to write into the template of the vdmDriver configuration file, an example configuration file is in Appendix B.1.

The selection process of the timestamps is done by a series of prerequisites and filtering to extract the information. The filters are made exclusively for vdM or vdM-like scans, e.g., emittance scans. However, in 2018, an option flag '-ms' is added to the framework to make it possible that other scan types, particularly mu-scans, can pass the filters and be processed by the framework.

8.2.3. Run Analysis

The 'runAnalysis.py' script is responsible for the running of the vdmDriver. It collects the metadata from the vdMDriver configuration file and accordingly runs the 'vdmDriverII.py' script. Additionally, it handles the errors and exceptions as well as the logging of the framework processes.

8.2.4. Post VdM

The 'postvdm.py' script collects the results from both LumiCalibration and FitResults files to extract $\Sigma_{x,y}$, $R(t)$, μ, σ_{vis}, and SBIL. It fits σ_{vis} values against SBIL with a linear function and saves the output together with the extracted values into a 'JSON' file. If the framework is running in the watcher mode or the option flag '-p' is given, the postvdm publishes these outputs to the BRIL web monitoring system.

8.3. Improvements in 2018

There have been number of improvements in the luminosity analysis framework in 2018. Most of them happened to be under the hood performance improvements. However, there are also some significant developments to the framework, which are:

- The Ramses detector is added as a new luminometer for stability and linearity cross-check of online luminometers.
- OrbitDrift and Dynamic-Beta effects are corrected in the vdM fitting rather than being an uncertainty as in previous years.
- Ghosts and satellites effect is added as a correction.
- A new correction approach for the background in the vdM scan is added using a dedicated ‘super-separation’ period.
- Peak position effect is added as a correction.

Additionally, different versions of the framework that are used by the specialized groups under BRIL are merged into one ‘master’ framework to ensure consistency and convenience across the groups.

9. ANALYSES RESULTS

As described in Chapter 6, the convoluted beam width and average peak rate are used to calculate the visible cross section σ_{vis}. The count rate is dependent on the individual detector and is determined by the acceptance of the detector, which is a function of the detector geometry and position with respect to the interaction point. On the other hand, the convoluted beam width $\Sigma_{x,y}$ is a beam property and should therefore be measured to be the same by all detectors. The comparison of the convoluted beam width and the evolution of its value over the course of the vdM fill are described in Section 9.1.

For a given set of beam conditions and detector performance, the visible cross section is constant. The visible cross sections measured by all detectors during the vdM fill are discussed in Section 9.2.

For the online luminometers, bunch width measurements are available for all 124 bunches, but for comparison of the results with PCC or clarity of the plots, in some cases only 5 bunches[19] are used.

9.1. Comparison of the Beam Widths

To illustrate the evolution of the beam width in the x and y-directions, the measured $\Sigma_{x,y}$ values are shown in Figure 9.1 over the whole duration of the vdM fill. All normalization corrections are applied to the $\Sigma_{x,y}$ measurements. The first three scans correspond to the first data taking period, and all other scans were taken in the second data taking period. As there was a gap of approximately 8 hours between the two data taking periods, a pronounced step in $\Sigma_{x,y}$ is observed when going from imaging scan 1 (imag1) to imaging scan 2 (imag2). It is relatively easy to see that bunches 265 and 865 belong to the group of bunches with high emittance and bunches 1780, 2192, and 3380 are in the group with lower emittance.

[19] The 5 bunches which have pixel data available.

All bunches follow a similar trend, and there is no difference observed in the behavior of the two different families of bunches.

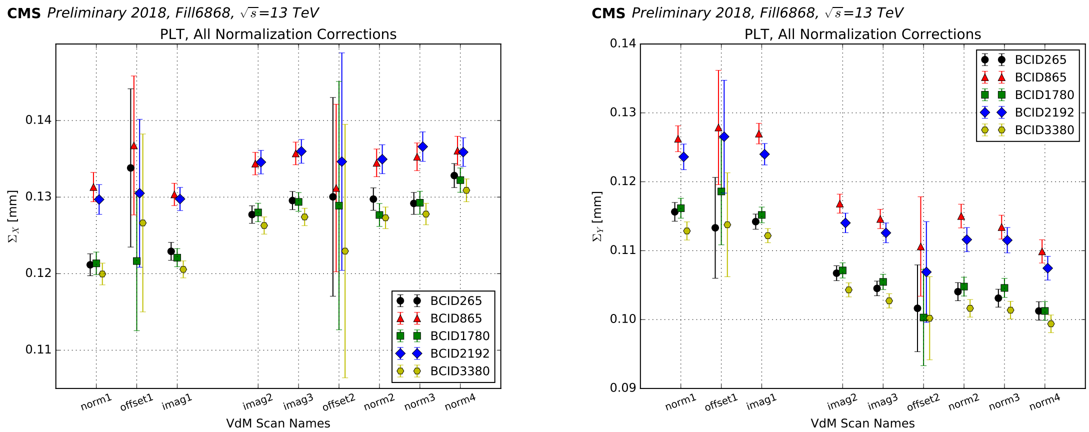

Figure 9.1: The convoluted beam width measured by PLT in the x (left) and y (right) dimension (Σ_x and Σ_y) after all normalization corrections have applied for the five bunch crossings with PCC data available. The uncertainty shown is statistical. The beam size increases in the x-direction and decreases in y-direction over time.

The offset scans have a significantly lower overall rate, so the statistical uncertainty in the measurement is correspondingly larger. As the offset scans are more sensitive to potential non-factorization (x-y correlation) effects, any significant difference of the beam width measured in the offset scans would suggest the presence of such an effect. The average beam width extracted from the first offset scan is slightly higher than that extracted from the centered scans norm1 and imag1 taken on either side of offset1 in x and y, as seen in Figure 9.1. However, the second offset scan (offset2) shows similar Σ_x and slightly lower Σ_y in all represented bunch crossings. This change could be interpreted as a change of the non-factorization during the fill, but it should be confirmed from other non-factorization measurements.

The two groups of bunches with different beam widths can be more clearly observed by looking at all bunches for the online luminometers, as shown in Figure 9.2-left. The cross check with Σ_x measured by PCC and by VTX in a normal vdM scan (norm3) is shown in Figure 9.2-right. This scan is chosen as a representative, well-behaved scan from the middle of the fill. Additional plots can be found in Appendix A.

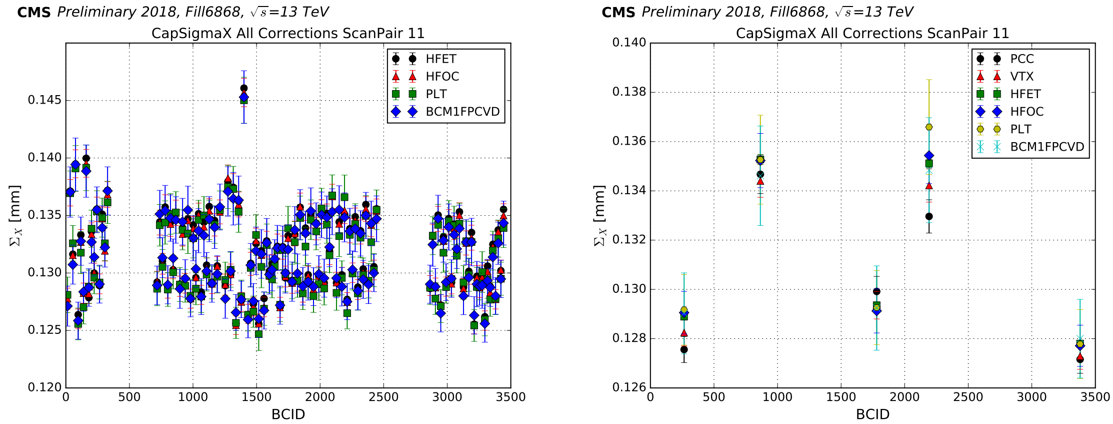

Figure 9.2: Convoluted beam width (Σ_x) measured in a normal vdM scan (norm3) for all colliding bunches for all online luminometers (HFET, HFOC, PLT, BCM1F) on the left and for the 5 bunch crossings available for PCC and VTX together with online detectors on the right. The measurements from all detectors agree within the statistical error bars.

The ratios of the $\Sigma_{x,y}$ measured by each online luminometer to $\Sigma_{x,y}$ measured by HFET are shown in Figure 9.3. The agreement is on the sub-percent level, as measured in the scan pair norm3. The largest disagreement is observed for HFOC in the scans of the first vdM period, with a disagreement up to a maximum of 0.5% (scans norm1, offset1 and imag1).

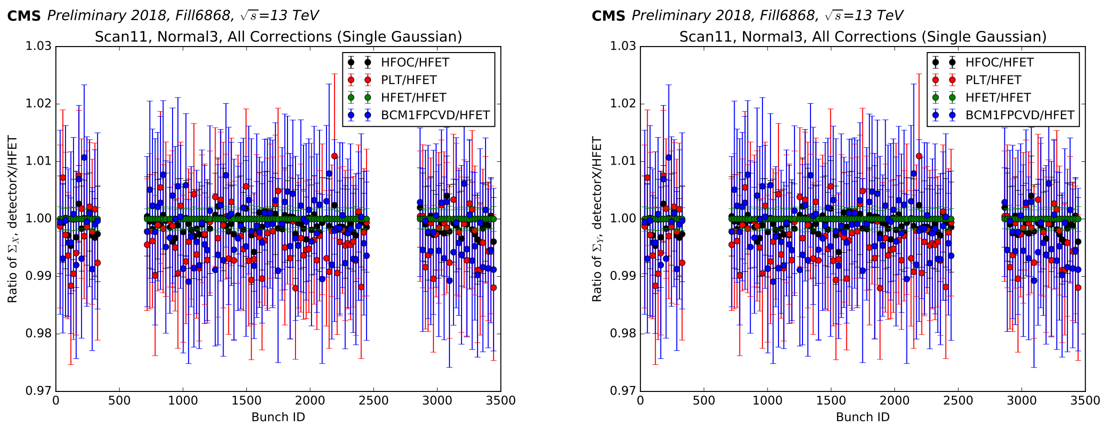

Figure 9.3: Ratio of Σ_x (left) and Σ_y (right) for each bunch crossing in a normal vdM scan pair (norm3) for each of the online luminometers (HFET, HFOC, PLT, BCM1F) to $\Sigma_{x,y}$ of HFET.

9.2. Visible Cross Section Results

Tables 9.1 and 9.2 show the measured visible cross sections for the different luminometers. The results are shown both with all corrections applied and with only some (or no) corrections applied, to show the effects of the different corrections. The exact values for the corrections, averaged over all scans, are summarized in the bottom part of the tables. The PCC and VTX results are obtained using five bunch crossings and therefore can differ from other detectors, where all 124 bunches are used to estimate the effect of each correction. The final visible cross section differs from the value with no corrections applied by up to 2–3% for PCC, HFOC and BCM1F, since the background correction effect for them is quite significant. For VTX and HFET, where background correction is taken as zero, the resulting total correction is less then 1%, reflecting the fact that different corrections have different signs and partially cancel each other in the final correction. Applied normalization corrections are the background correction BG, the peak position correction PP to take into account the offset in the non-scanning plane, the orbit drift correction OD, the beam-beam correction BB, the dynamic-β^* correction DB, the length scale calibration LSC, the ghost and satellite correction GS from bunch current normalisation, and the x-y correlation correction XYC[20] . All the corrections are applied sequentially.

While σ_{vis} is a property of the individual luminometer geometry, acceptance, and efficiency, and thus will inherently vary among the different luminometers, the measured convoluted beam width $\Sigma_{x,y}$ is a function of the beam and thus should be measured to be the same among all the luminometers. However, as shown in Section 9.1, while the general agreement in Σ is good, because of various instrumental effects there are some inconsistency both between luminometers and between individual scans for a single luminometer.

The overall visible cross section is determined by taking the weighted mean of the individual cross sections for the bunches used over the seven[21] scans taken.

[20]Not applied in the current analysis, as discussed in Section 7.6.
[21]The four regular scans and three beam imaging scans.

Some variation in the visible cross sections from scan-to-scan and bunch-to-bunch is observed. For the scan-to-scan variation, each scan is considered as an independent measurement and the standard deviation between seven scans is taken as a systematic uncertainty, resulting in an uncertainty of 0.32%. For the bunch-to-bunch variation, the error on the mean of the individual bunches of 0.05% is taken as the systematic uncertainty.

Table 9.1: Summary of measured visible cross sections in μb for BCM1F, HFET, HFOC, and PLT.

	PLT	HFOC	HFET	BCM1F
BG+PP+OD+BB+DB+LSC+GS+XYC (all corrections, XYC=0)	261.6 ± 1.6	805.9 ± 5.4	2503.6 ± 13.9	210.0 ± 1.3
BG+PP+OD+BB+DB+LSC+GS	261.6 ± 1.6	805.9 ± 5.4	2503.6 ± 13.9	210.0 ± 1.3
BG+PP+OD+BB+DB+LSC	260.7 ± 1.6	802.7 ± 5.4	2493.5 ± 13.9	209.1 ± 1.3
BG+PP+OD+BB+DB	262.7 ± 1.4	808.8 ± 5.4	2512.4 ± 14.1	210.7 ± 1.3
BG+PP+OD+BB	264.0 ± 1.4	812.6 ± 5.5	2523.9 ± 11.1	211.7 ± 1.3
BG+PP+OD	260.3 ± 1.4	801.0 ± 5.5	2486.9 ± 13.9	208.7 ± 1.3
BG+PP	260.1 ± 1.4	800.5 ± 5.4	2485.2 ± 13.9	208.6 ± 1.3
no corrections	263.7 ± 1.6	832.9 ± 8.4	2485.2 ± 13.9	214.3 ± 1.6
BG correction effect (%)	-1.56	-3.89	–	-2.66
OD correction effect (%)	+0.19	+0.19	+0.19	+0.19
BB correction effect (%)	+1.42	+1.44	+1.49	+1.43
DB correction effect (%)	-0.48	-0.47	-0.45	-0.47
LSC correction effect (%)	-0.75	-0.75	-0.75	-0.75
GS correction effect (%)	+0.40	+0.40	+0.40	+0.40
Total correction (%)	-0.73	-3.35	+0.73	-2.10

In Table 9.1 each detector uses its own measurement of the beam overlap Σ to compute the visible cross section. The uncertainties shown are determined from the average standard deviation of the bunch-to-bunch results. The final visible cross section has all normalization corrections applied. The corrections applied are the background correction (BG), the peak position correction (PP) to take into account the offset in the non-scanning plane, the orbit drift correction (OD), the beam-beam correction (BB), the dynamic-β^* correction (DB), the length scale calibration (LSC), the ghost and satellite corrections (GS), and the x-y correlation correction (XYC).

Since currently no x-y correlation is applied, the top row is identical to the following one.

Table 9.2: Summary of measured visible cross sections for PCC and VTX. Vertex counting with at least 14 tracks are used.

	PCC [b]	VTX [μb]
BG+PP+OD+BB+DB+LSC+GS+XYC (all corrections, XYC=0)	5.982 $\pm$ 0.037	29119 $\pm$ 142
BG+PP+OD+BB+DB+LSC+GS	5.982 $\pm$ 0.037	29119 $\pm$ 142
BG+PP+OD+BB+DB+LSC	5.958 $\pm$ 0.037	29002 $\pm$ 142
BG+PP+OD+BB+DB	6.033 $\pm$ 0.040	29322 $\pm$ 143
BG+PP+OD+BB	6.032 $\pm$ 0.042	29365 $\pm$ 150
BG+PP+OD	5.946 $\pm$ 0.036	28967 $\pm$ 139
BG+PP	5.949 $\pm$ 0.035	28984 $\pm$ 137
no corrections	6.105 $\pm$ 0.055	28984 $\pm$ 137
BG correction effect (%)	-2.56	–
OD correction effect (%)	-0.05	-0.05
BB correction effect (%)	+1.45	+1.37
DB correction effect (%)	-0.47	-0.49
LSC correction effect (%)	-0.75	-0.75
GS correction effect (%)	+0.40	+0.40
Total correction (%)	-2.06	+0.46

The uncertainties shown in Table 9.2 are determined from the average standard deviation of the bunch-to-bunch results. The final visible cross section has all normalization corrections applied on top of each other. The corrections applied are BG, PP, OD, BB, DB, LSC, GS, and XYC. Since currently no x-y correlation is applied, the top row is identical to the following one.

The PCC visible cross section results and statistical uncertainty after all normalization corrections are shown for all scans for the five bunches with pixel data on the left of Figure 9.4. The values for the visible cross sections are consistent within the uncertainties. On the right of Figure 9.4, the weighted average of the visible cross section over the five bunches is shown per scan, with only the background correction applied and with all normalization corrections applied. As the various normalization corrections have different signs, the change in the measured central value is small, but the standard deviation is reduced by a factor of 2. Figure 9.5 shows the same results for PLT. PLT results are available for all 124 bunch crossings colliding in the vdM scans, but only five bunch crossings are shown in the plot for comparison with PCC. Similar plots for HFOC, HFET, and BCM1F are shown in Appendix A.

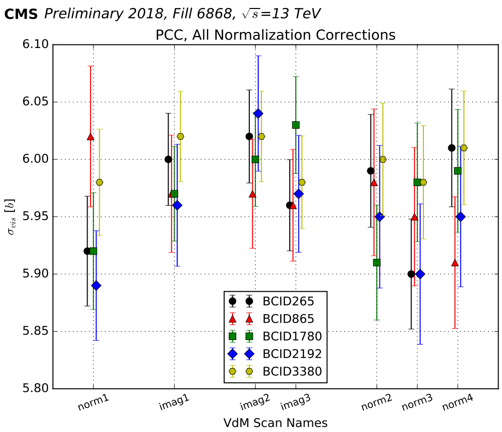

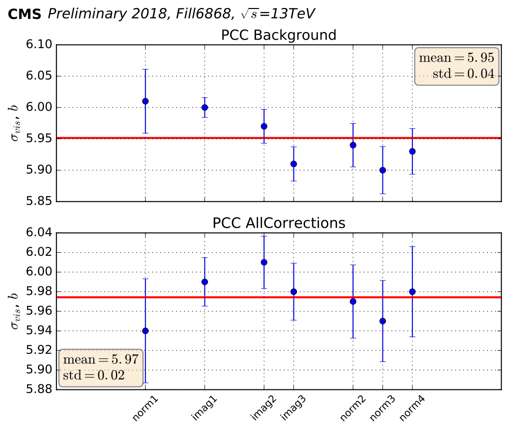

Figure 9.4: Left: Measured PCC visible cross section for all vdM scans, for the five bunch crossings with pixel data available. Right: The measured visible cross section for each scan, together with the weighted average (red line), with only the background correction applied (top) and with all corrections applied (bottom).

9.2.1. Cross-Detector Consistency

After the final calculation of the individual cross sections, the total integrated luminosity for the periods in the vdM scan fill when no scans were taking place, are also calculated.[22]

[22]Only the colliding bunches are included in the calculation, so possible noise contributions in the non-colliding bunches do not have any effect.

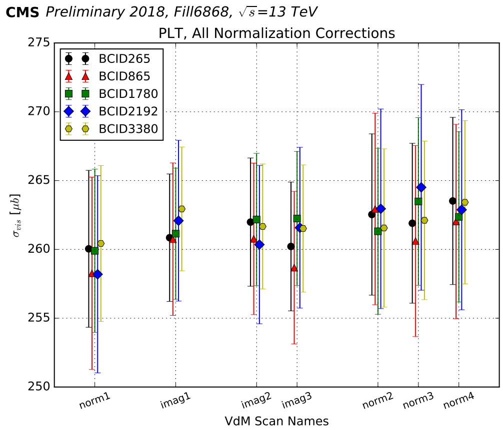

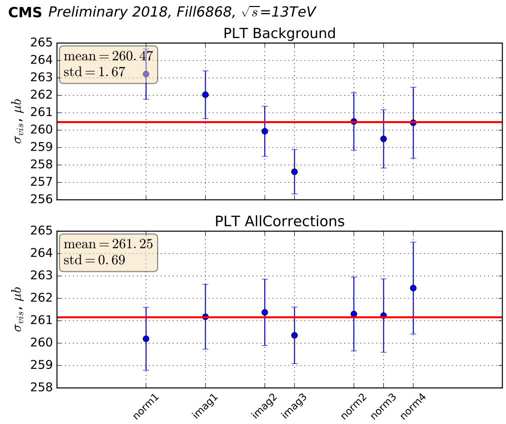

Figure 9.5: Left: Measured PLT visible cross section for all vdM scans, for the five bunch crossings with pixel data available. Right: The measured visible cross section for each scan, together with the weighted average (red line), with only the background correction applied (top) and with all corrections applied (bottom).

Since these periods feature a nearly constant luminosity at very low pileup, any effects due to non-linearity should be negligible and hence the measurements should be equal among the different luminometers.

However, a small difference of approximately 0.5% is observed. Figure 9.6 shows the luminosity for the different luminometers during the vdM fill, in which the remaining residual differences can be observed in the zoomed region. The three gray shaded rectangles indicate the periods used to calculate the total integrated luminosity for the cross-detector comparison. Table 9.3 shows the integrated luminosity values together with the residual differences. The rate data for the calculation of total integrated luminosity is not presented in this thesis. However, the σ_{vis} values used for the same calculation can be found in Table 9.1 and Table 9.2.

It is assigned a systematic uncertainty of 0.5%, the largest variation observed from the average, as a measure of the uncertainty from the cross-detector consistency in the vdM fill.

Table 9.3: Summary of measured integrated luminosity during stable periods in the vdM fill. The third column indicates the difference between the luminosity and the average.

Luminometer	Integrated luminosity (nb^{-1})	Difference from average
HFET	42.16	+0.1%
BCM1F	41.91	-0.5%
PLT	42.22	+0.2%
HFOC	41.99	-0.3%
PCC	42.31	+0.5%

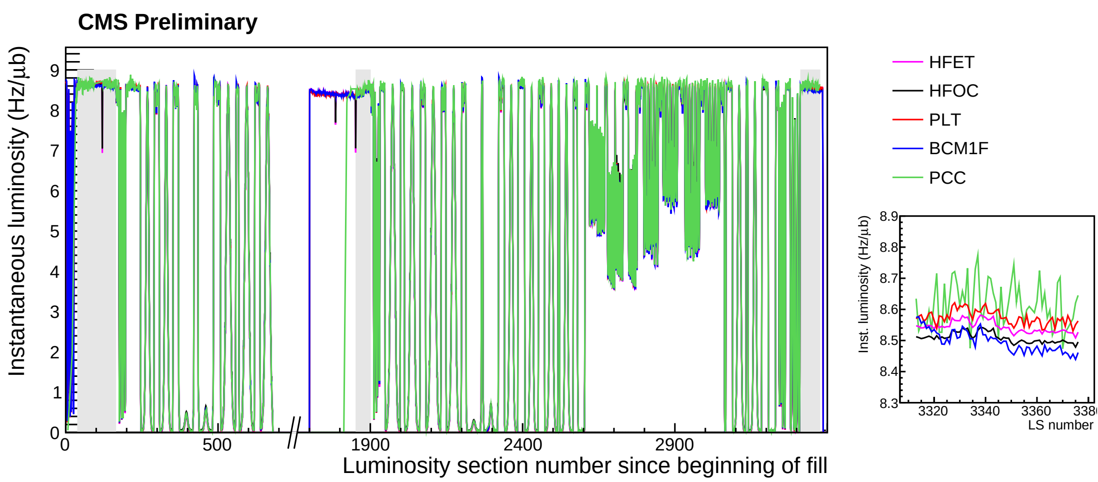

Figure 9.6: Instantaneous luminosity for the five independent luminometers during the vdM scan fill, showing the general agreement between all five luminometers through all the scans.

9.3. Linearity and Efficiency Corrections from Emittance Scans

An ideal luminometer would have a perfectly linear response as a function of the instantaneous luminosity, with a single calibration constant relating the two.

In practice, some nonlinear effects, as described in Chapter 5, affect any real luminometer, and various instrumental effects can cause changes in the efficiency (and hence calibration constant) over the course of the year.

In 2015–2016, testing the linearity and stability of a luminometer could only be done by comparison to a second reference luminometer, in which case it is not necessarily clear which luminometer (or both) is the source of the observed behavior. However, in 2017–2018, we can take advantage of emittance scan data in order to derive linearity and stability corrections using only data intrinsic to a single luminometer.

Emittance scans have been historically used by LHC to estimate beam size and calibrate LHC instruments. However, as these scans operate on the same principle as van der Meer scans, they can also provide similar data when both horizontal and vertical scans are performed. These scans can thus also provide useful data to CMS, and so in 2017–2018 CMS has used these scans to obtain additional information on luminometer performance.

In 2018, emittance scans consisted of 9 scan points with 10 seconds integration time at each scan point, with a maximum separation of approximately $\pm 3\sigma$. Scans are typically performed at the beginning of LHC fills ('early' scan) and again at the end of the fill ('late' scan), unless the beam is dumped unexpectedly.

Pile-up and beam optics are not adjusted; rather, the standard parameters used in physics data production are maintained. The number of scan points and their duration are both substantially reduced. Such reduced information, particularly in the tails, poses one of the most significant challenges of this analysis. Figure 9.7 shows a typical scan pair fit with a single Gaussian model.

After the scan, additional offline corrections are applied to emittance scan data. In particular, it was noticed that the bunch current measured by FBCT in the first bunch crossing of the train is approximately 1% higher in comparison to beam synchrotron radiation telescope (BSRT)[23] [35]. Therefore, currents for all leading bunches in the train were corrected offline. The FBCT/DCCT correction described in Section 7.7 was performed, and all 2018 emittance scan data was reanalyzed.

[23] Allows to take profiles of the transverse beam distribution. [42]

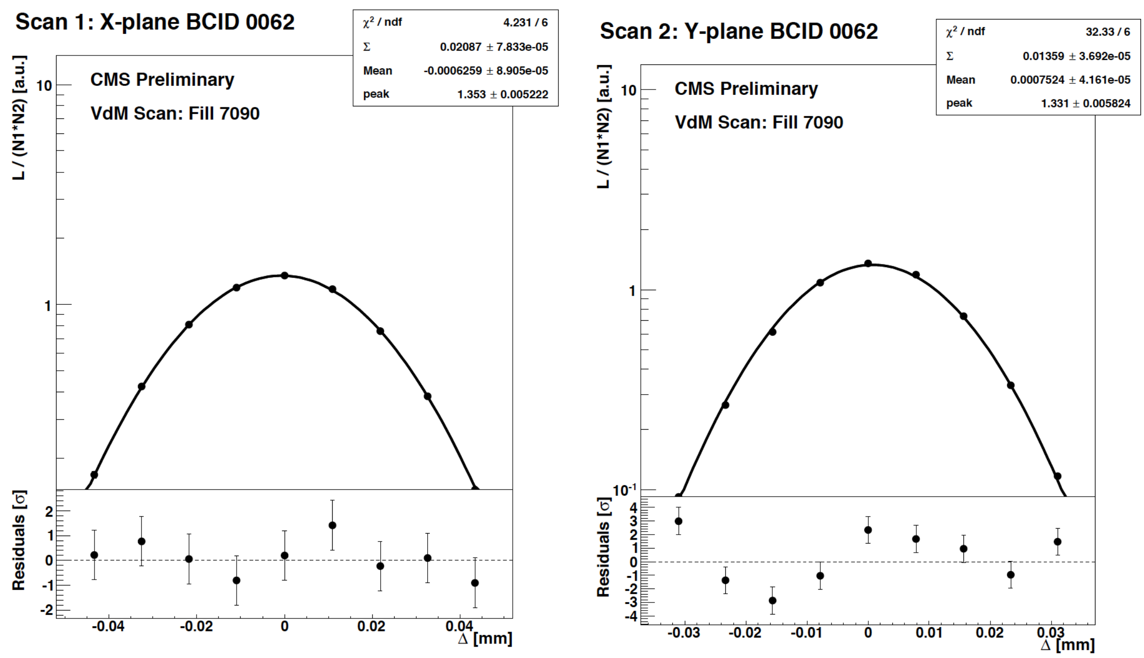

Figure 9.7: Fitted emittance scan data (with 9 points) for HFET data for an emittance scan taken in fill 7090 for BCID 62 for the x (left) and y (right) scan.

In addition, it was taken into account that beams are not always exactly at head-on position in the non-scanning plane in emittance scans, since bunches in the train experience additional kick from the magnets. The position of the whole bunch train can be shifted with respect to the other bunch trains, as seen in Figure 9.8 for the bunch trains around BCIDs 750-850. The offset of the mean in the x-direction is taken into account when analyzing the emittance scan in y and vice versa. The peak position correction results in an increase of approximately 2% in the average visible cross section. However, it does not reduce bunch-to-bunch variation or variation between early and late scans.

9.3.1. Figure of Merit Analysis

In 2018, a Figure of Merit (FOM) analysis is performed based on the emittance scans to track stability and linearity over the year.

In a normal vdM fit the rates in a detector, which are normalised by the beam current products, are fitted bunch by bunch to obtain the visible cross sections σ_{vis}.

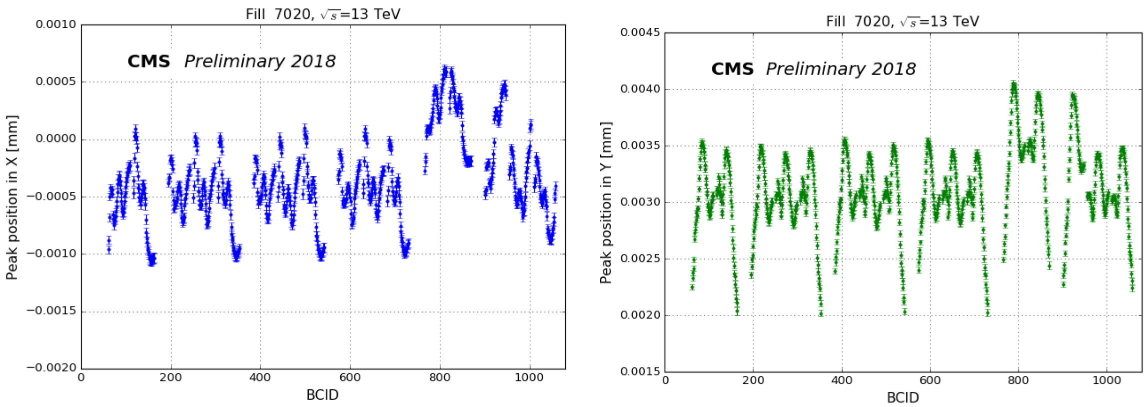

Figure 9.8: Position of the mean of the single Gaussian fit to emittance scan data in x (left) and in y (right). HFOC data is used from fill 7020. Only the first 1100 BCIDs are shown.

In the emittance scans the goal is not to obtain the absolute cross section, but rather to track stability. Since these scans are typically carried out at standard physics luminosities, the effects of non-linearity in a detector will distort the (typically) Gaussian shape of the fit. In the FOM analysis the rates are corrected by the nominal non-linearity of a detector,[24] and the peak is normalised to the visible cross section obtained during the relevant normal vdM scan. The resulting FOM value is typically then close to the value 1, and its deviation from 1 is a measure of the instability of the detector. In this way long-term drifts, for example due to radiation damage, can be tracked using the emittance scans.

Given an emittance scan with measured beam overlap widths $\Sigma_{x,y}$, the figure of merit R is given by,

$$R = \frac{2\pi \mathcal{L}_0 \Sigma_x \Sigma_y}{N_1 N_2 f} \tag{9.1}$$

where the variables are as in Equation 6.11 and $\mathcal{L}_0$ is the luminosity at the peak of the scan. Essentially, the figure of merit gives the ratio of the σ_{vis} implied by the emittance scan to the σ_{vis} obtained from the vdM scan.

[24]Determined in, for example, specialized ‘mu scans’, as described in Section 9.3.4.

9.3.2. Extracting Linearity

In 2018, the single bunch instantaneous luminosity (SBIL) at the beginning of a fill was typically approximately 7–8 Hz/μb, falling to 2–4 Hz/μb by the end of the fill. There is ≈1% difference observed between cross sections extracted in the early and late emittance scans, which originally was attributed to the non-linearity of the detectors. In addition, there is considerable variation among the individual bunch crossings at any given time.

Given the SBIL variations within a fill, a wide range of SBIL can be probed in the data from each emittance scan. Figure 9.9 shows the visible cross sections obtained for HFOC and PLT as a function of SBIL in fill 7110. The results for leading bunches (red) and train bunches (blue) are shown separately with linear fits. It is observed that there is some dependence on the SBIL, and that this dependence is slightly different for leading bunches than train bunches. There are no corrections applied to the plotted visible cross sections in Figure 9.9.

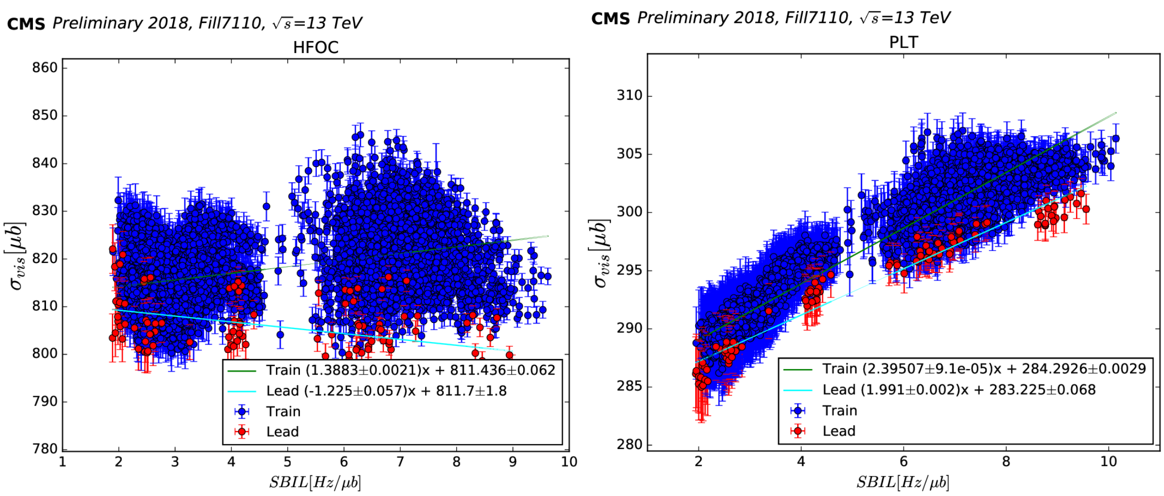

Figure 9.9: Visible cross section obtained from early (with high SBIL) and late (with low SBIL) emittance scan data as a function of SBIL for HFOC (left) and PLT (right).

The resulting variation of SBIL is used to derive corrections that are applied to the measured rates. In practice, quadratic corrections to the rates are used in a few running periods where the linearity is observed to have changed. This is typically a function of filling scheme. The non-linearities for leading and train bunches are often different. Since different filling schemes have different fractions of leading (and isolated) bunches compared to standard bunches in bunch trains, the overall non-linearity is a combination of the two. Changes in detector conditions can also imply some long-range time dependence in linearity as well. In either case, the procedure is the same for checking the linearity after corrections.

The detector-specific non-linearity corrections derived from the emittance scan data amount to approximately 1.5–2.6% (Hz/μb) in PLT, 0.20–0.25% (Hz/μb) in HFET, and 1.4–1.7% (Hz/μb) in BCM1F, varying over the course of the year as described above. For PCC, HFOC, and DT, no additional non-linearity correction is applied.

9.3.3. Extracting Efficiency

After linearity is corrected for all the fills, an average cross section per fill is computed. These cross sections are not taken as absolute calibrations but are instead used to estimate changes in detector efficiency as a function of time. These are then used to derive corrections to the observed rates to account for the efficiency losses in a detector, in order to restore approximately constant performance over the course of the year.

9.3.4. Mu Scans

In addition to the emittance scans, three other special scans, called 'mu-scans', were performed to evaluate the luminometer linearity. These scans are carried out during regular physics fills, but in a different fashion from regular vdM scans. Since the purpose is not to measure the beam shape, but to evaluate the luminometer performance as a function of SBIL, the steps are instead chosen so that the resulting SBIL is in steps of 1 Hz/μb in the range 1–7 Hz/μb. The scan is only performed in one direction (the y-direction) and the length of each step is chosen so that the statistical uncertainties for PCC are equal for each step.

Two mu-scans were performed during regular physics fills, fill 7274 on October 10 and fill 7320 on October 19, and one during a special high-pileup machine development fill, fill 7358 on October 26, which allows to probe linearity at very high SBIL.[25]

Figure 9.10 shows the results from the fill 7358 for a single bunch. The HFET/PCC ratio and HFOC/PCC ratio can be probed up to a very high SBIL.

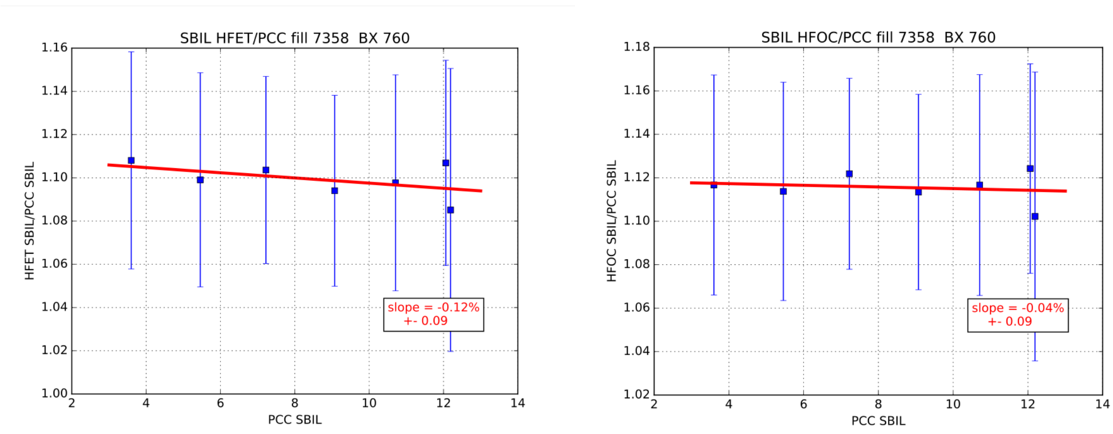

Figure 9.10: Linearity data obtained from the high-pileup machine development fill 7358. The results show the HFET/PCC ratio (left) and HFOC/PCC ratio (right) as a function of SBIL.

[25]Up to approximately 18 Hz/μb in the highest-luminosity bunches.

10. CONCLUSION

Luminosity is the quantity of a particle collider's ability to create interactions between its colliding particles. Measurement of this quantity is essential to the high energy physics studies since it both indicates the performance of the particle accelerator and gives a normalizing factor to the observed particle productions for the further calculations of specific particle production cross sections. However, luminosity measurement is a challenging process due to the unknown cross section of proton-proton interactions. So instead, the visible cross sections special to each detector are extracted from vdM scan data to calculate the luminosity.

This thesis is devoted to the extraction of the luminosity calibration constants using 2018 vdM scans data collected at $\sqrt{s} = 13$ TeV for proton-proton (pp) collisions. Table 10.1 shows the summary of the systematic uncertainties entered into the calculation of these calibration constants due to each systematic effect. Accordingly, the calibration constants presented in this thesis were obtained with a precision of 2.1%.

The extraction of linearity and stability of the detectors using the emittance scan analysis is a relatively new approach that started to be used only in 2017. It allows gathering information about a detector without relying on another detector. The standard cross-detector analysis method is unreliable since the origin of the observed effect becomes ambiguous. The emittance scan analysis is an effective method with promising results taken in 2018.

Table 10.1: Summary of the systematic uncertainties entering the luminosity calibration constants measurement for $\sqrt{s} = 13$ TeV pp collisions collected in 2018.

Systematic	Correction (%)	Uncertainty (%)
Length scale	-0.8	0.2
Orbit drift	0.2	0.1
x-y non-factorization	0.0	2.0
Beam-beam	1.5	0.2
Dynamic-β^*	-0.5	
Beam current calibration	2.3	0.2
Ghosts and satellites	0.4	0.1
Scan to scan variation	—	0.3
Bunch to bunch variation	—	0.1
Cross-detector consistency	—	0.5
Background subtraction	0 to 0.8	0.1
Total		2.1

REFERENCES

1. Evans, L. and P. Bryant, "LHC Machine", *Journal of Instrumentation*, Vol. 3, No. 08, pp. S08001–S08001, aug 2008.

2. Team, A., "The Four Main LHC Experiments", , Jun 1999, `https://cds.cern.ch/record/40525`.

3. Bachy, G., P. Bonnal and P. E. Faugeras, *Planning and Scheduling for the Large Hadron Collider Project*, Tech. rep., CERN, Geneva, Feb 1996, `https://cds.cern.ch/record/307862`.

4. Mobs, E., "The CERN Accelerator Complex - 2019. Complexe des Accélérateurs du CERN - 2019", , Jul 2019, `https://cds.cern.ch/record/2684277`, general Photo.

5. Alemany, R., M. Lamont, S. Page, M. Albert, M. Arrut, H. Burkhardt, A. Butterworh, E. Carlier, S. Deghaye, M. Ferro-Luzzi, B. Goddard, J.-J. Gras, M. Gruwe, L. Jensen, R. Jones, V. Kain, Q. King, G. Kruk, J. Lewis, D. Macina, A. Macpherson, D. Manglunki, L. Ponce, B. Puccio, S. Redaelli, W. Venturini, J. Wenninger, R. Bailey, P. Collier and S. Myers, "LHC Run Modes", *LHC-OP-ES-0005 rev 1.0*, 2007.

6. Sakuma, T., "Cutaway Diagrams of CMS Detector", *CMS Collaboration*, May 2019, `http://cds.cern.ch/record/2665537`.

7. Bayatian, G. L. *et al.*, "CMS Physics: Technical Design Report Volume 1: Detector Performance and Software", *CERN-LHCC-2006-001, CMS-TDR-8-1*, 2006.

8. Dominguez, A., D. Abbaneo, K. Arndt, N. Bacchetta, A. Ball, E. Bartz, W. Bertl, G. M. Bilei, G. Bolla, H. W. K. Cheung, M. Chertok, S. Costa, N. Demaria, D. D. Vazquez, K. Ecklund, W. Erdmann, K. Gill, G. Hall, K. Harder,

F. Hartmann, R. Horisberger, W. Johns, H. C. Kaestli, K. Klein, D. Kotlinski, S. Kwan, M. Pesaresi, H. Postema, T. Rohe, C. Schäfer, A. Starodumov, S. Streuli, A. Tricomi, P. Tropea, J. Troska, F. Vasey and W. Zeuner, *CMS Technical Design Report for the Pixel Detector Upgrade*, Tech. rep., Sep 2012, `https://cds.cern.ch/record/1481838`.

9. Chatrchyan, S. *et al.*, "The CMS Experiment at the CERN LHC", *JINST*, Vol. 3, p. S08004, 2008.

10. Layter, J. G., *The CMS Muon Project: Technical Design Report*, Technical design report. CMS, CERN, Geneva, 1997, `http://cds.cern.ch/record/343814`.

11. Herr, W. and B. Muratori, "Concept of Luminosity", *CERN-2006-002*, pp. 361–378, 2006.

12. Wikipedia contributors, "Event (particle physics) — Wikipedia, The Free Encyclopedia", `https://en.wikipedia.org/w/index.php?title=Event_(particle_physics)&oldid=885937084`, 2019, [Online; accessed 07-June-2021].

13. Wikipedia contributors, "Cross Section (physics) — Wikipedia, The Free Encyclopedia", `https://en.wikipedia.org/w/index.php?title=Cross_section_(physics)&oldid=1021210473`, 2021, [Online; accessed 07-June-2021].

14. Hempel, M. and W. Lohmann, "Development of a Novel Diamond Based Detector for Machine Induced Background and Luminosity Measurement", *DESY-THESIS-2017-030*, 2017.

15. Lujan, P., "Performance of the Pixel Luminosity Telescope for Luminosity Measurement at CMS During Run 2", *CMS CR -2017/347*, 2017.

16. Copy, B., E. Mandilara, I. Prieto Barreiro and F. Varela, "Monitoring of CERN's Data Interchange Protocol (DIP) System", *16th International Conference on Accelerator and Large Experimental Physics Control Systems*, 1 2018.

17. Gutleber, J. and L. Orsini, "Software Architecture for Processing Clusters Based on I2O", *ClusterComputing, the Journal of Networks, Software and Applications, Kluwer Academic Publishers*, 2002.

18. van der Meer, S., "Calibration of the Effective Beam Heights in the ISR", *CERN Internal Report ISR-PO/68-31*, 1968.

19. Barschel, C., M. Ferro-Luzzi, J.-J. Gras, M. Ludwig, P. Odier and S. Thoulet, *Results of the LHC DCCT Calibration Studies*, Tech. Rep. CERN-ATS-Note-2012-026 PERF, 2012, `https://cds.cern.ch/record/1425904`.

20. Belohrad, D., L. Jensen, O. Jones, M. Ludwig and J. Savioz, *The LHC Fast BCT System: A Comparison of Design Parameters with Initial Performance*, Tech. Rep. CERN-BE-2010-010, 2010, `https://cds.cern.ch/record/1267400`.

21. Jeff, A., M. Andersen, A. Boccardi, S. Bozyigit, E. Bravin, T. Lefevre, A. Rabiller, F. Roncarolo, C. P. Welsch and A. S. Fisher, "Longitudinal Density Monitor for the LHC", *Phys. Rev. ST Accel. Beams*, Vol. 15, p. 032803, 2012.

22. Jeff, A., *A Longitudinal Density Monitor for the LHC*, Ph.D. Thesis, Liverpool University, 2012, `https://cds.cern.ch/record/1513180`.

23. Gasior, M., J. Olexa and R. Steinhagen, "BPM Electronics Based on Compensated Diode Detectors — Results from Development Systems", *Conf. Proc.*, Vol. C1204151, p. MOPG010, 2012, `http://cds.cern.ch/record/1476070`.

24. Zanetti, M., *Beams Scan Based Absolute Normalization of the CMS Luminosity Measurement*, Tech. Rep. CERN-Proceedings-2011-001, 2011, `https://cds.cern.ch/record/1357856`.

25. O. Karacheban, P. T. o. b. o. C., "Emittance Scans for CMS Luminosity Calibration", *EPJ Web of Conferences 201 (2019) 04001*, 2019.

26. *CMS Luminosity Measurement for the 2018 Data-taking Period at* $\sqrt{s} = 13$ TeV, Tech. rep., CERN, Geneva, 2019, https://cds.cern.ch/record/2676164.

27. Bassetti, M. and G. Erskine, "Closed Expression for the Electrical Field of a Two-Dimensional Gaussian Charge", *CERN-ISR-TH/80-06*, March 1980.

28. Bambade, P., R. Erickson, W. Koska, W. K. N. Phinney and S. Wagner, "Observation of Beam-beam Deflections at the Interaction Point of the SLAC Linear Collider", *Phys. Rev. Lett.*, Vol. 62, (1989) 2949.

29. Kozanecki, W., T. Pieloni and J. Wenninger, "Observation of Beam-beam Deflections with LHC Orbit Data", *CERN-ACC-NOTE-2013-0006*, 2013.

30. Babaev, A., "Beam-dynamic Effects at the CMS BRIL van der Meer Scans", *JINST 13 C03028*, 2018.

31. et al., R. A.-F., "Cross-calibration of the LHC Transverse Beam-profile Monitors", *Proceedings, 8th International Particle Accelerator Conference (IPAC 2017)*, 2017.

32. CMS Collaboration, *CMS Luminosity Based on Pixel Cluster Counting - Summer 2012 Update*, CMS Physics Analysis Summary CMS-PAS-LUM-12-001, 2012, https://cds.cern.ch/record/1482193.

33. Klute, M., C. Medlock and J. Salfeld-Nebgen, "Beam Imaging and Luminosity Calibration", *JINST*, Vol. 12, p. P03018, 2017.

34. Palm, M., *BSRL Analysis: VdM Scans and Other Issues in 2017-2018*, LHC Luminosity Calibration and Monitoring Working Group presentation, 2018, https://indico.cern.ch/event/775187/contributions/3221948/.

35. Kral, J. and O. Sedlacek, *Bunch-dependent Response of FBCT with Bunch Trains*, LHC Luminosity Calibration and Monitoring Working Group presentation, 2018, https://indico.cern.ch/event/775187/contributions/3221928/.

36. Barschel, C., *Precision Luminosity Measurement at LHCb with Beam-gas Imaging*, Ph.D. Thesis, RWTH Aachen University, 2014, https://cds.cern.ch/record/1693671.

37. Coombs, G., *LHCb Ghost Charge Update*, LHC Luminosity Calibration and Monitoring Working Group presentation, 2018, https://indico.cern.ch/event/775187/contributions/3221952/.

38. Brun, R., F. Rademakers and S. Panacek, "ROOT, An Object Oriented Data Analysis Framework", *2000 CERN School of Computing*, pp. 11–41, 2000, https://cds.cern.ch/record/491486.

39. Copy, B., E. Mandilara, I. Prieto Barreiro and F. Varela, "Monitoring of CERN's Data Interchange Protocol (DIP) system", p. THPHA162. 4 p, 2018, https://cds.cern.ch/record/2305320.

40. "Introducing JSON", https://www.json.org/json-en.html, accessed: 07-06-2021.

41. Wikipedia contributors, "Comma-separated Values — Wikipedia, The Free Encyclopedia", https://en.wikipedia.org/w/index.php?title=Comma-separated_values&oldid=1022773018, 2021, [Online; accessed 09-June-2021].

42. Fitterer, M., G. Stancari, S. Papadopoulou, Y. Papaphilippou and S. Redaelli, *Analysis of BSRT Profiles in the LHC at Injection*, Tech. rep., Dec 2017, https://cds.cern.ch/record/2621636.

APPENDIX A: ADDITIONAL PLOTS FOR $\Sigma_{x,y}$ AND $\sigma_{\mathbf{vis}}$

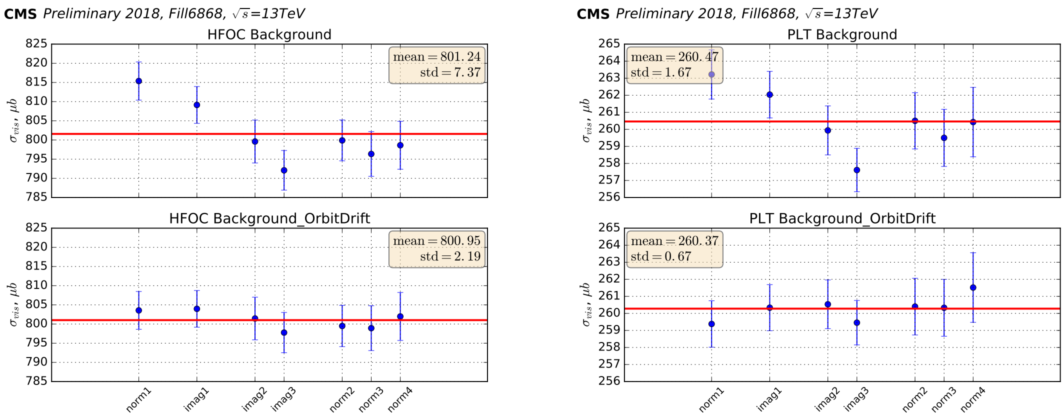

Figure A.1: Measured visible cross sections for all vdM scans before (top) and after (bottom) the orbit drift correction is applied for HFOC (left) and PLT (right). Significant improvement in the scan-to-scan agreement is observed.

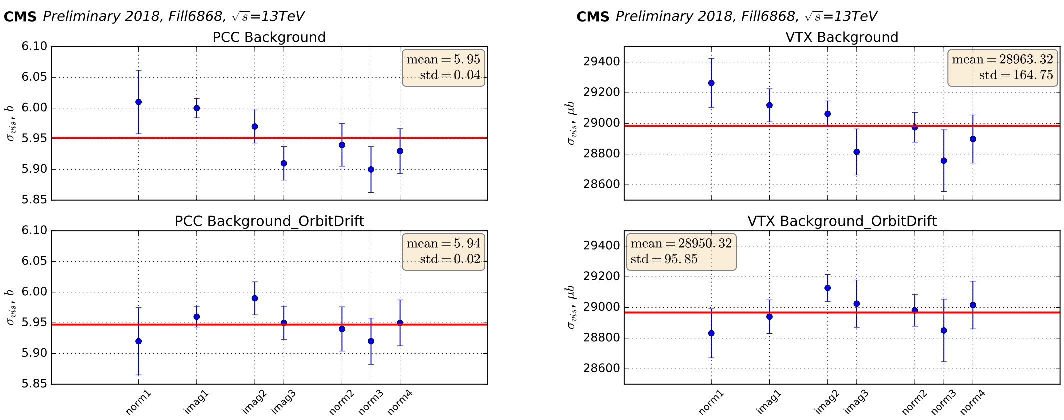

Figure A.2: Measured visible cross sections for all vdM scans before (top) and after (bottom) the orbit drift correction is applied for PCC (left) and VTX (right). Significant improvement in the scan-to-scan agreement is observed.

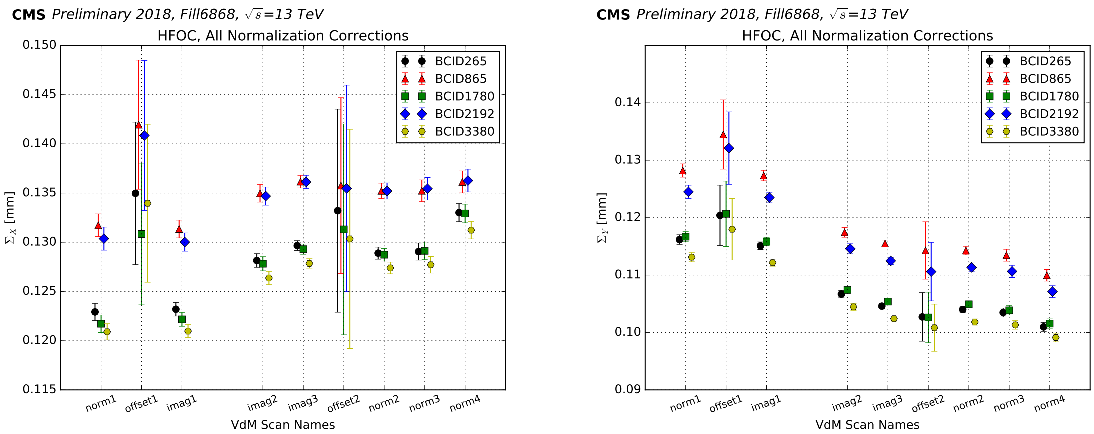

Figure A.3: The convoluted beam width measured by HFOC in the x (left) and y (right) direction (Σ_x and Σ_y) after all normalization corrections have applied for the five bunch crossings with PCC data available. The uncertainty shown is statistical. The beam size increases in the x-direction and decreases in y over time.

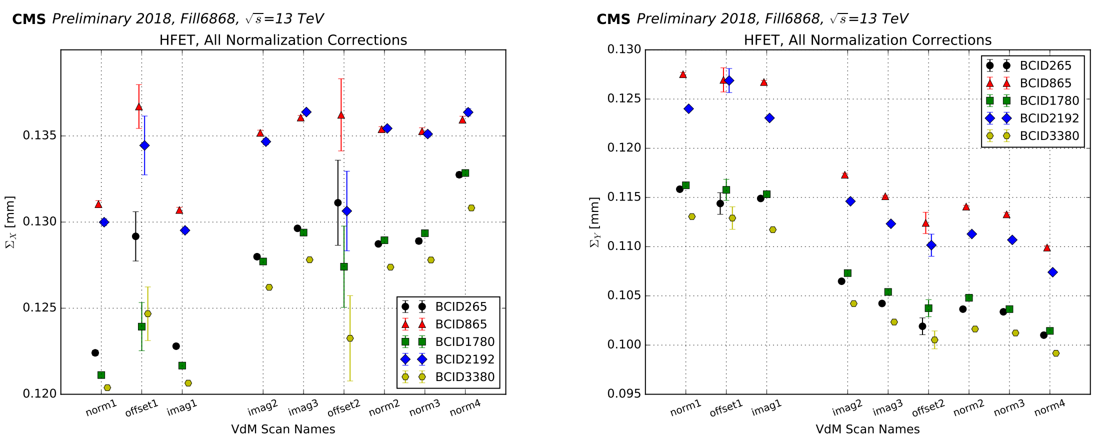

Figure A.4: The convoluted beam width measured by HFET in the x (left) and y (right) direction (Σ_x and Σ_y) after all normalization corrections have applied for the five bunch crossings with PCC data available. The uncertainty shown is statistical. The beam size increases in the x-direction and decreases in y over time.

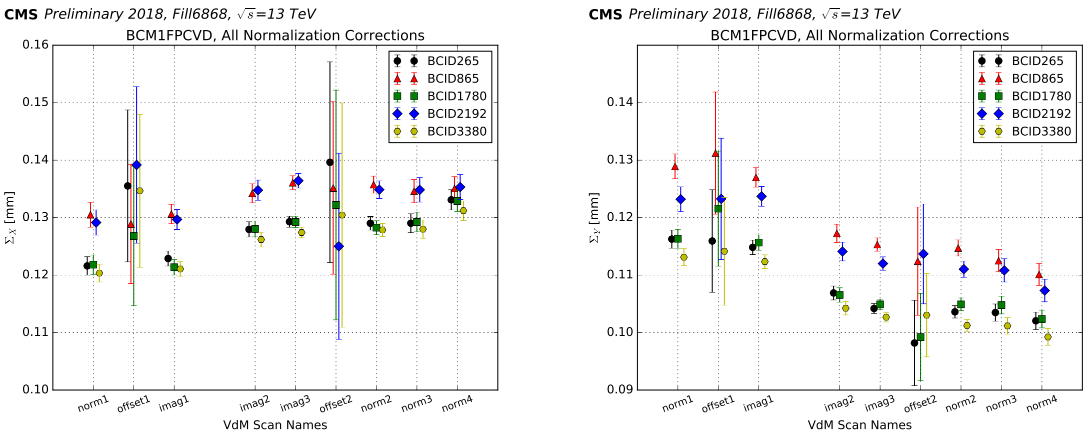

Figure A.5: The convoluted beam width measured by BCM1F in the x (left) and y (right) direction (Σ_x and Σ_y) after all normalization corrections have applied for the five bunch crossings with PCC data available. The uncertainty shown is statistical. The beam size increases in the x-direction and decreases in y over time.

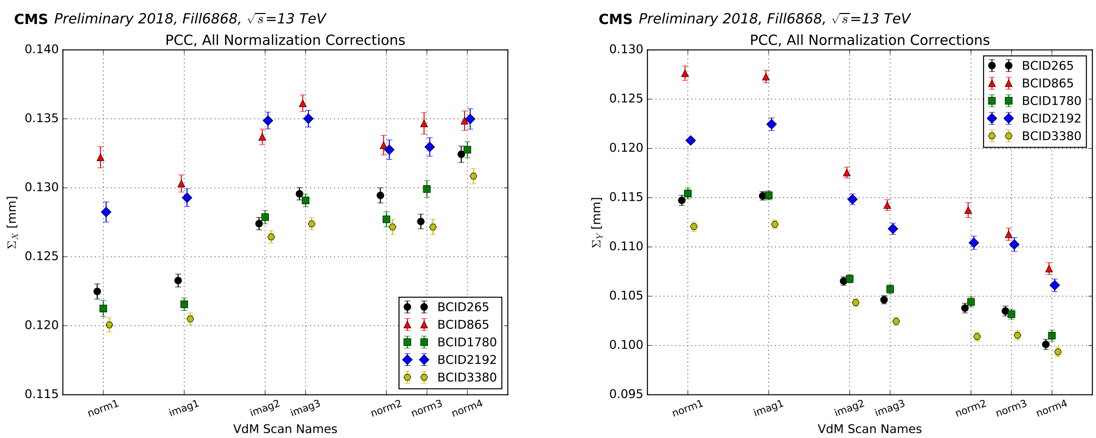

Figure A.6: The convoluted beam width measured by PCC in the x (left) and y (right) direction (Σ_x and Σ_y) after all normalization corrections have applied for the five bunch crossings with PCC data available. The uncertainty shown is statistical. The beam size increases in the x-direction and decreases in y over time.

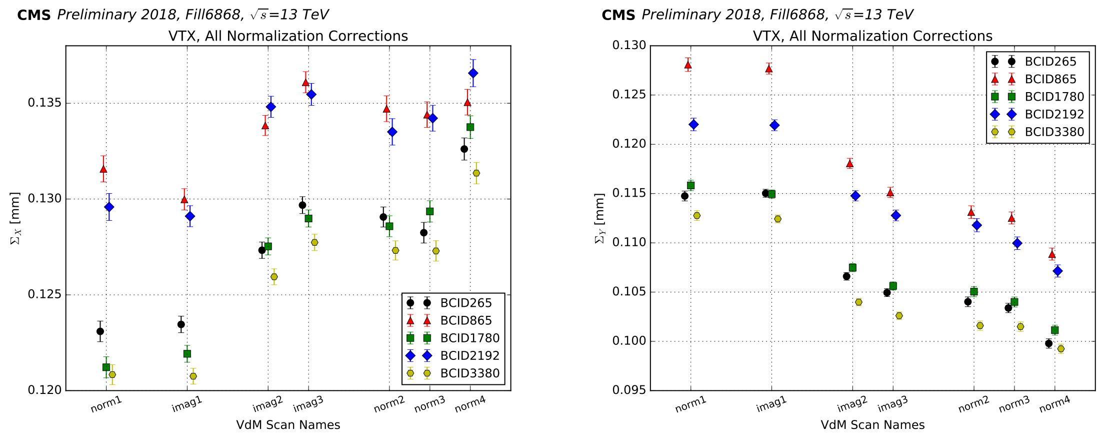

Figure A.7: The convoluted beam width measured by VTX in the x (left) and y (right) direction (Σ_x and Σ_y) after all normalization corrections have applied for the five bunch crossings with PCC data available. The uncertainty shown is statistical. The beam size increases in the x-direction and decreases in y over time.

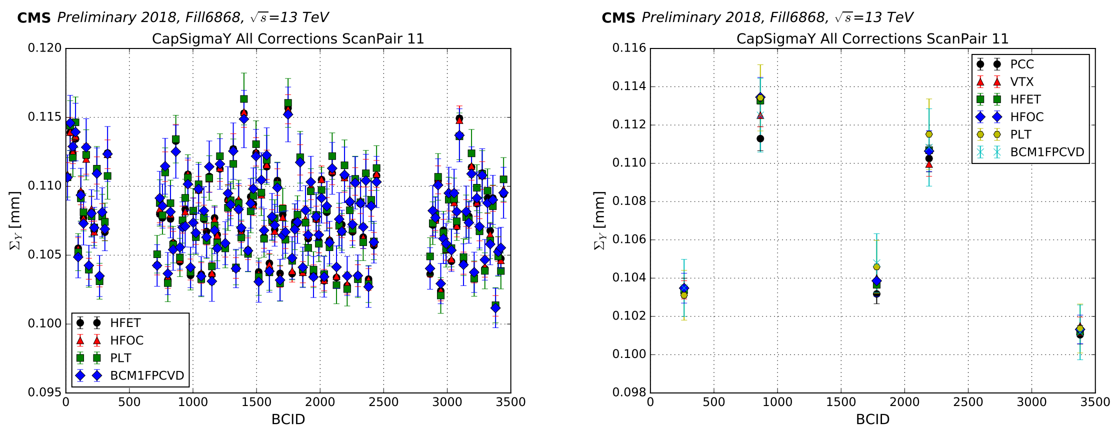

Figure A.8: Convoluted beam width (Σ_y) measured in a normal vdM scan (norm3) for all colliding bunches for all online luminometers (HFET, HFOC, PLT, BCM1F) on the left and for the 5 bunch crossings available for PCC and vertexes together with online detectors on the right. The measurements from all detectors agree within the statistical error bars.

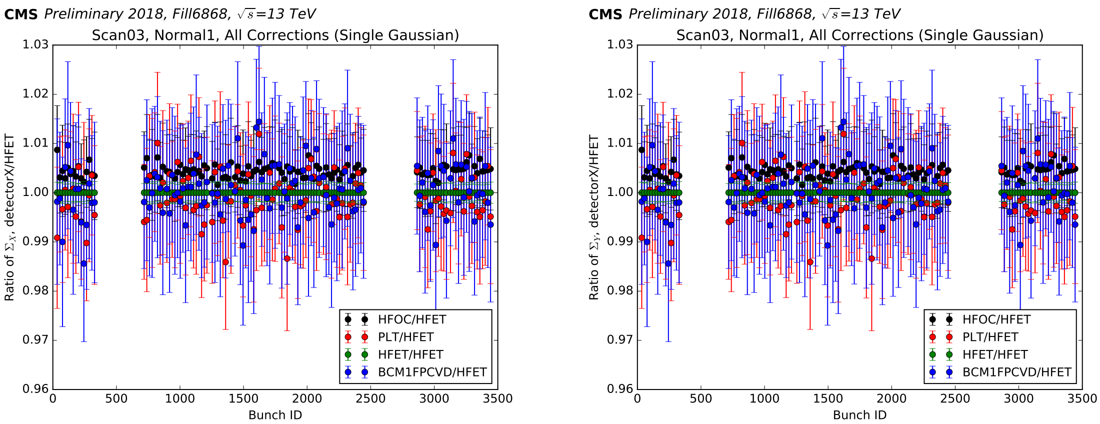

Figure A.9: Ratio of Σ_x (left) and Σ_y (right) for each bunch crossing in a normal VdM scan pair (norm1) for each of the online luminometers (HFET, HFOC, PLT, BCM1F) to $\Sigma_{x,y}$ of HFET.

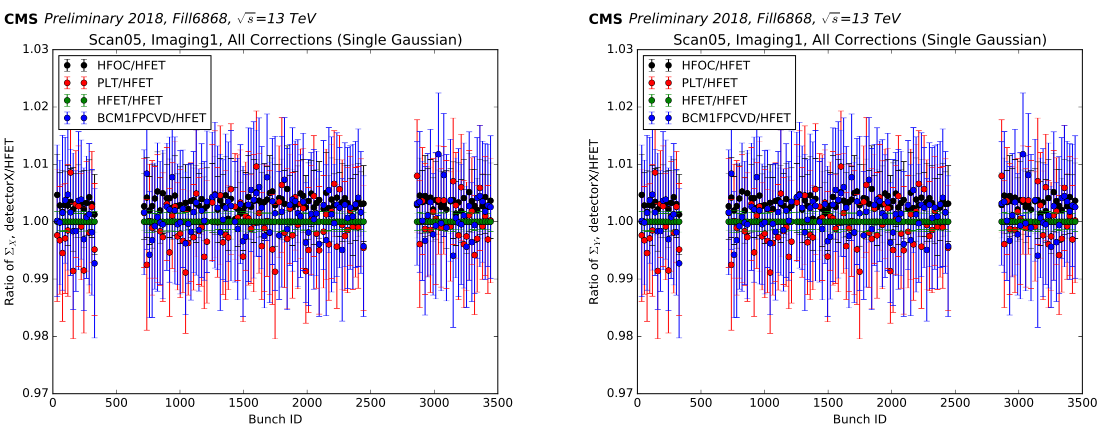

Figure A.10: Ratio of Σ_x (left) and Σ_y (right) for each bunch crossing in an imaging vdM scan pair (imag1) for each of the online luminometers (HFET, HFOC, PLT, BCM1F) to $\Sigma_{x,y}$ of HFET.

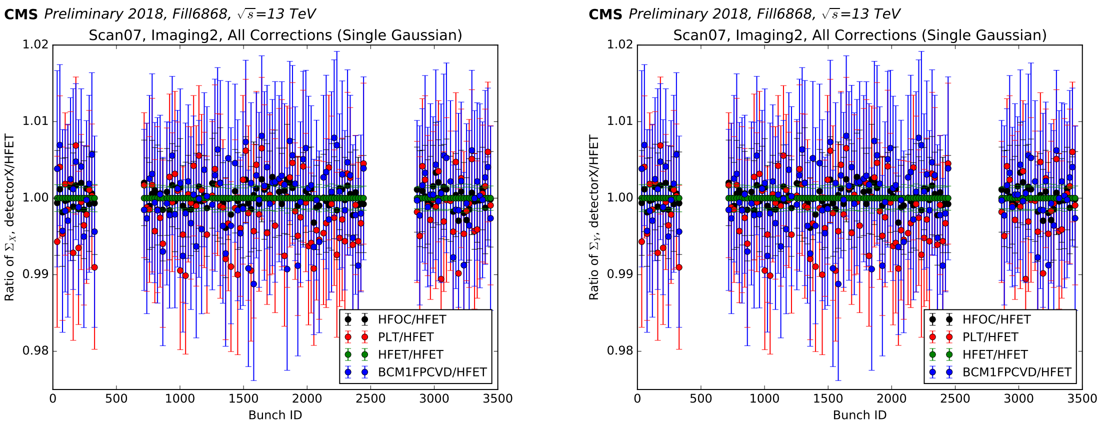

Figure A.11: Ratio of Σ_x (left) and Σ_y (right) for each bunch crossing in an imaging vdM scan pair (imag2) for each of the online luminometers (HFET, HFOC, PLT, BCM1F) to $\Sigma_{x,y}$ of HFET.

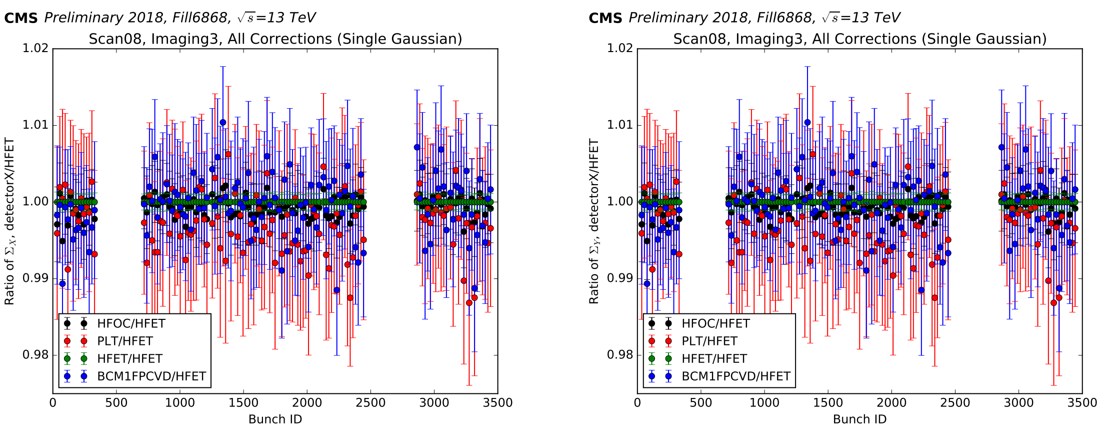

Figure A.12: Ratio of Σ_x (left) and Σ_y (right) for each bunch crossing in an imaging vdM scan pair (imag3) for each of the online luminometers (HFET, HFOC, PLT, BCM1F) to $\Sigma_{x,y}$ of HFET.

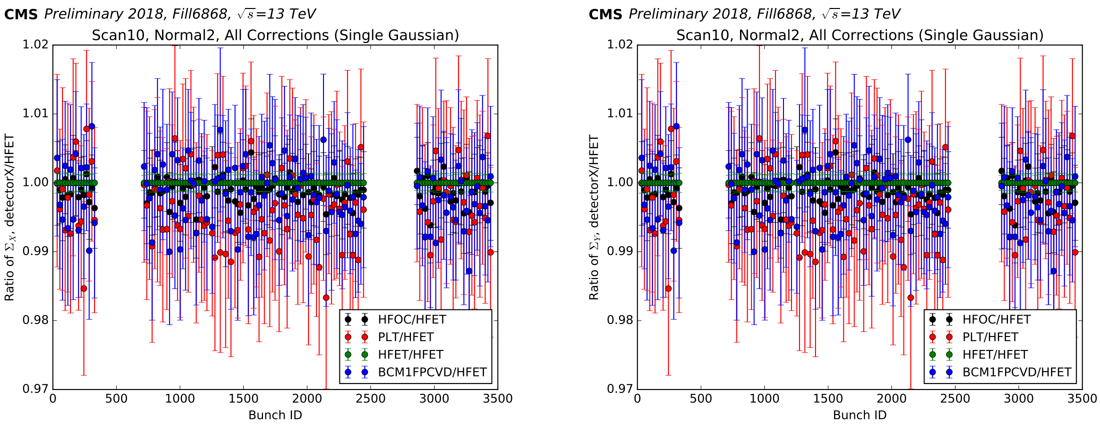

Figure A.13: Ratio of Σ_x (left) and Σ_y (right) for each bunch crossing in a normal vdM scan pair (norm2) for each of the online luminometers (HFET, HFOC, PLT, BCM1F) to $\Sigma_{x,y}$ of HFET.

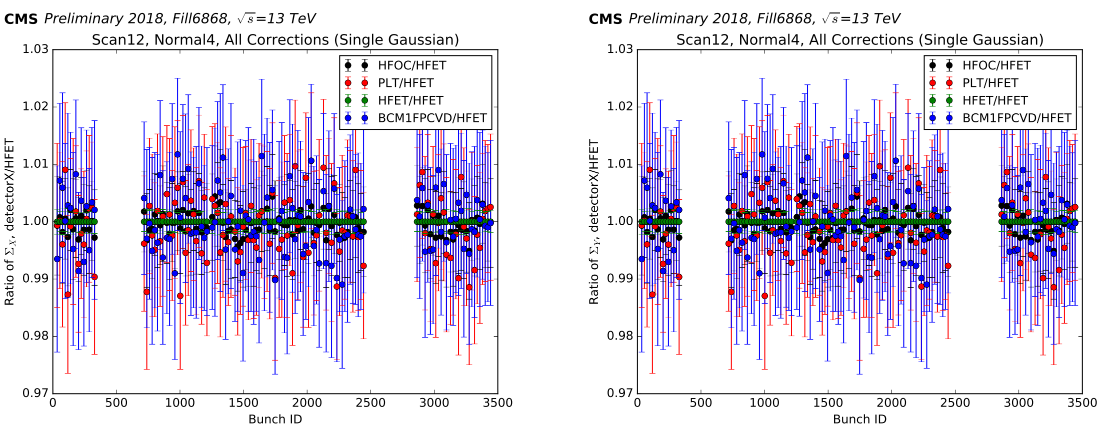

Figure A.14: Ratio of Σ_x (left) and Σ_y (right) for each bunch crossing in a normal vdM scan pair (norm4) for each of the online luminometers (HFET, HFOC, PLT, BCM1F) to $\Sigma_{x,y}$ of HFET.

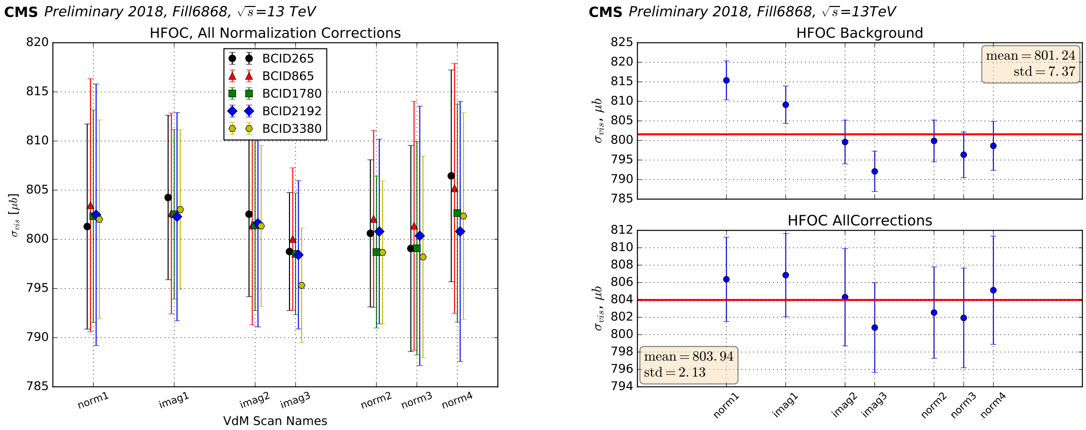

Figure A.15: Left: Measured HFOC visible cross section for all vdM scans, for the five bunch crossings with pixel data available. The uncertainty shown is statistical. Right: The measured visible cross section for each scan, together with the weighted average (red line), with only the background correction applied (top) and with all corrections applied (bottom).

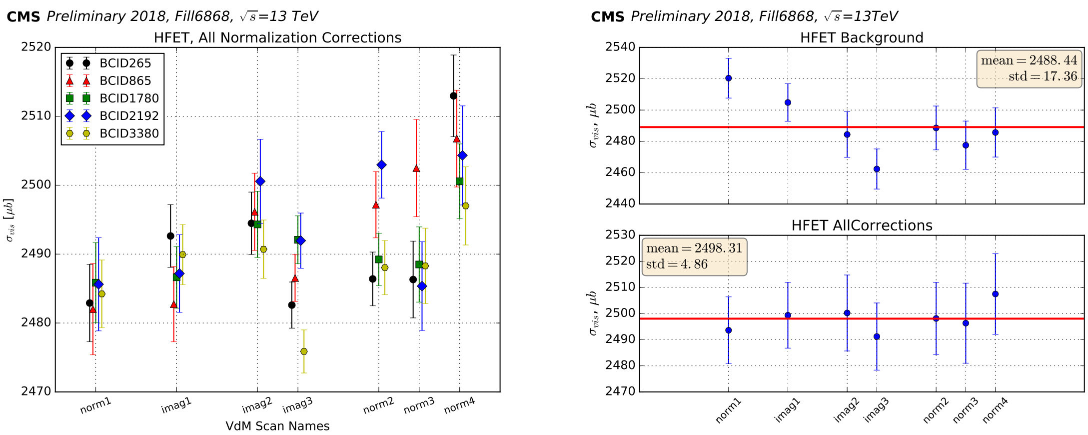

Figure A.16: Left: Measured HFET visible cross section for all vdM scans, for the five bunch crossings with pixel data available. The uncertainty shown is statistical. Right: The measured visible cross section for each scan, together with the weighted average (red line), with only the background correction applied (top) and with all corrections applied (bottom).

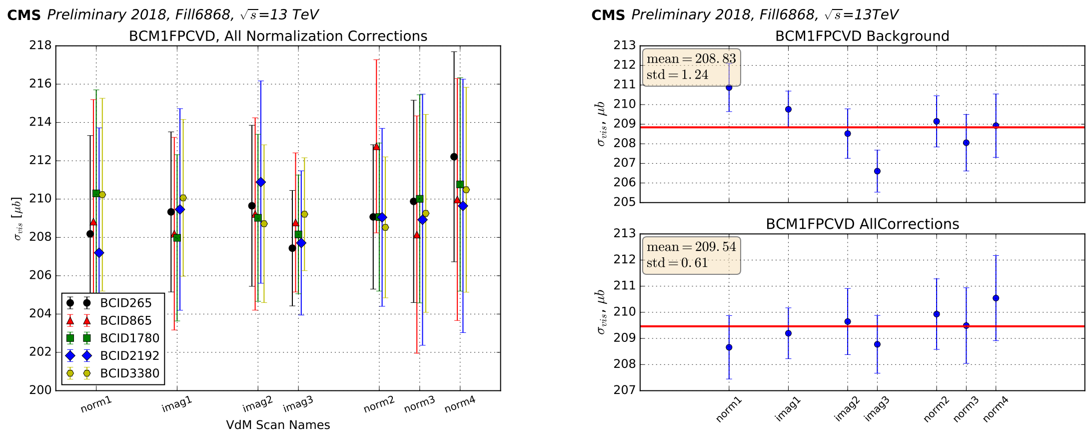

Figure A.17: Left: Measured BCM1F visible cross section for all vdM scans, for the five bunch crossings with pixel data available. The uncertainty shown is statistical. Right: The measured visible cross section for each scan, together with the weighted average (red line), with only the background correction applied (top) and with all corrections applied (bottom).

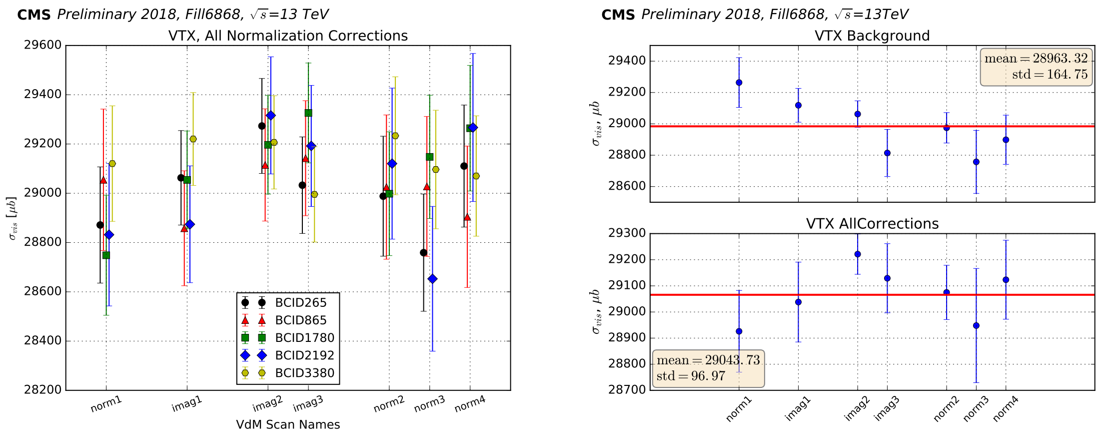

Figure A.18: Left: Measured VTX visible cross section for all vdM scans, for the five bunch crossings with pixel data available. The uncertainty shown is statistical. Right: The measured visible cross section for each scan, together with the weighted average (red line), with only the background correction applied (top) and with all corrections applied (bottom).

APPENDIX B: THE VDM FRAMEWORK EXAMPLES

B.1. Template of the vdmDriver Configuration File

```
{{
"Fill": "{fill}",
"Date": "{date}",
"Luminometer": "{luminometer}",
"AnalysisDir": "{analysisdir}",
"CorrLater" : ["noCorr", "LengthScale", "Ghosts", "Satellites", "BeamBeam", "DynamicBeta","Background"],
"Corr" : {corrs},
"Comment": "Output of following step goes to <AnalysisDir>/cond",
"makeScanFile": {makeScanFile},
"Comment": "Output of following step goes to <AnalysisDir>/LuminometerData",
"makeRateFile": {makeRateFile},
"Comment": "Output of following step goes to <AnalysisDir>/cond",
"makeBeamCurrentFile": {makeBeamCurrentFile},
"Comment": "Output of following step goes to <AnalysisDir>/corr",
"makeBeamBeamFile": {makeBeamBeamFile},
"Comment": "Output of following step goes to <AnalysisDir>/corr",
"makeDynamicBetaFile": {makeDynamicBetaFile},
"Comment": "Output of following step goes to <AnalysisDir>/corr",
"makeGhostsFile": false,
"Comment": "Output of following step goes to <AnalysisDir>/corr",
"makeSatellitesFile": false,
"Comment": "Output of following step goes to <AnalysisDir>/corr",
"makeLengthScaleFile": {makeLengthScaleFile},
"Comment": "Output of following step goes to <AnalysisDir>/corr",
"makeOrbitDriftFile": {makeOrbitDriftFile},
"Comment": "Output of following step goes to <AnalysisDir>/corr",
"makeBackgroundFile": {makeBackgroundFile},
"Comment": "Output of following step goes to <AnalysisDir>/<Luminometer>/graphs",
"makeGraphsFile": {makeGraphsFile},
"Comment": "Output of following step goes to <AnalysisDir>/<Luminometer>/graphs",
"makeGraphs2D": false,
"Comment": "Output of following step goes to <AnalysisDir>/<Luminometer>/results/<Corr>",
"runVdmFitter": {runVdmFitter},
"Comment": "Output of following step goes to <AnalysisDir>/<Luminometer>/results/<Corr>",
"calculateCalibrationConstant": true,
"MakePDF": {makepdf},
"MakeLogs": {makelogs},
"makeScanFileConfig":
    {{
    "InputCentralPath": "{central}",
```

```
    "InputDIPFile" : "{dip}",
        "ScanNames" : {scannames},
        "Comment" : "Since X,Y scans are automatically differentiated, a time window can include
         ↪  an X and a Y scan, will still work, timestamp in UTC",
        "ScanTimeWindows" : {timewindows},
    "Comment" : "A few parameters that are not in our current DIP file, but should be available
     ↪  eventually",
    "Comment" : "betaStar in m, angle in microrad",
    "BetaStar" : {bstar},
    "Angle" : {angle},
    "Offset" : {offsets},
    "ParticleTypeB1" : "proton",
    "ParticleTypeB2" : "proton",
    "Comment": "Beam energies in GeV",
    "EnergyB1" : 6499,
    "EnergyB2" : 6499,
    "OutputSubDir" : "cond",
    "MuScan":{muscan}
    }},
"makeRateFileConfig":
    {{
    "Comment": "The following directories are relative to <AnalysisDir>",
    "InputScanFile": "cond/Scan_{fill}.json",
    "InputLumiDir" : "{central}",
    "RateTable": "{ratetable}",
    "OutputSubDir": "LuminometerData",
    "Comment": "The following items are for PCC and VTX rate files",
    "InputPCCFiles_vdm": ["/scratch/yusufcan_VdM/VdmFramework/merged_ZB1.root"],
    "InputPCCFiles_muscan": ["/scratch/yusufcan_VdM/VdmFramework/merged_7320.root"],
    "PCCTreeName": "pccminitree",
    "PCC_BCID_vdm":[265,865,1780,2192,3380],
    "PCC_BCID_muscan_7358":[750,751,752,753,754,755,756,757,758,759,760,761,1644,1645,1646,1647,
     ↪  1648,1649,1650,1651,1652,1653,1654,1655],
    "PCC_BCID_muscan":[574, 575, 576, 577, 578, 579, 580, 581, 582, 583, 584, 585, 586, 587,
     ↪  588, 589, 590, 591, 592, 593, 594, 595, 596, 597, 598, 599, 600, 601, 602, 603, 604,
     ↪  605, 606, 607, 608, 609, 610, 611, 612, 613, 614, 615, 616, 617, 618, 619, 620, 621],
    "addScanInfo": true
    }},
"makeBeamCurrentFileConfig":
    {{
    "InputCentralPath": "{central}",
    "Comment": "Input scan file in <AnalysisDir>/<InputScanFile>",
    "InputScanFile" : "cond/Scan_{fill}.json",
    "OutputSubDir" : "cond",
    "CalibrateFBCTtoDCCT" : true
    }},
"makeBeamBeamFileConfig":
```

```
    {{
    "Comment": "Input scan info file is <AnalysisDir>/<InputScanFile>",
    "InputScanFile" : "cond/Scan_{fill}.json",
    "Comment": "Input beam currents file is <AnalysisDir>/<InputBeamCurrentFile>",
    "InputBeamCurrentFile" : "cond/BeamCurrents_{fill}.json",
    "Comment": "Input luminometer data in <AnalysisDir>/<InputLuminometerData>",
    "InputLuminometerData" : "LuminometerData/Rates_{luminometer}_{fill}.json",
    "Comment": "Input CapSigmas in <AnalysisDir>/<Luminometer>/results",
    "InputCapSigmaFile" : "{bbsource}/{fit}_FitResults.pkl",
    "Scanpairs" : {scanpairs},
    "Comment": "This is relative to <AnalysisDir>",
    "OutputSubDir": "corr"
    }},
"makeDynamicBetaFileConfig":
    {{
    "Comment": "Input scan info file is <AnalysisDir>/<InputScanFile>",
    "InputScanFile" : "cond/Scan_{fill}.json",
    "Comment": "Input beam currents file is <AnalysisDir>/<InputBeamCurrentFile>",
    "InputBeamCurrentFile" : "cond/BeamCurrents_{fill}.json",
    "Comment": "Input luminometer data in <AnalysisDir>/<InputLuminometerData>",
    "InputLuminometerData" : "LuminometerData/Rates_{luminometer}_{fill}.json",
    "Comment": "Input CapSigmas in <AnalysisDir>/<Luminometer>/results",
    "InputCapSigmaFile" : "{bbsource}/{fit}_FitResults.pkl",
    "Comment": "Input BeamBeam in <AnalysisDir>/corr",
    "InputBeamBeamFile" : "corr/BeamBeam_{luminometer}_{fill}.json",
    "Scanpairs" : {scanpairs},
    "Comment": "This is relative to <AnalysisDir>",
    "OutputSubDir": "corr"
    }},
"makeGhostsFileConfig":
    {{
    "Comment" : "Where to find the correction factors in json format",
    "InputDataDir" : "dataPrep_corr/corrData",
    "Comment": "This is relative to <AnalysisDir>",
    "OutputSubDir": "corr"
    }},
"makeSatellitesFileConfig":
    {{
    "Comment" : "Where to find the correction factors in json format",
    "InputDataDir" : "dataPrep_corr/corrData",
    "Comment": "This is relative to <AnalysisDir>",
    "OutputSubDir": "corr"
    }},
"makeLengthScaleFileConfig":
    {{
    "Comment": "Length scale scan fill",
    "FillLS": "{fill}",
```

```
      "Comment" : "Where to find the correction factors in json format",
      "InputDataDir" : "dataPrep_corr/corrData",
      "Comment": "This is relative to <AnalysisDir>",
      "OutputSubDir": "corr"
      }},
  "makeOrbitDriftFileConfig":
      {{
      "Comment" : "Where to find the correction factors in json format",
      "InputDataDir" : "dataPrep_corr/corrData",
      "Comment" : "Type of the orbit drifts file (DOROS / arcBPM / arcBPM_m_DOROS / arcBPM_DOROS_ave)",
      "OrbitDriftType" : "arcBPM_DOROS_ave",
      "Comment": "This is relative to <AnalysisDir>",
      "OutputSubDir": "corr"
      }},
  "makeGraphsFileConfig":
      {{
      "Comment": "Input scan file in <AnalysisDir>/<InputScanFile>",
      "InputScanFile" : "cond/Scan_{fill}.json",
      "Comment": "Input beam currents file in <AnalysisDir>/<InputBeamCurrentFile>",
      "InputBeamCurrentFile" : "cond/BeamCurrents_{fill}.json",
      "Comment": "Input luminometer data in <AnalysisDir>/<InputLuminometerData>",
      "InputLuminometerData" : "LuminometerData/Rates_{luminometer}_{fill}.json",
      "OutputSubDir" : "graphs",
      "MakePDF": {makepdf}
      }},
  "makeGraphs2DConfig":
      {{
      "Comment": "Defines each X/Y pair for which to make 2D graphs",
      "Scanpairs" : {scanpairs},
      "Comment": "Input/output directory is <AnalysisDir>/<Luminometer>/graphs",
      "InOutSubDir": "graphs"
      }},
  "vdmFitterConfig":
       {{
       "Comment": "Input graphs file in <AnalysisDir>/<Luminometer>/graphs",
       "InputGraphsFile" : "graphs/graphs_{fill}_{corr}.json",
       "FitName" : "{fit}",
       "FitConfigFile" : "fits/{fit}_Config.json",
       "ScanNames" : {scannames},
       "MinuitFile" : "{fit}_{corr}_Minuit"
       }},
  "calculateCalibrationConstantConfig":
      {{
      "Fill" : "{fill}",
      "AnalysisDir" : "{analysisdir}",
      "Luminometer": "{luminometer}",
```

```
    "Corr" : {corrs},
    "Comment": "Input fit results file in <AnalysisDir>/<Luminometer>/results/<Corr>",
    "InputFitResultsFile" : "{fit}_FitResults.pkl",
    "LuminometerSettings":
        {{
        "LuminometerName": "{luminometer}",
        "Comment": "defaults to settings in luminometer.py",
        "Comment": "needs to be set for non-default settings or for new luminometer",
        "LuminometerDescription": "default",
        "WhatIsMeasured": "default",
        "NormalizationGraphs": "default",
        "OldNormAvailable": "false"
        }},
    "Comment": "Total inelastic cross section in microbarn, for pp at 8TeV",
    "Total_inel_Xsec": 72700,
    "Comment": "Use negative number to make clear that no old normalization is available",
    "Comment": "For low energy pp: 10.2; for pp at 8TeV, as determined in April 2012 scan: 6.36",
    "Comment": "For pPb, as determined in Sep 2012 pilot run, taking into account that Pb ion is
      ↪   stripped of all its 82 electrons: 6.36/115.8*82",
    "OldNormalization": 10.2,
    "FormulaToUse": "1D-Gaussian-like",
    "Scanpairs" : {scanpairs}
    }},
"makeBackgroundFileConfig":
    {{
    "RateTable": "{ratetable}",
    "Filename":"{filename1}",
    "Filename2":"{filename2}",
    "FixedBackground":"{fixed}",
    "SuperSeparation":
        {{
        "pltlumizero":[3.3e-06, 9.0e-07],
        "hfoclumi":[3.0e-05, 3.0e-06],
        "bcm1fsilumi":[3.0e-06, 8.0e-07],
        "bcm1fpcvdlumi":[5.0e-06, 1.0e-06],
        "pcclumi":[0.169, 0.003]
        }}
    }}
}}
```

B.2. The Configuration File of the AutoAnalysis

```
{
    "Comment": "Results folder, watch folder, max threads to use, steps needed for double gaussian, ratetables to analyse",
    "automation_folder": "Automation/",
    "central_default": "/brildata/vdmdata18/",
    "log_folder": "Automation/",
    "lxplusconfig": {
        "automation_folder": "Fill6016Final/",
        "central_default": "/eos/cms/store/group/dpg_bril/comm_bril/vdmdata2017/",
        "log_folder": "vdmlogs/"
    },
    "max_threads": 10,
    "dg_steps": 50,
    "ratetables": [
        "vtxlumi"
    ],
    "exampleratetables": [
        "pltlumizero",
        "hfetlumi",
        "hfoclumi",
        "bcm1fsilumi",
        "bcm1fpcvdlumi",
        "bcm1fscvdlumi",
        "bcm1futca_pcvdlumi_100",
        "bcm1futca_pcvdlumi_101",
        "bcm1futca_silumi_100",
        "bcm1futca_silumi_101",
        "pcclumi",
        "vtxlumi"
    ]
}
```

B.3. LumiCalibration Output File for Fill 6868, PLT Detector, Single Gaussian Fit

Scan	Type	BCID	sigma	sigmaErr	Mean	MeanErr	CapSigma	CapSigmaErr	peak	peakErr	chi2	ndof
1	X	13	8.98E-02	2.76E-03	4.06E-03	5.18E-03	1.27E-01	3.90E-03	2.91E-03	1.46E-04	1.15E-01	6
1	X	34	9.50E-02	3.40E-03	2.95E-03	6.38E-03	1.34E-01	4.81E-03	2.63E-03	1.52E-04	4.11E-01	6
1	X	55	9.39E-02	2.72E-03	2.27E-03	5.28E-03	1.33E-01	3.85E-03	2.67E-03	1.28E-04	5.70E-01	6
1	X	76	9.42E-02	3.32E-03	2.54E-03	6.42E-03	1.33E-01	4.70E-03	2.72E-03	1.58E-04	7.06E-01	6
1	X	97	8.95E-02	2.63E-03	3.59E-03	4.96E-03	1.27E-01	3.72E-03	3.05E-03	1.47E-04	1.10E+00	6
1	X	118	9.30E-02	3.25E-03	1.62E-03	6.16E-03	1.32E-01	4.60E-03	2.80E-03	1.60E-04	9.62E-01	6
1	X	139	8.99E-02	2.60E-03	2.59E-03	5.05E-03	1.27E-01	3.68E-03	2.91E-03	1.41E-04	8.06E-01	6
1	X	160	9.38E-02	3.03E-03	1.65E-03	6.43E-03	1.33E-01	4.28E-03	2.70E-03	1.53E-04	5.17E+00	6
1	X	181	9.04E-02	2.45E-03	2.20E-03	4.77E-03	1.28E-01	3.46E-03	3.08E-03	1.40E-04	6.27E-01	6
1	X	202	9.53E-02	3.04E-03	3.49E-03	5.67E-03	1.35E-01	4.31E-03	2.78E-03	1.43E-04	5.40E-01	6
1	X	223	9.23E-02	2.60E-03	3.72E-03	4.90E-03	1.31E-01	3.68E-03	2.94E-03	1.35E-04	5.78E-02	6
1	X	244	9.77E-02	3.30E-03	5.00E-05	6.14E-03	1.38E-01	4.67E-03	2.71E-03	1.46E-04	1.08E+00	6
1	X	265	9.27E-02	2.70E-03	1.15E-03	5.11E-03	1.31E-01	3.83E-03	2.90E-03	1.38E-04	7.46E-01	6
1	X	286	9.47E-02	3.11E-03	5.79E-03	5.77E-03	1.34E-01	4.40E-03	2.81E-03	1.49E-04	4.03E-01	6
1	X	307	9.36E-02	2.73E-03	3.74E-03	5.18E-03	1.32E-01	3.86E-03	2.89E-03	1.38E-04	4.40E-01	6
1	X	328	9.69E-02	3.49E-03	-6.85E-04	6.38E-03	1.37E-01	4.94E-03	2.64E-03	1.51E-04	7.94E-01	6
1	X	718	9.06E-02	2.63E-03	2.37E-03	4.96E-03	1.28E-01	3.72E-03	3.05E-03	1.45E-04	5.22E-01	6
1	X	739	9.42E-02	3.27E-03	2.27E-03	6.18E-03	1.33E-01	4.63E-03	2.81E-03	1.59E-04	7.13E-01	6

Scan	Type	BCID	sigma	sigmaErr	Mean	MeanErr	CapSigma	CapSigmaErr	peak	peakErr	chi2	ndof
1	X	760	9.34E-02	2.75E-03	2.36E-04	5.19E-03	1.32E-01	3.89E-03	2.93E-03	1.41E-04	1.90E+00	6
1	X	781	9.65E-02	3.45E-03	5.91E-03	6.57E-03	1.36E-01	4.87E-03	2.69E-03	1.56E-04	9.44E-01	6
1	X	802	9.28E-02	2.62E-03	-8.51E-04	5.11E-03	1.31E-01	3.71E-03	3.00E-03	1.41E-04	1.04E+00	6
1	X	823	9.52E-02	3.11E-03	1.06E-03	6.11E-03	1.35E-01	4.40E-03	2.85E-03	1.55E-04	9.24E-01	6
1	X	844	9.14E-02	2.62E-03	-2.85E-04	4.96E-03	1.29E-01	3.71E-03	2.96E-03	1.39E-04	9.80E-01	6
1	X	865	9.52E-02	3.26E-03	-4.41E-04	6.32E-03	1.35E-01	4.61E-03	2.60E-03	1.47E-04	1.21E+00	6
1	X	897	9.13E-02	2.65E-03	1.20E-06	5.10E-03	1.29E-01	3.74E-03	3.00E-03	1.44E-04	1.33E+00	6
1	X	918	9.38E-02	3.15E-03	3.00E-03	6.03E-03	1.33E-01	4.45E-03	2.81E-03	1.55E-04	9.81E-01	6
1	X	939	9.05E-02	2.54E-03	2.44E-03	4.92E-03	1.28E-01	3.59E-03	2.94E-03	1.37E-04	1.65E+00	6
1	X	960	9.71E-02	3.32E-03	-3.33E-03	6.22E-03	1.37E-01	4.69E-03	2.73E-03	1.50E-04	9.22E-01	6
1	X	981	9.00E-02	2.54E-03	3.86E-03	4.77E-03	1.27E-01	3.59E-03	3.08E-03	1.42E-04	7.20E-01	6
1	X	1002	9.47E-02	3.11E-03	1.82E-03	6.03E-03	1.34E-01	4.40E-03	2.74E-03	1.49E-04	1.22E+00	6
1	X	1023	9.23E-02	2.46E-03	4.27E-03	4.87E-03	1.31E-01	3.47E-03	2.92E-03	1.31E-04	1.23E+00	6
1	X	1044	9.68E-02	3.23E-03	2.03E-03	6.06E-03	1.37E-01	4.57E-03	2.69E-03	1.45E-04	5.42E-01	6
1	X	1065	9.11E-02	2.48E-03	2.02E-03	4.84E-03	1.29E-01	3.51E-03	2.97E-03	1.35E-04	1.40E+00	6
1	X	1086	9.46E-02	2.95E-03	2.30E-03	5.63E-03	1.34E-01	4.17E-03	2.82E-03	1.44E-04	7.35E-01	6
1	X	1107	9.24E-02	2.75E-03	4.50E-03	5.02E-03	1.31E-01	3.89E-03	2.86E-03	1.36E-04	2.05E+00	6
1	X	1128	9.57E-02	3.10E-03	4.39E-03	6.01E-03	1.35E-01	4.39E-03	2.74E-03	1.47E-04	7.64E-01	6
1	X	1149	9.10E-02	2.61E-03	-4.31E-04	4.87E-03	1.29E-01	3.69E-03	3.02E-03	1.41E-04	5.65E-01	6

Scan	Type	BCID	sigma	sigmaErr	Mean	MeanErr	CapSigma	CapSigmaErr	peak	peakErr	chi2	ndof
1	X	1170	9.44E-02	2.84E-03	3.88E-03	5.58E-03	1.33E-01	4.02E-03	2.81E-03	1.41E-04	9.61E-01	6
1	X	1191	9.24E-02	2.67E-03	2.94E-03	4.92E-03	1.31E-01	3.78E-03	2.91E-03	1.35E-04	1.20E+00	6
1	X	1212	9.58E-02	3.14E-03	1.26E-03	6.04E-03	1.35E-01	4.44E-03	2.66E-03	1.43E-04	9.32E-01	6
1	X	1254	9.04E-02	2.73E-03	1.64E-03	5.22E-03	1.28E-01	3.86E-03	2.95E-03	1.47E-04	6.90E-01	6
1	X	1275	9.34E-02	3.17E-03	3.20E-03	6.09E-03	1.32E-01	4.49E-03	2.78E-03	1.55E-04	6.97E-01	6
1	X	1296	9.10E-02	2.62E-03	4.59E-03	5.08E-03	1.29E-01	3.71E-03	2.86E-03	1.37E-04	9.67E-01	6
1	X	1317	9.30E-02	3.25E-03	1.62E-03	6.41E-03	1.31E-01	4.60E-03	2.72E-03	1.59E-04	1.93E+00	6
1	X	1338	8.73E-02	2.32E-03	6.23E-03	4.63E-03	1.24E-01	3.28E-03	3.13E-03	1.42E-04	9.59E-01	6
1	X	1359	9.82E-02	3.50E-03	2.76E-03	6.52E-03	1.39E-01	4.95E-03	2.58E-03	1.47E-04	5.47E-01	6
1	X	1380	8.94E-02	2.45E-03	5.40E-03	4.78E-03	1.26E-01	3.47E-03	2.97E-03	1.37E-04	5.01E-01	6
1	X	1401	1.06E-01	4.12E-03	-6.97E-04	7.27E-03	1.49E-01	5.83E-03	2.31E-03	1.37E-04	1.81E-01	6
1	X	1433	8.96E-02	2.45E-03	4.07E-03	4.78E-03	1.27E-01	3.46E-03	3.12E-03	1.43E-04	3.62E-01	6
1	X	1454	9.22E-02	2.85E-03	2.84E-03	5.76E-03	1.30E-01	4.04E-03	2.85E-03	1.50E-04	1.26E+00	6
1	X	1475	8.94E-02	2.47E-03	3.94E-03	4.76E-03	1.26E-01	3.50E-03	2.96E-03	1.36E-04	1.24E+00	6
1	X	1496	9.61E-02	3.34E-03	1.38E-03	6.43E-03	1.36E-01	4.73E-03	2.60E-03	1.48E-04	1.25E+00	6
1	X	1517	8.85E-02	2.41E-03	1.97E-03	4.88E-03	1.25E-01	3.41E-03	3.19E-03	1.49E-04	1.59E+00	6
1	X	1538	9.36E-02	3.41E-03	2.26E-03	6.34E-03	1.32E-01	4.82E-03	2.78E-03	1.63E-04	6.78E-02	6
1	X	1559	9.01E-02	2.57E-03	-5.38E-04	5.08E-03	1.27E-01	3.63E-03	2.95E-03	1.42E-04	9.32E-01	6
1	X	1580	9.25E-02	3.27E-03	3.04E-03	6.28E-03	1.31E-01	4.63E-03	2.76E-03	1.61E-04	5.40E-01	6

Scan	Type	BCID	sigma	sigmaErr	Mean	MeanErr	CapSigma	CapSigmaErr	peak	peakErr	chi2	ndof
1	X	1601	9.05E-02	2.67E-03	4.96E-03	5.03E-03	1.28E-01	3.78E-03	3.00E-03	1.45E-04	2.58E-01	6
1	X	1622	9.26E-02	2.90E-03	2.70E-03	5.52E-03	1.31E-01	4.11E-03	2.91E-03	1.50E-04	1.07E+00	6
1	X	1643	9.11E-02	2.52E-03	2.15E-03	4.97E-03	1.29E-01	3.56E-03	2.92E-03	1.36E-04	9.99E-01	6
1	X	1664	9.20E-02	3.03E-03	4.46E-03	5.83E-03	1.30E-01	4.29E-03	2.80E-03	1.52E-04	9.09E-01	6
1	X	1685	8.93E-02	2.53E-03	3.89E-03	4.85E-03	1.26E-01	3.58E-03	3.13E-03	1.47E-04	1.17E+00	6
1	X	1706	9.46E-02	3.04E-03	9.42E-05	5.75E-03	1.34E-01	4.30E-03	2.87E-03	1.50E-04	3.51E-01	6
1	X	1727	9.28E-02	2.75E-03	4.64E-03	5.21E-03	1.31E-01	3.88E-03	2.91E-03	1.40E-04	1.35E+00	6
1	X	1748	9.39E-02	3.47E-03	2.07E-03	6.35E-03	1.33E-01	4.90E-03	2.58E-03	1.52E-04	4.48E-01	6
1	X	1780	9.20E-02	2.72E-03	5.40E-03	5.16E-03	1.30E-01	3.85E-03	3.00E-03	1.45E-04	3.38E-01	6
1	X	1801	9.65E-02	3.43E-03	1.66E-03	6.47E-03	1.36E-01	4.85E-03	2.64E-03	1.52E-04	5.66E-01	6
1	X	1822	9.26E-02	2.67E-03	2.84E-03	5.12E-03	1.31E-01	3.78E-03	2.90E-03	1.38E-04	4.47E-01	6
1	X	1843	9.52E-02	3.63E-03	7.86E-04	6.67E-03	1.35E-01	5.13E-03	2.69E-03	1.63E-04	1.20E+00	6
1	X	1864	8.95E-02	2.46E-03	1.48E-03	4.74E-03	1.27E-01	3.48E-03	3.16E-03	1.44E-04	6.95E-01	6
1	X	1885	9.62E-02	3.23E-03	1.27E-03	6.05E-03	1.36E-01	4.56E-03	2.73E-03	1.48E-04	2.54E+00	6
1	X	1906	9.24E-02	2.51E-03	5.24E-03	4.92E-03	1.31E-01	3.56E-03	2.92E-03	1.33E-04	9.78E-01	6
1	X	1927	9.46E-02	3.14E-03	3.43E-03	5.99E-03	1.34E-01	4.45E-03	2.75E-03	1.49E-04	1.09E+00	6
1	X	1948	9.00E-02	2.49E-03	2.35E-03	4.91E-03	1.27E-01	3.52E-03	3.02E-03	1.41E-04	1.16E+00	6
1	X	1969	9.41E-02	2.95E-03	1.70E-03	5.63E-03	1.33E-01	4.18E-03	2.81E-03	1.44E-04	1.01E+00	6
1	X	1990	9.28E-02	2.61E-03	-1.26E-03	4.98E-03	1.31E-01	3.69E-03	2.90E-03	1.34E-04	7.91E-01	6

Scan	Type	BCID	sigma	sigmaErr	Mean	MeanErr	CapSigma	CapSigmaErr	peak	peakErr	chi2	ndof
1	X	2011	9.58E-02	3.17E-03	1.07E-03	6.04E-03	1.36E-01	4.49E-03	2.72E-03	1.47E-04	7.60E-01	6
1	X	2032	9.14E-02	2.58E-03	-2.26E-04	4.94E-03	1.29E-01	3.65E-03	3.03E-03	1.41E-04	2.59E-01	6
1	X	2053	9.68E-02	3.17E-03	9.04E-04	5.91E-03	1.37E-01	4.48E-03	2.71E-03	1.43E-04	3.47E-01	6
1	X	2074	9.28E-02	2.69E-03	-9.67E-04	5.05E-03	1.31E-01	3.80E-03	2.97E-03	1.40E-04	3.03E-01	6
1	X	2095	9.79E-02	3.50E-03	1.74E-03	6.25E-03	1.39E-01	4.95E-03	2.61E-03	1.45E-04	4.29E-01	6
1	X	2129	8.91E-02	2.60E-03	3.21E-03	4.95E-03	1.26E-01	3.68E-03	3.13E-03	1.51E-04	3.40E-01	6
1	X	2150	9.42E-02	3.29E-03	1.15E-04	6.26E-03	1.33E-01	4.65E-03	2.78E-03	1.58E-04	6.93E-01	6
1	X	2171	9.26E-02	2.63E-03	2.34E-04	5.09E-03	1.31E-01	3.73E-03	2.93E-03	1.39E-04	1.05E+00	6
1	X	2192	9.75E-02	3.41E-03	8.86E-04	6.53E-03	1.38E-01	4.82E-03	2.74E-03	1.56E-04	1.07E+00	6
1	X	2213	8.96E-02	2.41E-03	2.91E-03	4.70E-03	1.27E-01	3.41E-03	3.11E-03	1.41E-04	8.28E-01	6
1	X	2234	9.44E-02	3.23E-03	5.03E-03	5.98E-03	1.34E-01	4.57E-03	2.82E-03	1.55E-04	5.46E-01	6
1	X	2255	9.14E-02	2.66E-03	4.14E-03	4.95E-03	1.29E-01	3.77E-03	2.90E-03	1.37E-04	9.58E-01	6
1	X	2276	9.64E-02	3.20E-03	7.80E-03	6.20E-03	1.36E-01	4.53E-03	2.68E-03	1.47E-04	1.24E+00	6
1	X	2297	9.25E-02	2.72E-03	4.24E-03	5.08E-03	1.31E-01	3.84E-03	3.01E-03	1.44E-04	4.23E-01	6
1	X	2318	9.61E-02	3.23E-03	4.08E-03	6.11E-03	1.36E-01	4.57E-03	2.68E-03	1.46E-04	6.89E-01	6
1	X	2339	9.24E-02	2.67E-03	4.11E-03	5.13E-03	1.31E-01	3.78E-03	2.88E-03	1.37E-04	7.85E-01	6
1	X	2360	9.54E-02	3.16E-03	6.37E-04	6.14E-03	1.35E-01	4.47E-03	2.67E-03	1.46E-04	1.03E+00	6
1	X	2381	9.20E-02	2.75E-03	2.41E-03	5.14E-03	1.30E-01	3.88E-03	2.92E-03	1.42E-04	8.86E-01	6
1	X	2402	9.44E-02	3.15E-03	2.27E-03	5.73E-03	1.34E-01	4.46E-03	2.82E-03	1.49E-04	5.12E-01	6

Scan	Type	BCID	sigma	sigmaErr	Mean	MeanErr	CapSigma	CapSigmaErr	peak	peakErr	chi2	ndof
1	X	2423	9.28E-02	2.59E-03	2.39E-03	4.99E-03	1.31E-01	3.66E-03	2.96E-03	1.37E-04	1.47E+00	6
1	X	2444	9.51E-02	3.13E-03	5.44E-03	5.97E-03	1.34E-01	4.43E-03	2.67E-03	1.44E-04	8.37E-01	6
1	X	2865	8.96E-02	2.56E-03	2.51E-03	4.91E-03	1.27E-01	3.63E-03	3.03E-03	1.44E-04	7.18E-01	6
1	X	2886	9.38E-02	2.89E-03	2.69E-03	5.75E-03	1.33E-01	4.09E-03	2.88E-03	1.50E-04	1.73E+00	6
1	X	2907	9.23E-02	2.69E-03	2.03E-03	4.92E-03	1.31E-01	3.81E-03	2.87E-03	1.34E-04	4.10E-01	6
1	X	2928	9.44E-02	3.18E-03	1.68E-03	6.22E-03	1.33E-01	4.50E-03	2.70E-03	1.51E-04	6.09E-01	6
1	X	2949	9.02E-02	2.52E-03	2.46E-03	4.87E-03	1.28E-01	3.56E-03	3.11E-03	1.45E-04	9.36E-01	6
1	X	2970	9.50E-02	3.10E-03	-1.35E-03	5.95E-03	1.34E-01	4.38E-03	2.80E-03	1.50E-04	1.19E+00	6
1	X	2991	9.17E-02	2.50E-03	1.39E-03	4.88E-03	1.30E-01	3.53E-03	2.97E-03	1.36E-04	6.72E-01	6
1	X	3012	9.62E-02	3.16E-03	4.23E-03	6.23E-03	1.36E-01	4.47E-03	2.70E-03	1.48E-04	1.40E+00	6
1	X	3033	9.02E-02	2.61E-03	2.34E-03	4.93E-03	1.28E-01	3.69E-03	2.98E-03	1.42E-04	8.13E-01	6
1	X	3054	9.29E-02	2.95E-03	2.25E-03	5.57E-03	1.31E-01	4.17E-03	2.82E-03	1.46E-04	7.54E-01	6
1	X	3075	9.28E-02	2.66E-03	4.04E-03	5.11E-03	1.31E-01	3.76E-03	2.88E-03	1.36E-04	1.08E+00	6
1	X	3096	9.83E-02	3.36E-03	-3.45E-04	6.36E-03	1.39E-01	4.75E-03	2.54E-03	1.41E-04	4.28E-01	6
1	X	3128	9.13E-02	2.59E-03	5.88E-04	4.97E-03	1.29E-01	3.66E-03	3.03E-03	1.43E-04	1.15E+00	6
1	X	3149	9.51E-02	3.09E-03	3.48E-03	6.15E-03	1.34E-01	4.38E-03	2.73E-03	1.49E-04	1.91E+00	6
1	X	3170	9.27E-02	2.60E-03	2.73E-03	4.99E-03	1.31E-01	3.68E-03	2.92E-03	1.35E-04	8.44E-01	6
1	X	3191	9.78E-02	3.47E-03	3.05E-03	6.55E-03	1.38E-01	4.91E-03	2.56E-03	1.47E-04	3.17E-01	6
1	X	3212	8.90E-02	2.45E-03	1.98E-03	4.80E-03	1.26E-01	3.46E-03	3.09E-03	1.43E-04	4.62E-01	6

Scan	Type	BCID	sigma	sigmaErr	Mean	MeanErr	CapSigma	CapSigmaErr	peak	peakErr	chi2	ndof
1	X	3233	9.11E-02	3.09E-03	1.93E-03	5.91E-03	1.29E-01	4.37E-03	2.90E-03	1.62E-04	5.68E-01	6
1	X	3254	9.15E-02	2.70E-03	1.16E-03	5.12E-03	1.29E-01	3.82E-03	2.86E-03	1.39E-04	1.15E+00	6
1	X	3275	9.28E-02	3.05E-03	3.87E-03	6.23E-03	1.31E-01	4.31E-03	2.67E-03	1.51E-04	2.19E+00	6
1	X	3296	8.91E-02	2.49E-03	3.53E-03	4.83E-03	1.26E-01	3.52E-03	3.09E-03	1.44E-04	7.68E-01	6
1	X	3317	9.14E-02	2.84E-03	7.77E-03	5.69E-03	1.29E-01	4.01E-03	2.85E-03	1.50E-04	1.10E+00	6
1	X	3338	9.04E-02	2.65E-03	3.85E-03	4.96E-03	1.28E-01	3.75E-03	2.96E-03	1.42E-04	4.80E-01	6
1	X	3359	9.27E-02	2.96E-03	2.37E-03	5.79E-03	1.31E-01	4.19E-03	2.80E-03	1.49E-04	1.16E+00	6
1	X	3380	9.02E-02	2.48E-03	4.31E-04	4.74E-03	1.27E-01	3.51E-03	3.15E-03	1.44E-04	2.96E-01	6
1	X	3401	9.60E-02	3.13E-03	2.50E-03	5.72E-03	1.36E-01	4.42E-03	2.81E-03	1.46E-04	3.31E-01	6
1	X	3422	9.26E-02	2.59E-03	5.72E-04	4.96E-03	1.31E-01	3.67E-03	2.99E-03	1.38E-04	1.61E+00	6
1	X	3443	9.51E-02	3.03E-03	-2.10E-04	5.86E-03	1.34E-01	4.29E-03	2.78E-03	1.46E-04	7.90E-01	6
2	Y	13	8.09E-02	2.60E-03	-4.09E-03	4.48E-03	1.14E-01	3.68E-03	2.85E-03	1.37E-04	2.52E-01	6
2	Y	34	8.23E-02	3.15E-03	-4.07E-03	5.32E-03	1.16E-01	4.46E-03	2.65E-03	1.49E-04	9.18E-01	6
2	Y	55	8.11E-02	2.56E-03	-4.03E-03	4.36E-03	1.15E-01	3.63E-03	2.73E-03	1.28E-04	5.79E-01	6
2	Y	76	8.34E-02	3.27E-03	-2.22E-03	5.55E-03	1.18E-01	4.62E-03	2.62E-03	1.50E-04	7.51E-01	6
2	Y	97	7.75E-02	2.43E-03	-5.09E-04	4.20E-03	1.10E-01	3.44E-03	2.93E-03	1.39E-04	2.62E-01	6
2	Y	118	7.99E-02	3.04E-03	-1.25E-03	5.14E-03	1.13E-01	4.30E-03	2.75E-03	1.55E-04	4.07E-01	6
2	Y	139	7.95E-02	2.49E-03	-4.08E-03	4.28E-03	1.12E-01	3.52E-03	2.87E-03	1.35E-04	5.33E-01	6
2	Y	160	8.14E-02	3.20E-03	-1.93E-03	5.42E-03	1.15E-01	4.52E-03	2.67E-03	1.54E-04	1.32E+00	6

Scan	Type	BCID	sigma	sigmaErr	Mean	MeanErr	CapSigma	CapSigmaErr	peak	peakErr	chi2	ndof
2	Y	181	7.64E-02	2.23E-03	-2.80E-03	3.94E-03	1.08E-01	3.16E-03	3.00E-03	1.36E-04	6.58E-01	6
2	Y	202	7.98E-02	2.67E-03	-2.28E-03	4.65E-03	1.13E-01	3.78E-03	2.75E-03	1.39E-04	7.40E-01	6
2	Y	223	7.84E-02	2.38E-03	3.83E-04	4.07E-03	1.11E-01	3.36E-03	2.87E-03	1.31E-04	2.18E-01	6
2	Y	244	8.08E-02	2.96E-03	-4.82E-03	4.97E-03	1.14E-01	4.19E-03	2.69E-03	1.45E-04	3.13E-01	6
2	Y	265	7.60E-02	2.30E-03	1.37E-03	4.01E-03	1.07E-01	3.25E-03	2.98E-03	1.39E-04	2.55E-01	6
2	Y	286	7.86E-02	2.73E-03	-2.60E-03	4.69E-03	1.11E-01	3.87E-03	2.78E-03	1.46E-04	9.31E-01	6
2	Y	307	7.93E-02	2.42E-03	-1.10E-04	4.27E-03	1.12E-01	3.42E-03	2.86E-03	1.33E-04	6.40E-01	6
2	Y	328	8.20E-02	3.21E-03	-6.83E-04	5.33E-03	1.16E-01	4.54E-03	2.55E-03	1.45E-04	7.26E-01	6
2	Y	718	7.75E-02	2.37E-03	-2.92E-03	4.16E-03	1.10E-01	3.35E-03	2.94E-03	1.38E-04	1.15E+00	6
2	Y	739	8.02E-02	2.98E-03	-1.26E-03	5.19E-03	1.13E-01	4.22E-03	2.71E-03	1.51E-04	9.26E-01	6
2	Y	760	7.88E-02	2.50E-03	-3.70E-03	4.33E-03	1.11E-01	3.53E-03	2.81E-03	1.35E-04	1.92E+00	6
2	Y	781	8.12E-02	3.07E-03	-2.58E-03	5.41E-03	1.15E-01	4.34E-03	2.67E-03	1.52E-04	9.66E-01	6
2	Y	802	7.64E-02	2.27E-03	-1.31E-03	4.06E-03	1.08E-01	3.20E-03	3.05E-03	1.41E-04	1.01E+00	6
2	Y	823	7.86E-02	2.88E-03	9.13E-04	4.93E-03	1.11E-01	4.08E-03	2.82E-03	1.56E-04	1.78E-01	6
2	Y	844	7.85E-02	2.37E-03	-2.30E-03	4.17E-03	1.11E-01	3.34E-03	2.86E-03	1.32E-04	7.45E-01	6
2	Y	865	8.30E-02	3.30E-03	-4.30E-03	5.27E-03	1.17E-01	4.66E-03	2.66E-03	1.49E-04	1.26E+00	6
2	Y	897	7.70E-02	2.39E-03	-1.78E-03	4.18E-03	1.09E-01	3.38E-03	2.97E-03	1.41E-04	3.15E-01	6
2	Y	918	7.70E-02	2.71E-03	-3.20E-03	4.84E-03	1.09E-01	3.83E-03	2.80E-03	1.53E-04	3.02E-01	6
2	Y	939	8.01E-02	2.50E-03	-2.49E-03	4.20E-03	1.13E-01	3.53E-03	2.82E-03	1.31E-04	8.18E-01	6

Scan	Type	BCID	sigma	sigmaErr	Mean	MeanErr	CapSigma	CapSigmaErr	peak	peakErr	chi2	ndof
2	Y	960	8.11E-02	3.05E-03	-4.26E-03	5.13E-03	1.15E-01	4.31E-03	2.70E-03	1.48E-04	6.97E-01	6
2	Y	981	7.53E-02	2.13E-03	-3.21E-03	3.87E-03	1.07E-01	3.02E-03	3.07E-03	1.37E-04	5.34E-01	6
2	Y	1002	7.88E-02	2.87E-03	4.94E-04	4.86E-03	1.12E-01	4.05E-03	2.76E-03	1.50E-04	9.61E-01	6
2	Y	1023	7.85E-02	2.26E-03	-4.58E-03	4.02E-03	1.11E-01	3.19E-03	2.89E-03	1.28E-04	6.64E-01	6
2	Y	1044	8.17E-02	3.05E-03	-2.57E-03	5.04E-03	1.16E-01	4.31E-03	2.65E-03	1.43E-04	1.24E+00	6
2	Y	1065	7.55E-02	2.12E-03	-1.75E-03	3.83E-03	1.07E-01	2.99E-03	3.05E-03	1.35E-04	9.31E-01	6
2	Y	1086	7.95E-02	2.77E-03	-3.27E-03	4.78E-03	1.12E-01	3.91E-03	2.70E-03	1.40E-04	2.05E+00	6
2	Y	1107	7.89E-02	2.47E-03	-1.25E-03	4.15E-03	1.12E-01	3.49E-03	2.84E-03	1.32E-04	7.58E-01	6
2	Y	1128	8.20E-02	3.05E-03	-1.53E-03	5.14E-03	1.16E-01	4.31E-03	2.59E-03	1.41E-04	6.39E-01	6
2	Y	1149	7.57E-02	2.22E-03	-3.55E-03	3.94E-03	1.07E-01	3.15E-03	3.01E-03	1.38E-04	2.27E-01	6
2	Y	1170	7.94E-02	2.65E-03	-3.25E-03	4.56E-03	1.12E-01	3.75E-03	2.81E-03	1.41E-04	3.93E-01	6
2	Y	1191	8.00E-02	2.32E-03	-2.26E-03	4.13E-03	1.13E-01	3.28E-03	2.85E-03	1.27E-04	1.76E+00	6
2	Y	1212	8.19E-02	2.95E-03	-6.21E-04	5.05E-03	1.16E-01	4.17E-03	2.59E-03	1.38E-04	6.21E-01	6
2	Y	1254	7.77E-02	2.45E-03	-2.69E-03	4.31E-03	1.10E-01	3.46E-03	2.97E-03	1.43E-04	4.21E-01	6
2	Y	1275	7.94E-02	2.94E-03	-3.26E-03	5.04E-03	1.12E-01	4.16E-03	2.76E-03	1.53E-04	8.02E-01	6
2	Y	1296	7.93E-02	2.44E-03	-1.91E-03	4.21E-03	1.12E-01	3.45E-03	2.90E-03	1.35E-04	3.02E-01	6
2	Y	1317	8.14E-02	3.16E-03	-2.44E-03	5.37E-03	1.15E-01	4.47E-03	2.72E-03	1.56E-04	6.47E-01	6
2	Y	1338	7.58E-02	2.16E-03	-5.27E-03	3.88E-03	1.07E-01	3.05E-03	3.06E-03	1.37E-04	6.36E-01	6
2	Y	1359	7.94E-02	3.00E-03	-3.65E-03	5.11E-03	1.12E-01	4.24E-03	2.66E-03	1.50E-04	1.46E+00	6

Scan	Type	BCID	sigma	sigmaErr	Mean	MeanErr	CapSigma	CapSigmaErr	peak	peakErr	chi2	ndof
2	Y	1380	7.88E-02	2.32E-03	-4.70E-03	4.06E-03	1.11E-01	3.28E-03	2.90E-03	1.30E-04	6.51E-01	6
2	Y	1401	8.34E-02	3.36E-03	-3.46E-03	5.68E-03	1.18E-01	4.75E-03	2.33E-03	1.37E-04	9.57E-01	6
2	Y	1433	7.66E-02	2.29E-03	-4.45E-03	3.99E-03	1.08E-01	3.24E-03	3.04E-03	1.39E-04	2.84E-01	6
2	Y	1454	8.03E-02	2.90E-03	-1.67E-03	4.84E-03	1.14E-01	4.11E-03	2.81E-03	1.49E-04	1.31E+00	6
2	Y	1475	8.09E-02	2.37E-03	-4.36E-03	4.14E-03	1.14E-01	3.36E-03	2.89E-03	1.28E-04	1.01E+00	6
2	Y	1496	8.24E-02	3.16E-03	-4.63E-03	5.21E-03	1.16E-01	4.47E-03	2.71E-03	1.51E-04	8.44E-01	6
2	Y	1517	7.64E-02	2.29E-03	-3.16E-03	4.12E-03	1.08E-01	3.24E-03	3.05E-03	1.43E-04	5.72E-01	6
2	Y	1538	7.89E-02	3.00E-03	1.38E-04	5.12E-03	1.12E-01	4.25E-03	2.83E-03	1.61E-04	4.79E-01	6
2	Y	1559	7.92E-02	2.52E-03	-4.06E-03	4.30E-03	1.12E-01	3.56E-03	2.94E-03	1.39E-04	1.18E+00	6
2	Y	1580	8.25E-02	3.25E-03	-3.70E-03	5.47E-03	1.17E-01	4.59E-03	2.66E-03	1.53E-04	4.25E-01	6
2	Y	1601	7.54E-02	2.30E-03	-3.69E-03	4.00E-03	1.07E-01	3.25E-03	3.09E-03	1.45E-04	2.74E-01	6
2	Y	1622	7.80E-02	2.56E-03	6.76E-04	4.52E-03	1.10E-01	3.62E-03	2.87E-03	1.45E-04	4.48E-01	6
2	Y	1643	7.76E-02	2.26E-03	-2.48E-03	4.01E-03	1.10E-01	3.20E-03	3.00E-03	1.36E-04	8.06E-01	6
2	Y	1664	8.07E-02	3.01E-03	-3.78E-04	4.94E-03	1.14E-01	4.26E-03	2.72E-03	1.48E-04	9.37E-01	6
2	Y	1685	7.56E-02	2.20E-03	-1.61E-03	4.01E-03	1.07E-01	3.11E-03	3.04E-03	1.40E-04	1.43E+00	6
2	Y	1706	7.82E-02	2.68E-03	-3.02E-03	4.67E-03	1.11E-01	3.79E-03	2.81E-03	1.47E-04	4.26E-01	6
2	Y	1727	7.73E-02	2.36E-03	-2.80E-03	4.17E-03	1.09E-01	3.34E-03	2.90E-03	1.37E-04	4.80E-01	6
2	Y	1748	8.38E-02	3.15E-03	2.14E-04	5.43E-03	1.19E-01	4.46E-03	2.59E-03	1.43E-04	1.11E+00	6
2	Y	1780	7.56E-02	2.31E-03	-7.00E-04	4.12E-03	1.07E-01	3.27E-03	3.01E-03	1.44E-04	3.53E-01	6

Scan	Type	BCID	sigma	sigmaErr	Mean	MeanErr	CapSigma	CapSigmaErr	peak	peakErr	chi2	ndof
2	Y	1801	7.92E-02	2.99E-03	-3.85E-03	5.11E-03	1.12E-01	4.23E-03	2.72E-03	1.54E-04	3.68E-01	6
2	Y	1822	7.89E-02	2.44E-03	-2.56E-03	4.24E-03	1.12E-01	3.45E-03	2.87E-03	1.34E-04	3.67E-01	6
2	Y	1843	8.21E-02	3.39E-03	-2.09E-03	5.69E-03	1.16E-01	4.79E-03	2.58E-03	1.55E-04	1.03E+00	6
2	Y	1864	7.58E-02	2.23E-03	-2.78E-03	3.95E-03	1.07E-01	3.16E-03	3.04E-03	1.39E-04	7.70E-01	6
2	Y	1885	8.08E-02	3.01E-03	-4.55E-03	4.98E-03	1.14E-01	4.25E-03	2.70E-03	1.47E-04	7.97E-01	6
2	Y	1906	7.76E-02	2.31E-03	-1.14E-03	4.02E-03	1.10E-01	3.26E-03	2.89E-03	1.32E-04	1.17E-01	6
2	Y	1927	7.94E-02	2.91E-03	-3.19E-03	4.91E-03	1.12E-01	4.12E-03	2.71E-03	1.48E-04	1.66E-01	6
2	Y	1948	7.60E-02	2.27E-03	-2.82E-03	4.01E-03	1.07E-01	3.20E-03	3.03E-03	1.40E-04	8.85E-01	6
2	Y	1969	7.87E-02	2.70E-03	-1.91E-03	4.62E-03	1.11E-01	3.82E-03	2.78E-03	1.43E-04	5.09E-01	6
2	Y	1990	7.75E-02	2.23E-03	-4.13E-03	3.99E-03	1.10E-01	3.16E-03	2.96E-03	1.33E-04	6.02E-01	6
2	Y	2011	8.03E-02	2.99E-03	1.00E-03	5.00E-03	1.14E-01	4.22E-03	2.64E-03	1.44E-04	2.59E-01	6
2	Y	2032	7.61E-02	2.23E-03	-3.07E-03	4.02E-03	1.08E-01	3.15E-03	3.00E-03	1.38E-04	6.74E-01	6
2	Y	2053	7.88E-02	2.75E-03	-3.13E-03	4.70E-03	1.11E-01	3.89E-03	2.75E-03	1.44E-04	2.22E-01	6
2	Y	2074	7.76E-02	2.42E-03	3.48E-04	4.23E-03	1.10E-01	3.42E-03	2.83E-03	1.34E-04	1.74E+00	6
2	Y	2095	8.05E-02	2.97E-03	-1.36E-03	5.00E-03	1.14E-01	4.21E-03	2.64E-03	1.44E-04	1.79E+00	6
2	Y	2129	7.45E-02	2.31E-03	2.98E-04	4.07E-03	1.05E-01	3.26E-03	3.02E-03	1.45E-04	3.24E-01	6
2	Y	2150	7.94E-02	3.03E-03	-5.22E-03	5.13E-03	1.12E-01	4.29E-03	2.75E-03	1.57E-04	4.55E-01	6
2	Y	2171	7.97E-02	2.51E-03	-7.96E-04	4.32E-03	1.13E-01	3.55E-03	2.80E-03	1.33E-04	4.77E-01	6
2	Y	2192	7.93E-02	3.08E-03	-4.72E-03	5.29E-03	1.12E-01	4.36E-03	2.68E-03	1.56E-04	7.81E-01	6

Scan	Type	BCID	sigma	sigmaErr	Mean	MeanErr	CapSigma	CapSigmaErr	peak	peakErr	chi2	ndof
2	Y	2213	7.56E-02	2.16E-03	-2.59E-04	3.84E-03	1.07E-01	3.06E-03	3.09E-03	1.38E-04	1.02E+00	6
2	Y	2234	7.83E-02	2.81E-03	-4.25E-03	4.86E-03	1.11E-01	3.97E-03	2.80E-03	1.52E-04	8.94E-01	6
2	Y	2255	7.82E-02	2.36E-03	-3.23E-03	4.09E-03	1.11E-01	3.33E-03	2.88E-03	1.32E-04	2.15E-01	6
2	Y	2276	8.11E-02	3.04E-03	-6.57E-03	5.17E-03	1.15E-01	4.30E-03	2.61E-03	1.44E-04	8.07E-01	6
2	Y	2297	7.68E-02	2.33E-03	-3.20E-03	4.11E-03	1.09E-01	3.29E-03	2.98E-03	1.40E-04	7.44E-01	6
2	Y	2318	7.92E-02	2.77E-03	-3.81E-03	4.80E-03	1.12E-01	3.91E-03	2.80E-03	1.48E-04	4.84E-01	6
2	Y	2339	7.74E-02	2.36E-03	-2.71E-03	4.12E-03	1.09E-01	3.34E-03	2.93E-03	1.37E-04	7.87E-01	6
2	Y	2360	7.94E-02	2.89E-03	-2.67E-03	4.94E-03	1.12E-01	4.08E-03	2.74E-03	1.48E-04	7.51E-01	6
2	Y	2381	7.54E-02	2.31E-03	-2.85E-03	4.04E-03	1.07E-01	3.26E-03	3.02E-03	1.43E-04	8.44E-01	6
2	Y	2402	7.93E-02	2.69E-03	-5.78E-03	4.74E-03	1.12E-01	3.81E-03	2.73E-03	1.42E-04	4.80E-01	6
2	Y	2423	7.87E-02	2.31E-03	-2.48E-03	4.17E-03	1.11E-01	3.26E-03	2.85E-03	1.30E-04	1.27E+00	6
2	Y	2444	7.98E-02	2.78E-03	-4.66E-03	4.81E-03	1.13E-01	3.93E-03	2.74E-03	1.44E-04	3.05E-01	6
2	Y	2865	7.71E-02	2.35E-03	-3.41E-04	4.10E-03	1.09E-01	3.33E-03	2.94E-03	1.38E-04	2.61E-01	6
2	Y	2886	7.88E-02	2.87E-03	-1.27E-03	4.85E-03	1.11E-01	4.06E-03	2.72E-03	1.47E-04	9.59E-01	6
2	Y	2907	7.81E-02	2.31E-03	2.93E-05	3.99E-03	1.10E-01	3.26E-03	2.92E-03	1.31E-04	1.87E-01	6
2	Y	2928	8.21E-02	3.20E-03	-1.74E-03	5.28E-03	1.16E-01	4.52E-03	2.65E-03	1.49E-04	4.01E-01	6
2	Y	2949	7.52E-02	2.25E-03	-2.39E-03	3.93E-03	1.06E-01	3.19E-03	3.14E-03	1.45E-04	9.34E-01	6
2	Y	2970	7.77E-02	2.74E-03	-1.65E-03	4.71E-03	1.10E-01	3.88E-03	2.87E-03	1.53E-04	5.30E-01	6
2	Y	2991	7.82E-02	2.33E-03	-8.77E-04	4.04E-03	1.11E-01	3.29E-03	2.92E-03	1.33E-04	3.07E-01	6

Scan	Type	BCID	sigma	sigmaErr	Mean	MeanErr	CapSigma	CapSigmaErr	peak	peakErr	chi2	ndof
2	Y	3012	8.11E-02	3.04E-03	-3.86E-03	5.12E-03	1.15E-01	4.30E-03	2.68E-03	1.48E-04	7.36E-01	6
2	Y	3033	7.67E-02	2.29E-03	-1.90E-03	4.04E-03	1.08E-01	3.24E-03	2.97E-03	1.37E-04	9.13E-01	6
2	Y	3054	8.06E-02	2.78E-03	-3.60E-03	4.72E-03	1.14E-01	3.93E-03	2.75E-03	1.41E-04	1.84E-01	6
2	Y	3075	7.69E-02	2.39E-03	-9.88E-04	4.12E-03	1.09E-01	3.38E-03	2.88E-03	1.36E-04	2.52E-01	6
2	Y	3096	8.25E-02	3.05E-03	-2.28E-03	5.10E-03	1.17E-01	4.31E-03	2.66E-03	1.43E-04	5.71E-01	6
2	Y	3128	7.67E-02	2.36E-03	-1.57E-03	4.12E-03	1.09E-01	3.34E-03	2.91E-03	1.38E-04	6.16E-01	6
2	Y	3149	7.92E-02	2.82E-03	-1.46E-03	4.90E-03	1.12E-01	3.99E-03	2.81E-03	1.51E-04	5.49E-01	6
2	Y	3170	7.99E-02	2.40E-03	-2.90E-03	4.20E-03	1.13E-01	3.39E-03	2.84E-03	1.29E-04	1.01E+00	6
2	Y	3191	8.45E-02	3.30E-03	-3.99E-03	5.48E-03	1.20E-01	4.67E-03	2.58E-03	1.44E-04	5.49E-01	6
2	Y	3212	7.49E-02	2.17E-03	6.16E-04	3.88E-03	1.06E-01	3.08E-03	3.12E-03	1.42E-04	9.54E-01	6
2	Y	3233	8.13E-02	2.96E-03	-2.79E-03	5.17E-03	1.15E-01	4.18E-03	2.76E-03	1.50E-04	8.64E-01	6
2	Y	3254	7.82E-02	2.43E-03	-3.61E-03	4.17E-03	1.11E-01	3.44E-03	2.91E-03	1.37E-04	1.33E+00	6
2	Y	3275	7.97E-02	2.97E-03	-2.47E-03	4.98E-03	1.13E-01	4.20E-03	2.86E-03	1.57E-04	4.44E-01	6
2	Y	3296	7.46E-02	2.21E-03	-2.61E-03	3.92E-03	1.06E-01	3.13E-03	3.07E-03	1.42E-04	6.72E-01	6
2	Y	3317	7.89E-02	2.65E-03	-1.67E-04	4.69E-03	1.12E-01	3.75E-03	2.88E-03	1.48E-04	1.06E+00	6
2	Y	3338	7.76E-02	2.28E-03	-4.30E-03	4.07E-03	1.10E-01	3.22E-03	2.99E-03	1.36E-04	3.55E-01	6
2	Y	3359	8.04E-02	2.86E-03	-4.03E-03	4.85E-03	1.14E-01	4.05E-03	2.78E-03	1.46E-04	5.88E-01	6
2	Y	3380	7.28E-02	2.01E-03	-2.04E-03	3.77E-03	1.03E-01	2.84E-03	3.14E-03	1.41E-04	1.11E+00	6
2	Y	3401	7.69E-02	2.52E-03	-2.35E-03	4.50E-03	1.09E-01	3.56E-03	2.85E-03	1.45E-04	6.24E-01	6

Scan	Type	BCID	sigma	sigmaErr	Mean	MeanErr	CapSigma	CapSigmaErr	peak	peakErr	chi2	ndof
2	Y	3422	7.79E-02	2.27E-03	-1.03E-03	4.10E-03	1.10E-01	3.20E-03	2.90E-03	1.32E-04	1.06E+00	6
2	Y	3443	8.15E-02	2.94E-03	-2.43E-03	5.02E-03	1.15E-01	4.16E-03	2.61E-03	1.40E-04	1.99E-01	6